Carbon-based transparent microelectrodes for optical investigation and electrophysiology

Dissertation
der Mathamatisch-Naturwissenschaftlichen Fakultät
der Eberhard Karls Universität Tübingen
zur Erlangun des Grades eines
Doktors der Naturwissenschaften
(Dr. rer. nat.)

vorgelegt von
Pranoti Kshirsagar
aus Nagpur, India

Tübingen
2019

Summary

The goal of this work was to develop carbon based transparent electrodes for advancement of microelectrode array (MEA) technology by allowing the possibility of combining optical methods with classical electrophysiology. Recent years have seen a surge of interest in novel methods such as optogenetics and calcium imaging with the focus on understanding the complex neuronal networks. The conventional microelectrode materials obstruct the optical access, which is from the substrate side with an inverted microscope, and this limitation is overcome by using carbon materials. This work was focused on three main materials - carbon nanostructures, graphene and graphene/PEDOT:PSS (poly(3,4-ethylenedioxythiophene)). The transparency often comes at the cost of high electrochemical impedance. This challenge was tackled by using a novel combination of chemical vapour deposited (CVD) graphene and PEDOT:PSS.

Carbon nanostructures were grown at 550 °C by CVD with acetylene as the carbon source. The morphology was studied by scanning electron microscope (SEM) and the presence of nanostructures mixed with amorphous carbon confirmed by Raman spectroscopy. The semitransparent nature was revealed by UV-Vis measurements. The electrochemical impedance was in the acceptable range for electrophysiological recordings. The functionality of the carbon nanostructure microelectrodes was confirmed by recording electrogenic signals from cardiomyocytes where the optical inspection of the cells through the semitransparent microelectrodes was possible. The mechanical robustness and biocompatibility was revealed by studying the electrode-cell ultrastructure.

Graphene was grown by CVD with methane as the carbon source and integrated in the MEA fabrication process. The largely single layer graphene was investigated with SEM and Raman spectroscopy. The excellent transparency over the entire microelectrode was revealed by optical transmittance measurements. The graphene microelectrodes displayed high electrochemical impedance which led to high noise during electrophysiology. The functionality of the transparent graphene mircoelectrodes was checked with cardiomyocytes where high amplitude signals were detected similar to recording with standard electrodes, however, the smaller amplitude signals went unrecorded owing to the high noise.

Graphene/PEDOT:PSS microelectrodes were fabricated by electrodeposition of the conducting polymer PEDOT:PSS on graphene microelectrodes. Optical microscopy revealed that PEDOT:PSS followed the graphene surface and the continuous coverage of the latter by the former reduced to sparse coverage with decreasing amount of PEDOT:PSS. Raman spectroscopy, especially in the case of lower PEDOT:PSS amounts, revealed the presence of PEDOT:PSS on regions which appeared transparent optically. This information was crucial in understanding the electrodeposition mechanism. The electrochemical impedance was found to be comparable with the commercially available TiN microelectrodes and the applicability was tested with cardiomyocytes. Optical imaging was possible through the transparent microelectrodes. An optimum balance between the optical transparency and electrochemical impedance was obtained which allows flexibility in producing microelectrodes for a wide range of applications.

This work presents a comprehensive view on carbon based transparent microelectrodes for novel applications employing combinations of electro- and opto-physiology. The electrodes fabricated in this work are expected to go a long way in assistance with decoding the complex biological systems and provide insights on the single cell level.

Zusammenfassung

Das Ziel der vorliegenden Arbeit lag in der Entwicklung kohlenstoffbasierter, transparenter Elektroden zur Weiterentwicklung der Mikroelektrodenmatrix-Technologie (MEA) durch Ermöglichung der Kombination optischer und klassischer elektrophysiologischer Methoden. In den letzten Jahren konnte ein vermehrtes Interesse an neuen Methoden wie Calcium-Imaging und Optogenetik beobachtet werden, deren Fokus auf dem verbesserten Verständnis komplexer neuronaler Netzwerke liegt. Konventionelle Elektrodenmaterialien verhindern den optischen Zugang mit inversen Mikroskopen von der Substratseite aus, eine Einschränkung welche mit Hilfe von kohlenstoffbasierten Materialien überwunden werden kann. Diese Arbeit konzentriert sich auf drei solcher Materialien – Kohlenstoffnanostrukturen, Graphen und Graphen/PEDOT:PSS (Poly-(3,4-ethylendioxithiophen)). Die Transparenz der Elektrodenmaterialien geht oft auf Kosten der elektrochemischen Impedanz. Diese Herausforderung wurde durch eine neuartige Kombination aus durch chemische Gasphasenabscheidung gewonnenem Graphen und PEDOT:PSS angegangen.

Die Kohlenstoffnanostrukturen wurden durch chemische Gasphasenabscheidung (CVD) bei 550 °C unter Nutzung von Ethin als Kohlenstoffquelle hergestellt. Die Morphologie dieser Strukturen wurde rasterelektronenmikroskopisch untersucht und das Vorliegen von Nanostrukturen neben amorphem Kohlenstoff konnte durch Raman-Spektroskopie bestätigt werden. Die semitransparenten Eigenschaften dieser Nanostrukturen wurden durch UV/Vis-spektroskopische Messungen offenbart. Die elektrochemische Impedanz konnte innerhalb des für elektrophysiologische Messungen angemessenen Bereichs verortet werden. Die Funktionalität der Kohlenstoffnanostruktur-Mikroelektroden wurde durch die Aufnahme elektrogener Signale von Kardiomyozyten bei gleichzeitiger optischer Überwachung der Zellen durch die semitransparenten Elektroden bestätigt. Die mechanische Robustheit sowie die Biokompabilität wurde durch Untersuchung der Zell-Elektroden-Ultrastruktur aufgezeigt.

Graphen wurde durch chemische Gasphasenabscheidung hergestellt, wobei Methan als Kohlenstoffquelle diente, und in den MEA-Produktionsprozess eingebunden. Das weitgehend einlagige Graphen wurde mit Hilfe von Rastertunnelmikroskopie und Raman-Spektroskopie analysiert. Die hervorragende Transparenz über die gesamte Mikroelektrodenfläche konnte durch optische Transmissionsmessungen nachgewiesen werden. Die Graphen-Mikroelektroden zeigten eine hohe elektrochemische Impedanz, was ein starkes Rauschen während elektrophysiologischer Messungen zur Folge hatte. Die Funktionalität der transparenten Graphen-Mikroelektroden wurde durch die Aufnahme elektrogener Signale von Kardiomyozyten überprüft, wobei Signale hoher Amplitude wie mit Standardelektroden detektiert werden konnten, während Signale kleinerer Amplitude aufgrund des starken Rauschens verloren gingen.

Die Graphen/PEDOT:PSS-Mikroelektroden wurden durch elektrolytische Abscheidung des elektrisch leitenden Polymers PEDOT:PSS auf Graphen-Mikroelektroden hergestellt. Die Untersuchung der Abscheidungen durch optische Mikroskopie zeigte, dass das PEDOT:PSS-Polymer auf der Graphenoberfläche abgeschieden wurde, wobei die Überdeckung mit dem Polymer bei kürzerer Abscheidungszeit geringer war. Bereiche geringer Schichtdicke des Polymers wiesen optische Transparenz auf. Raman-spektroskopische Analyse konnte auch in diesen Bereichen das Vorhandensein von PEDOT:PSS nachweisen. Diese Beobachtung war entscheidend für das Verständnis des Abscheidungsmechanismus. Die ermittelte elektrochemische Impedanz der Graphen/PEDOT:PSS-Mikroelektroden ist vergleichbar mit der kommerziell erhältlicher TiN-Mikroelektroden und ihre Funktionalität wurde durch die Aufnahme elektrogener Signale von Kardiomyozyten bestätigt. Die simultane optische Zugänglichkeit durch die transparenten Elektroden konnte ebenfalls bestätigt werden. Es wurde somit die bestmögliche Balance zwischen optischer Transparenz und elektrochemischer Impedanz erreicht, wodurch die Produktion von Mikroelektroden für eine breit gefächerte Palette von Anwendungen ermöglicht wird.

Diese Arbeit stellt einen umfassenden Einblick in den Bereich kohlenstoffbasierter Mikroelektroden

für neuartige Anwendungen unter Einbezug von sowohl Elektro- als auch Optophysiologie dar. Die hergestellten Elektroden sollen helfen, komplexe biologische Systeme besser zu verstehen sowie Einblicke auch auf der Ebene einzelner Zellen zu gewähren.

Acknowledgements

Contents

1 Introduction

1.1 Motivation

Biological tissues and cells contain ion-channels which allow the passage of ions resulting in a potential difference across the cells membrane. This potential difference is picked up by electrodes and the recorded signals are decoded to understand the inter- and intra-cellular communication. The field of recording the electrogenic activity of the cells, electrophysiology, finds application in various fields ranging from neuroscience to drug development. In neuroscience, the recordings provide deep insights in the complex neuronal networks in brain and retina. The effect of a new drug under investigation can be quantified by monitoring the change in the cellular signals.

Microelectrode arrays (MEAs) are widely used for electrophysiological measurements with simultaneous optical investigation being a novel and young field. For effective electrogenic cellular recordings, the electrodes must display low electrochemical impedance values which ensures low thermal noise and hence, improved signal-to-noise ratio. Comprehensive understanding of the biological system is possible when the recording site (electrode) dimension is in the range of the cell dimension. The impedance, and in turn the thermal noise, increases with decreasing electrode size. A typically used electrode diameter is 30 µm.

Optogenetics and calcium imaging are emerging new fields which require optical access while recording electrogenic cellular activity. In optogenetics certain channels in the cells are optically activated and in calcium imaging the calcium channels are activated by chemical modification. Electrophysiology coupled with optical investigation offers comprehensive understanding of the biological systems. Optical access is made possible by using float-glass as a base substrate instead of a printed circuit board. However, conduction paths and microelectrodes are made of opaque materials, such as, titanium nitride (TiN) [1], platinum (Pt) [2], gold (Au) [3], iridium oxide IrO_x [4, 5] and more recently Au coated with poly(3,4-ethylenedioxythiophene):polystyrene sulfonate-carbon nanotubes (PEDOT:PSS-CNT) [6]. The maximum recorded signal is contributed by the cells either directly on top or in the vicinity of the microelectrode. The opaque materials obstruct the view which can be tackled by 3-dimensional (3D) imaging where optical images of different planes away from the substrate are stacked, resulting in the 3D image. However, the opaque electrode casts a shadow in the vicinity of the electrode. In addition, conventional materials show light induced artifacts upon light interaction resulting in altered signal (voltage) which can be misinterpreted as an electrophysiological signal. This is a major drawback in using conventional, metal-based electrodes in optogenetics and calcium imaging.

In this work, carbon based materials were chosen as they display excellent electrical properties and possible optical transparency without light induced artefacts. Carbon nanotubes have been explored but their optical properties are yet to be investigated in the MEA technology. Graphene has attracted a lot of attention since the first isolated preparation over a decade ago. The entry of graphene in the MEA technology is relatively recent and more work needs to be done in utilizing the optical transparency which comes at the price of increased impedance. The conducting polymer PEDOT:PSS has been used to reduce the impedance of microelectrodes. Combining graphene with PEDOT:PSS could balance out the poor impedance properties while taking advantage of their optical transparency.

1.2 Aim and Outline

The aim of this work was to prepare and anaylze three types of carbon based electrodes - carbon nanostructures, graphene and graphene/PEDOT:PSS. The carbon materials were produced, characterized - optically and electrochemically, and their applicability evaluated by recording cellular activity. The goal was to develop microelectrodes for a wide variety of applications from conventional electrophysiolgy,

where low impedance is desirable, to novel applications, such as optogenetics and calcium imaging where optical transparency is preferred.

Chapter 2 (Fundamentals) begins with the background and state of the art of MEAs, discusses the benefits of transparent electrodes, the basics behind the carbon based materials and an overview of the carbon materials in MEA technology. Chapter 3 (Materials) details the production, equipment details and integration of the carbon materials in MEAs. Chapter 4 (Methods) includes a brief description of the microscopic, electrochemical and optical characterization methods as well as the equipment and parameters used. Chapters 5, 6 and 7 include the discussed results of the carbon nanostructures, graphene and graphene/PEDOT:PSS microelectrodes, respectively. Chapter 8 concludes the discussion and offers an outlook.

2 Fundamentals

2.1 Microelectrode Arrays

Microelectrode arrays (MEAs) are used for sensing extracellular electrical activity of electrogenic cells such as neurons and cardiomyocytes. The extracellular field is caused by the current flowing from the ionic processes across the morphology of the cell. The ion channels in cells control the exchange of ions and, in turn, the current which is recorded when cells come in the vicinity of microelectrodes. Neurons, the basic unit of the nervous system, consist of axons and dendrites. Axons carry information to and from the cell body. Dendrites carry the incoming signal in the cell body.

The electrophysiological recordings are in the form of field action potentials (fAPs) or spikes which represent inter- or intra-cellular information transfer. This communication can be decoded to understand the complex neuronal network. For instance, neuronal spikes can be recorded from several neurons and the frequency, amplitude and shape of the spike can shed light on how the neuron is communicating with the neighbouring cells. Electrophysiology also finds application in drug development where the effect of a new drug can be studied on the specific ion channels based on the changes in the fAP upon injecting the test-drug in the cell culture medium.

Ion channels attract special attention from the pharmaceutical industry for drug screening, with adequate electrophysiology, where the effect of the specific compound on the cellular activity is studied [7]. Furthermore, brain functions such as learning, memory acquisition and retrieval as well as speech recognition depend on the synchronised activity of neurons in space and time. Diseases like Alzheimer's, epilepsy and other psychological impairments (depression, obsessive compulsive disorder [8]) are caused by biochemical or electrical abnormalities in the brain [9]. MEAs find applications in the retina research with retinal waves, neuronal coding and inter-neuron communication studies being some of the examples [10].
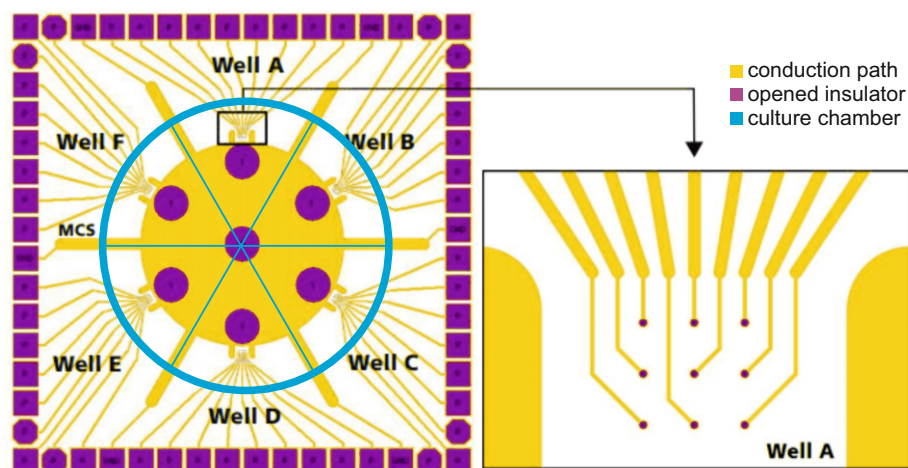
Figure 2.1 Schematic 6-well MEA with 6-electrode fields (wells) comprising 9 electrodes each with cell culture chamber (blue) atop.

A typical MEA consists of a base substrate (either float glass or polyimide in the case of flexible MEAs) on which the conduction paths and electrodes are fabricated. MEAs with different electrode dimensions and layouts can be customized and produced for a wide range of applications. Figure 2.1 shows a schematic of a 6-well MEA where 6 simultaneous experiments are possible with 9 electrodes (recording

sites) each. The conduction paths leading up to the microelectrodes are insulated to ensure that only the electrodes are in contact with the culture medium and the cells. This is especially important for single unit recording which means electrical recording obtained from a single cell. Also, the insulator must be thick enough to avoid shunt capacitance. A glass ring (cell/tissue culture chamber, blue circle in figure 2.1) is glued atop the array of microelectrodes and electrical activity is recorded when cells come either in direct contact or in the vicinity of the electrode.

The MEAs, since their introduction in 1972 [11], are constantly developed and adapted for novel applications [8, 12–14] with *in vivo* electrophysiology [15, 16], high density CMOS-based MEAs [10] and new electrode shapes or materials [17, 18] being some of the examples. Choosing the right material for the electrode, conduction path and insulator is crucial in order to obtain high quality measurements. MEAs are fabricated with the aim of lowering the impedance to improve the signal-to-noise ratio. The typical electrode materials are TiN [1], Pt [2], Au [3], IrO_x [4, 5] and more recently PEDOT:PSS-CNT [6], as well as other carbon based materials graphene [19, 20], graphene oxide [21], CNTs and diamond. Impedance magnitude at 1 kHz is often used as the quality control norm as the maximum neuronal activity (firing rate) is reported around this frequency [22]. It is important to consider that the impedance is microelectrode dimension dependent and hence the value at only one frequency is not enough for realistic and fair comparison. For a better overview, the specific impedance which is the product of impedance magnitude at 1 kHz and electrode area is used here. The commercially available TiN electrodes, produced by NMI TT GmbH and distributed by Multi Channel Systems GmbH, display a specific impedance of $1.4 \, \Omega \, cm^2$ [23]. The specific impedances of carbon based microelectrodes are discussed in section 2.4.

2.2 Why transparent electrodes?
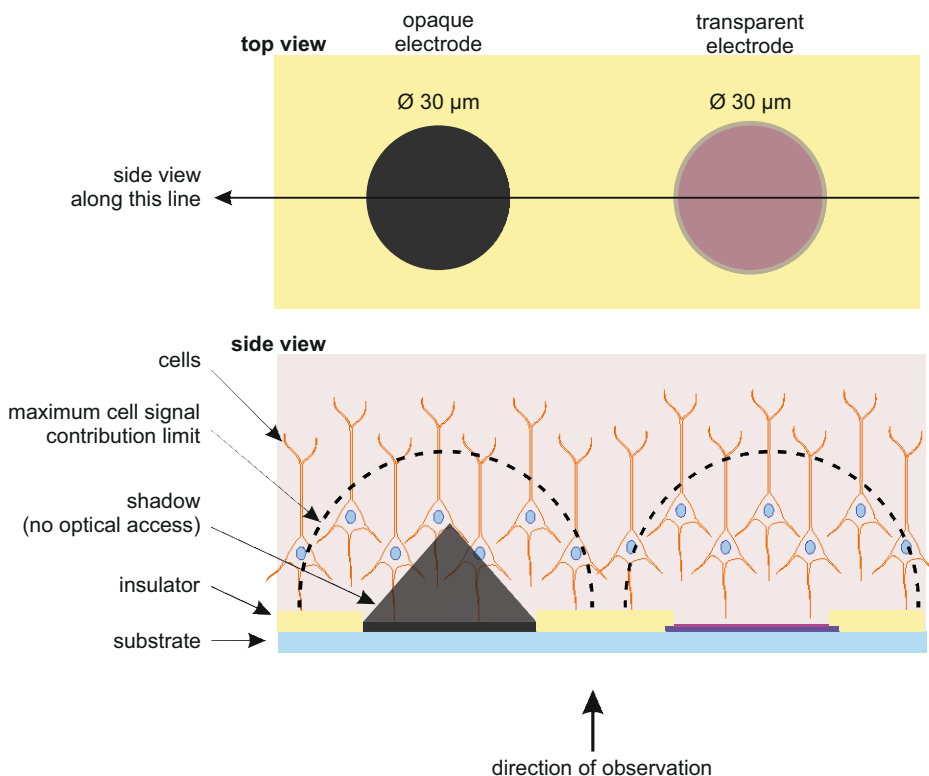
Figure 2.2 The cells closest to the opaque electrode (left) are shadowed. A transparent electrode (right) allows unobstructed optical access to the cells and offers the possibility to optically stimulate these cells. [Modified from [24]]

During electrophysiological measurements, the optical access is possible only from the substrate side as the cell culture medium is on top of the electrode (see figure 2.2). Conventional electrode materials obstruct the field of view. This can be addressed by 3D imaging of the cell culture where the Z-stack

of the X-Y planes is collated offering a 3D view of the system. However, with opaque materials the closest cells to the electrode are shadowed and this shadow is also visible in the 3D image. The extent of the shadowing depends on the dimension of the electrode, the objective used for the optophysiology and the numerical aperture. A typical 30 μm diameter electrode casts a ∼20 μm shadow through a 20x objective with 0.8 numerical aperture and 1.35 refractive index (see figure 2.2). The distance of active cells from the electrode is crucial as the signal amplitude diminishes with distance from the electrode. For example, in the case of neurons the maximum recorded activity (>60 μV) is from the cells within a ∼50 μm [15] radius from the electrode (dashed semicircle in figure 2.2). This loss of information can be countered by using transparent microelectrodes.

Electrophysiology coupled with optical investigation is an emerging field with optogenetics and calcium imaging being recent examples. Optogenetics is an elegant approach where 'reverse engineering' is applied in biology. Optics and genetic engineering come together to provide a deeper insight into the information transfer and exchange among neurons [25–27]. Calcium imaging is a promising technique for detailed understanding of the neuronal networks either in combination with MEAs or solo. Different types of neurons have different activities in neuronal networks and hence for precise understanding of the neuronal network, calcium imaging has been reported as a beneficial tool [28]. Both, optogenetics [26] and calcium imaging [29] have revolutionized neuroscience by enabling systematic and precise recordings *in vivo* and *in vitro*.

Transparent electrodes allow for simultaneous electrophysiology and optical imaging. This is essential for the advancement of the neural research field and opens up new possibilities for investigating the brain functions which could further improve therapeutic neural interface applications [20]. Carbon based materials such as carbon nanostructures and graphene are potential electrodes owing to the high surface area of the former and optical transparency of the latter. The next section briefly introduces the carbon materials used in this work.

2.3 Materials of interest

2.3.1 Carbon nanostructures

Electron microscopic images of helical microtubules of graphitic carbon were first published in 1991 [30], six years after the C_{60} fullerene synthesis was reported. These tubular carbon structures were concluded to be formed by rolling up single hexagonal carbon sheets instead of the Bacon's scroll model [31] for tubular needle growth. These carbon nanostructures, popularly known as CNTs, created a new wave of interest owing to their extraordinary mechanical, thermal and electrical properties. The Young's modulus and tensile strength of CNTs is five and fifty times higher than steel, respectively [32]. They show excellent thermal conductivities and ballistic charge transport compared to most known materials. It is important to note that these extraordinary properties are usually assosicated with purely single walled CNTs (SWCNTs) while multi-walled CNTs (MWCNTs) display inferior properties [33].

CNTs are one-dimensional structures consisting of sp^2 hybridized carbon atoms forming a hexagonal network. Every carbon atom is covalently bound to three others with a 120° angle and a 1.42 Å bond length. While three of the valence electrons are located in the three covalent bonds, the fourth one is located in the π orbital orthogonal to the sp^2 plane. The overlap of the π orbitals of the adjacent atoms in a given plane leads to the electron bond network which results in high charge mobility and hence, improved conductivity. Figure 2.3 shows tubular nanostructures grown at 600 °C and observed using a helium ion microscope. SWCNTs have diameters in the range of few nanometres which increase for MWCNTs depending on the number of rolled up carbon layers. Among other parameters like the base substrate, catalyst and carbon source, the production of CNTs by catalytic chemical vapour deposition demands temperatures over >600 °C. Below these temperatures, carbon tubular structures with thicker diameters mixed with amorphous carbon are obtained.

These carbon nanostructures are reported to have a wide range of biological applications. [34, 35] More details on the application of CNTs in the biomedical field and the interfacing with biology can be found here [36]. The high surface area of the carbon nanostructures lowers the electrochemical impedance which is essential for improved electrophysiology. However, the electrical properties of the CNTs come at the cost of optical transparency. Hence, one of the main challenges of this work was
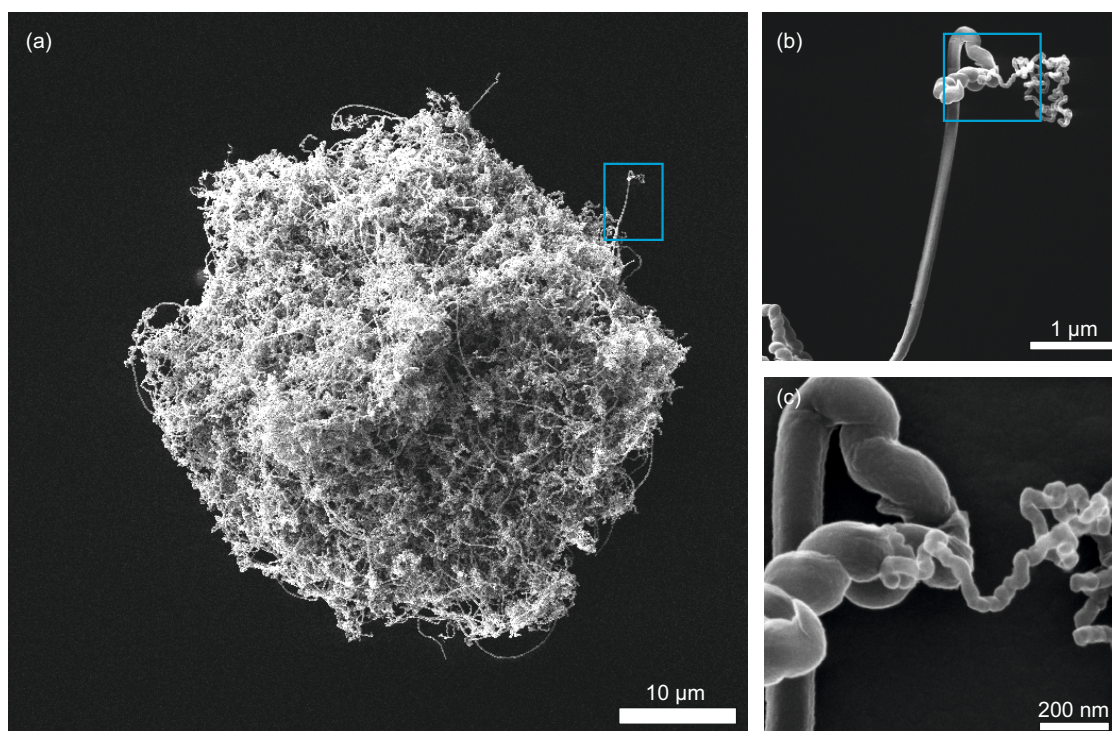
Figure 2.3 Tubular carbon nanostructures produced at 600 °C and observed with helium ion microscope.

to balance the carbon nanostructure production parameters and optical transparency while maintaining low impedance.

2.3.2 Graphene

Graphene is a two-dimensional hexagonal lattice of carbon atoms (see figure 2.4 (a)). Since its first isolated preparation in 2004 [37], graphene is one the most extensively researched materials of the recent decades. Ballistic electron transport [38, 39], exceptional thermal conductance [40], superior mechanical properties [41], impermeability to gases [42] and supreme transparency (close to 98 % for monolayer graphene [43]) are few of the superlatives associated with this wonder material. Chemical vapour deposition (CVD) growth of graphene is a popularly used production method.

The entry of graphene into the field of biomedicine is only a decade old. The application of a derivative of graphene, nano graphene oxide, in drug delivery and cellular imaging has been reported in 2008 [45]. Since then, the application of different derivatives of graphene has been reported in the field of biosensing [46]. A field effect transistor for sensing cellular signals from cardiomyocytes using mechanically exfoliated single layer graphene was reported in 2010 [47]. Recently, single layer graphene was reported to tune the neuronal excitability [48].

Graphene synthesis and application is reviewed here [49]. The main advantage of using graphene in the MEA technology is the optical transparency ($\sim$97 % for monolayer graphene) which is an improvement over CNTs, although the electrochemical properties of graphene need in-depth investigation. Graphene microelectrodes reported in the MEA technology are discussed in section 2.4.

2.3.3 PEDOT:PSS

Poly(3,4-ethylenedioxythiophene), PEDOT, was developed and patented by the Bayer AG in the second half of the1980s. Water soluble poly(styrene sulfonic acid), PSS, was subsequently used as the charge-balancing dopant during the electropolymerization of EDOT into PEDOT:PSS. [50] The chemical structure of PEDOT:PSS is shown in figure 2.5. This combination has gathered increased interest from both fundamental researchers and industry. PEDOT:PSS displays good thermal stability, the possibility of
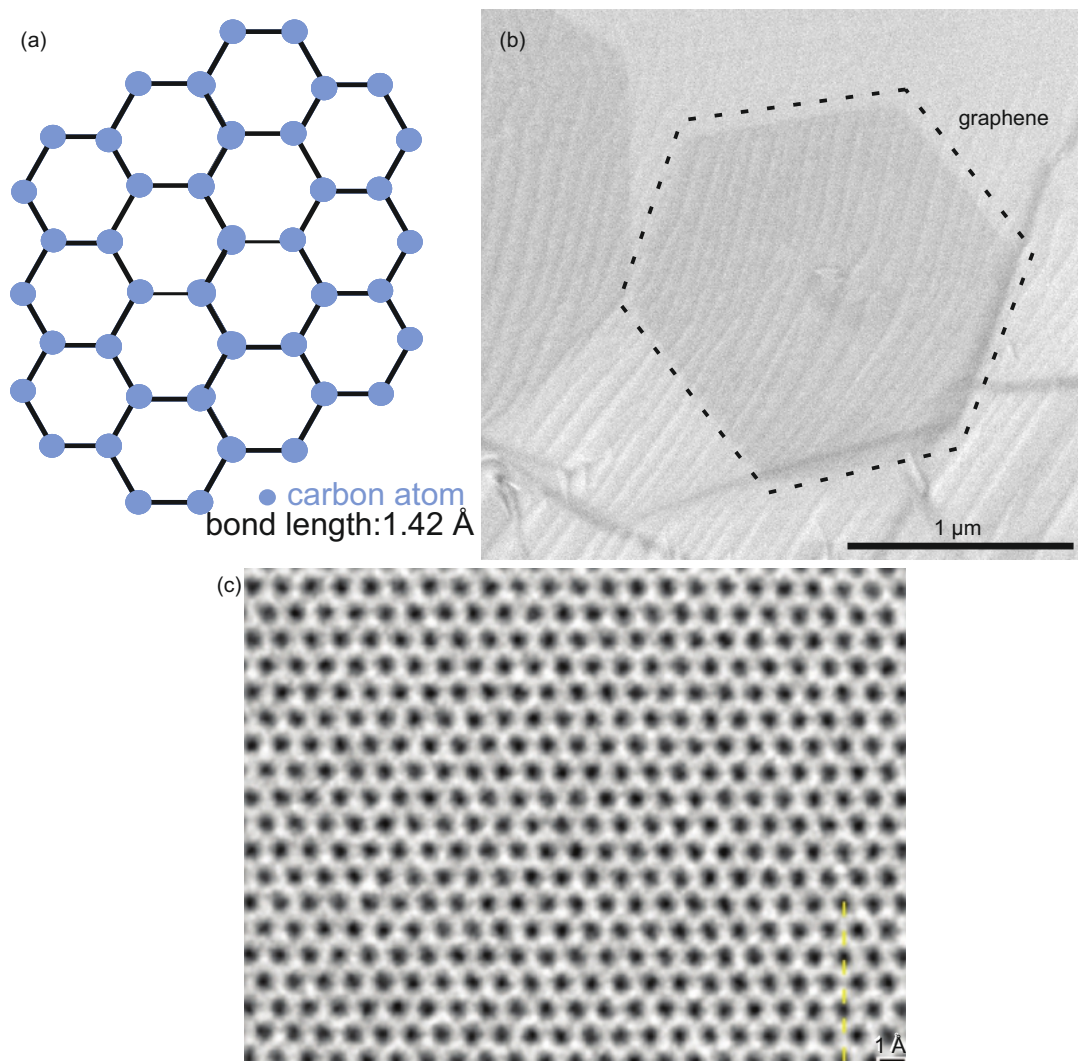
Figure 2.4 (a) Hexagonal graphene with 1.42 Å bond length. (b) Scanning electron micrograph of graphene grown on Cu by chemical vapour deposition. (c) One of the first transmission electron microscopic images of single layer graphene (Reprinted with permission from [44]. Copyright 2018 American Chemical Society.)

transparency, adequate film-forming properties and tunable conductivity [51]. The commercially available PEDOT:PSS solution can be spincoated on the desirable substrates for a wide range of applications ranging from organic light-emitting diodes, organic photovoltaic devices to transparent conductive oxides [52]. Electropolymerization of EDOT into PEDOT in a PSS-containing electrolyte is another way of producing PEDOT:PSS films. A controlled amount of current, necessary to initiate the polymerization process is passed through the electrochemical cell. The electropolymerization mechanism is not completely understood. Following is the description adapted from [53] and the polymerization scheme is shown in figure 2.6.

A resonance stabilized cation radical forms when the applied potential exceeds the oxidation potential of the monomer (figure 2.6 (a)). The cation combines with a second radical to form a dimer which is (thermodynamically) stabilized due to the loss of two protons (b). The larger delocalized system in the dimers makes them susceptible to oxidation and hence forming the radicals at lower potential. The same principle applies to trimers and oligomers. The radical formation from the monomers, dimers and larger oligomers, and the recombination with one of their kind or reacting with a neutral monomer or oligomers makes the electropolymerization a complex mechanism. Possible reactions are presented in
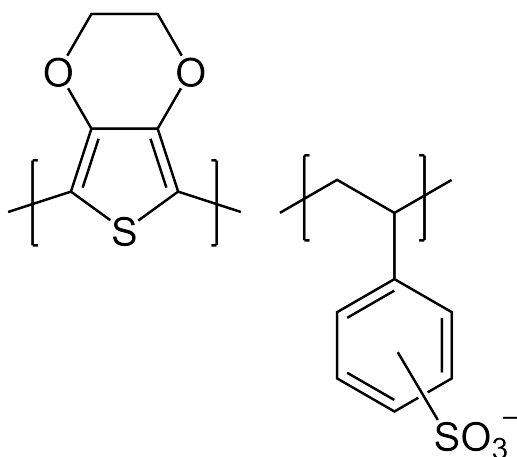
Figure 2.5 Chemical structure of PEDOT (left) and PSS (right).

figure 2.6 (c,d). The positive charge remains at every third or fourth repeat unit and requires balance by anions which diffuse into the polymer during polymerization.

In MEA technology, PEDOT:PSS is often used to reduce the impedance of the microelectrodes in *in vivo* and *in vitro* applications [54–57]. In this work, the conducting polymer was used to combat high impedance of graphene and develop microelectrodes for a wide range of applications.
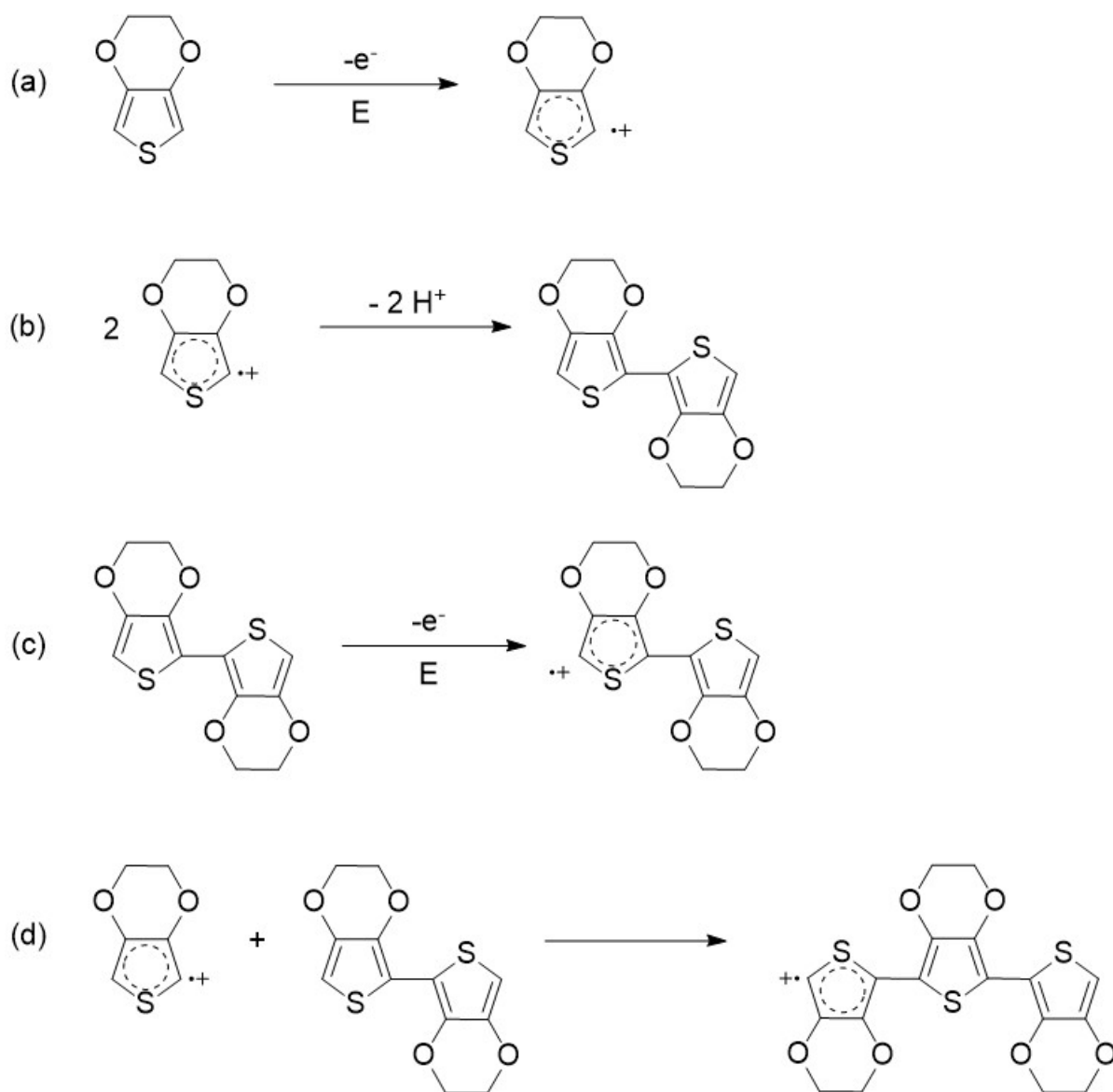
Figure 2.6 EDOT electropolymerization scheme. [Modified after [53]]

2.4 Carbon materials in MEA technology

The entry of carbon based materials into the MEA technology is only a decade old. Opacity and light-induced artefacts in the electrical recordings are the two main reasons behind exploring new MEA electrode materials. As explained in section 2.2, conventional electrode materials are opaque and cast a shadow while imaging the cells either in transmission mode or with the inverse microscope. The light induced artefacts result from the photoelectric effect which is the emission of electrons from the metallic surface in response to light. These artefacts can look like the local fAPs or a spike which are similar to the electrical activity of the cells. This may lead to the artefacts being (mis)interpreted for cellular recordings. Moving the light away from the opaque electrodes or shielding them from the light by other means can prevent the artefacts, but both are not possible in optogenetics where the cells are in close vicinity or directly on top of the electrode. Graphene based materials are reported to show no light-induced artefacts and hence are a step ahead of the conventional metal based electrode materials [58].

As previously mentioned, the impedance is used as the benchmark for a potential electrode material, and the magnitude impedance at 1 kHz is reported as the neuronal activity appears on a length scale of ~1 ms [22]. The reported carbon based MEAs have different shapes and dimension. Hence the specific impedance is calculated for the different materials for a better overview and comparison between the materials (see table 2.1). The all-CNT microelectrode was reported to have ~8 fold higher specific impedance than the CNT grown on TiN to reduce the impedance. The focus was on electrical properties and not on optical transparency. Graphene-based microelectrodes where chemical vapour deposited graphene films were transferred on flexible substrates for *in vivo* electrophsiology combined with optogenetics [20] and calcium imaging [19] were reported in 2014 .

The high surface area and the electronic properties are the main motivations behind using CNTs in biological and biomedical applications. CNTs grown on TiN [59, 64] and flexible substrates [60, 65] are reported to improve the electrical properties. In other cases, modified CNTs coated on tungsten and steel wires were observed to improve the neuronal recording [66].

The same group, David- Pur *et al.,* reported a flexible all-CNT MEA where the contact pads, conduction paths and electrodes were made of CNTs on a flexible substrate [60]. In both cases the focus was on reducing the impedance and no transmittance studies were reported.

Four-graphene layers with 200 μm diameter electrodes displayed magnitude impedance of (243 ± 6) kΩ at 1 kHz. The cell dimensions are in tens of μm and hence the large electrode records contributions from more than one cell which is often not desirable. Here, the 3-D imaging of the cells on top of TiN (opaque) and graphene (transparent) microelectrodes clearly showed the shadow-effect of the former. 3-D imaging was thought to be an alternative for visualizing cells cultured on the opaque electrode but the shadow effect hinders the imaging. This supports the need for transparent electrodes.

Nitrogen doped graphene microelectrodes of 50×50 μm^2 with Au conduction paths [19] and graphene coated Au microelectrodes [62] were reported to show 13 Ω cm^2 (10 fold higher than the commercially available TiN) specific impedance with the former being transparent. In another case, recently platinum nanoparticles coated on graphene were reported to show specific impedances in the range of 87–0.14 Ω cm^2 [63].

Electrode material	specific impedance ($\Omega*cm^2$)	optical transparency (%)	publication
TiN	1.4	NA	[23]
CNT (Ni) on TiN	0.5	NA	Gabay et. al. [59]
CNT (Ni) on flexible substrate	4.3	NA	David-Pur et. al. [60]
Nano crystalline diamond	2.1	50	Mcdonald et. al. [61]
CLEAR device (4 graphene layers)	76	90	Park et. al. [20]
doped graphene	13	80	Kuzum et. al. [19]
graphene on Au	13	NA	Koerbitzer et. al. [62]
graphene on PET	96	80	Thunemann et. al. [58]
Pt nanoparticles on graphene	87 - 0.14	95-30	Lu et. al. [63]

Table 2.1 Table summarizes the electrode materials, specific impedance (product of impedance magnitude at 1 kHz and micro-electrode area), optical transparency and the corresponding publication.

3 Materials

3.1 Production of Carbon Based Materials

3.1.1 Catalyst and carbon deposition

In this work, carbon deposition was optimized and analysed on 1 mm thick float glass substrates ($5 \times 1\,cm^2$) sputter coated with a 200 nm indium tin oxide (ITO) layer. The catalysts, Fe and Ni, were deposited using a Cressington sputter coating system in argon (Ar) atmosphere at 0.05 mbar with a plasma power of 30 W for 8 s, corresponding to $\sim$5 nm layer thickness. For process optimization, the influence of temperature on the carbon deposition was studied from 400 °C to 600 °C with 50 °C step. The temperatures reported here were measured on the heating plate upon which the 1 mm thick float glass substrates were placed. In a modified Leybold Z401 vacuum system, the target temperature was ramped at $\sim$200 °C min^{-1} in presence of 200 sccm ammonia (NH_3) and the substrates were held at the target temperature for 10 min upon which 200 sccm acetylene (C_2H_2) was injected and the pressure was set to 5 mbar. After 10 min process time the gas flows were shut and the heater was switched off. The chamber was vented on reaching 200 °C by injecting nitrogen and the substrate removed. [67]

The carbon deposition on atomic layer deposited (ALD) Ni as catalyst was studied as part of the Carbon4Health project which was a 3 yr project with the goal of producing transparent carbon-based electrodes for *in vitro* and *in vivo* biomedical and life science applications. 200 nm ITO on float glass substrates was covered with a photoresist (S1818, Shipley Corporation, US) and photolithography opened squares in the resist. Ni was deposited at Plasma Electronic GmbH by means of plasma enhanced ALD where Bis(ethylcyclopentadienyl) nickel (II) served as the precursor. The Ni precursor was subjected to cycles of oxidation (water plasma) and reduction (hydrogen plasma) at 155 °C yielding a $\sim$3 nm layer. ALD-Ni deposition was followed by resist lift off leaving squares of Ni on the ITO/glass substrate. Carbon was deposited following the process described above with 550 °C as the process temperature. [68]

3.1.2 Graphene production

Graphene was grown on commercially bought Cu foil from Alfa Aeaser GmbH (foil number 13380). This particular foil was chosen based on results described in [69]. Cu was pre-treated with 1 M ammonium persulfate (APS) in ultrasonic bath for 1 min, followed by de-ionized water cleaning (twice) and isopropanol rinse. The Cu foil was then carefully dried with a nitrogen gun without bending it, placed in the Black Magic (Aixtron) machine, and the chamber was pumped down to 20 mbar. The temperature was increased from room temperature to 800 °C with a 200 °C min^{-1} ramp in the presence of 200 sccm Ar. After the desired temperature was reached, Cu was held (annealing) for 5 min followed by the introduction of 200 sccm H_2 and 100 sccm CH_4 for 5 min. The temperature was then lowered with a 200 °C min^{-1} ramp in the presence of 200 sccm Ar, and the chamber was vented upon reaching 200 °C.

3.2 Integration in the MEA technology

3.2.1 Carbon nanostructures MEA fabrication

1 mm thick $49 \times 49\,mm^2$ glass substrates were coated with 200 nm ITO followed by photolithography with a S1818 resist mask and a dry etch process in H_2/CH_4 plasma producing ITO conduction paths and contact pads. After resist removal, a 500 nm thick silicon oxide (SiO_x) was deposited by plasma-enhanced chemical vapour deposition (PECVD) followed by application of the second resist mask (AZ 3027 ECI). A dry etch CF_4/O_2 plasma opened the contact pads (purple squares along the edges of the

resist

SiOx

ITO

glass

MEA substrate was fabricated utilizing ITO conduction paths and SiO$_x$ insulator with established cleanroom processes.

30 µm

30 µm diameter electrodes are opened in the resist by photolithography, SiO$_x$ removed by reactive ion etching and the resist was left on the insulator.

A thin catalyst layer of Ni or Fe (5 nm) was deposited by physical vapour deposition.

Resist lift-off left catalyst layer on the electrodes.

Carbon was deposited with acetylene as carbon source in ammonia atmosphere.
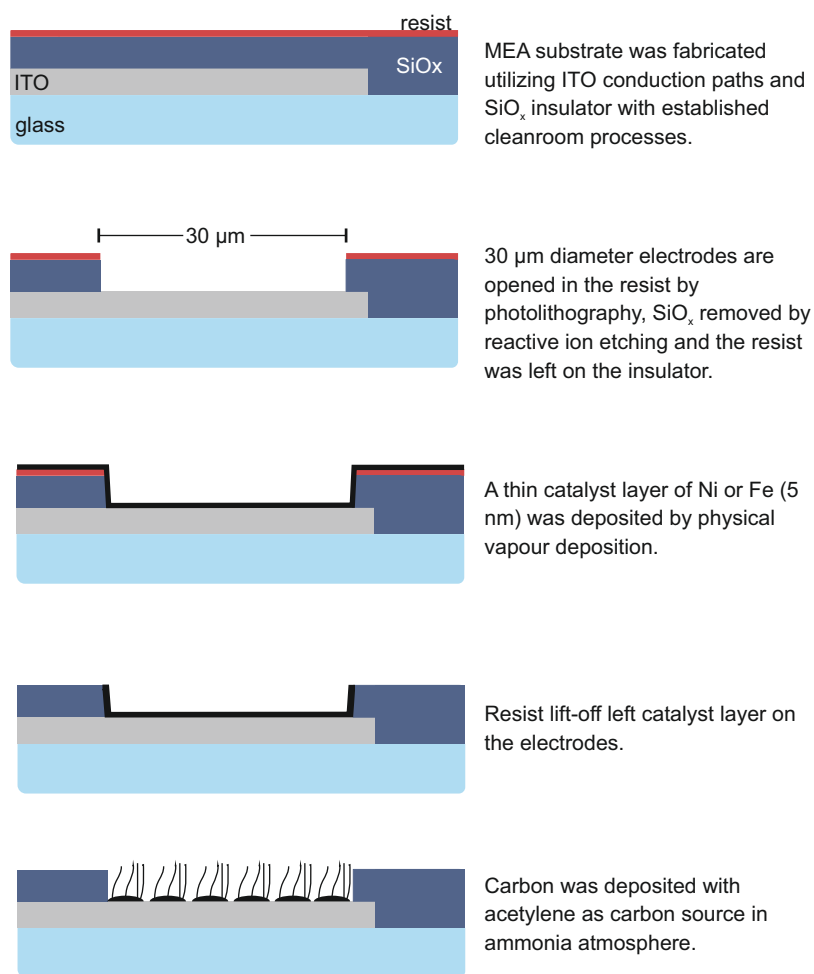
Figure 3.1 Carbon MEA fabrication scheme for producing 30 µm carbon nanostructure electrodes on ITO conduction paths with SiOx as insulator on 1 mm thick glass base substrate.
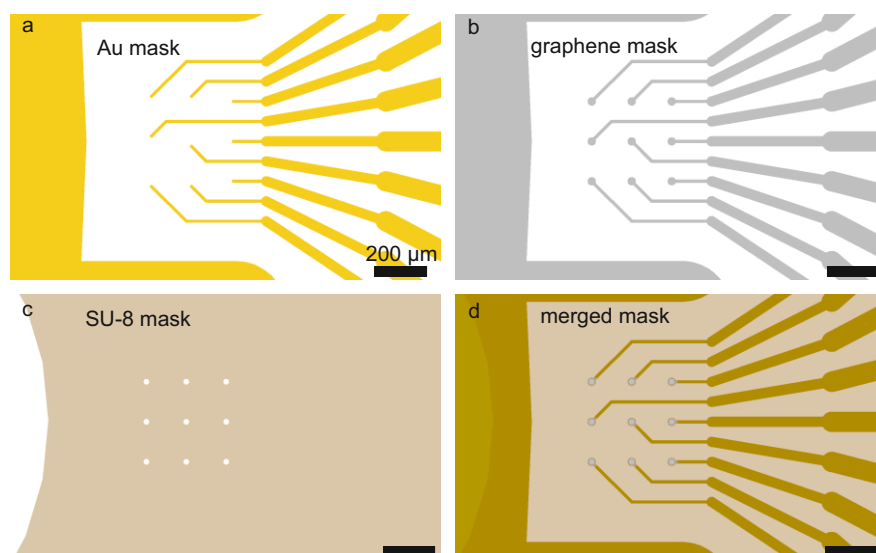
Figure 3.2 Photolithography masks for different graphene MEA fabrication steps. Au (a) and graphene (b) are structured using positive resist. SU-8 (c) is a negative resist. (d) Merged masks show the expected results, yellow being Au and grey being graphene.

MEA substrate in figure 2.1) and the electrodes (see figure 3.1). The resist mask at this point was used for catalyst lift off. The processes until this point were done by the clean room team at the NMI. Carbon deposition catalyst, Ni or Fe, was sputter deposited as described in section 3.1.1 and carbon nanostructures deposited at 550 °C or 600 °C.

3.2.2 Graphene MEA fabrication

200 nm Au was sputter deposited on glass substrate, and structured by photolithography using the mask shown in figure 3.2 (a) by the clean room team at the NMI. A polymer-based transfer was implemented to transfer graphene from Cu to Au conduction paths. For this purpose, Poly(methyl methacrylate), PMMA, was spin coated on the Cu-graphene foils with 5 s at 500 rpm and 30 s at 3000 rpm, followed by baking at 120 °C for 2 min. The assembly was cut into pieces of the desired dimensions with a scissor which bent the Cu foil. The pieces were flattened by pressing between two cleaned microscopic glass slides. 1 M Ammonium persulfate (APS) solution in de-ionised (DI) water was used for etching the Cu. The flattened Cu pieces were carefully suspended on the surface of the Cu etchant. The top-side of the Cu pieces was marked to make sure only the bottom is exposed to the APS solution. The mark is also useful in locating the transparent PMMA-graphene membrane floating in the solution which turned light blue from the dissolved Cu. The thin delicate membrane was fished out of the APS solution using a clean glass slide and released in DI water twice where it floated on the surface. The membrane was carefully placed on the target region (electrode field) making sure it overlaps with the Au conduction paths. Water trapped between PMMA-graphene and the MEA substrate was carefully removed using an air gun. The substrates were dried overnight and PMMA was removed in acetone (30 min) and isopropanol (5 min) followed by air gun drying.

Figure 3.3 shows selected graphene MEA fabrication steps. The graphene transferred onto the Au conduction paths and the electrode field was examined with scanning electron microscope (SEM). Graphene was structured into ~40 µm diameter electrodes by the clean room team using the mask shown in figure 3.2 (b). The structuring was done by photo-lithography using S1818 resist and etching the unwanted graphene with oxygen plasma (200 W, 100 mTorr, 3 min).

The SU-8 insulator deposition was done by Dr. Peter D. Jones. Prior to insulator deposition, the substrates were baked for >1 h at 150 °C, then removed from the oven and cooled to room temperature immediately before spin-coating. SU-8 3005 was spin-coated for 10 s at 500 rpm then 30 s at 4000 rpm, soft baked for 5 min at 95 °C on a hotplate, exposed through a photomask (700 mJ cm^{-2}, i-line, SÜSS
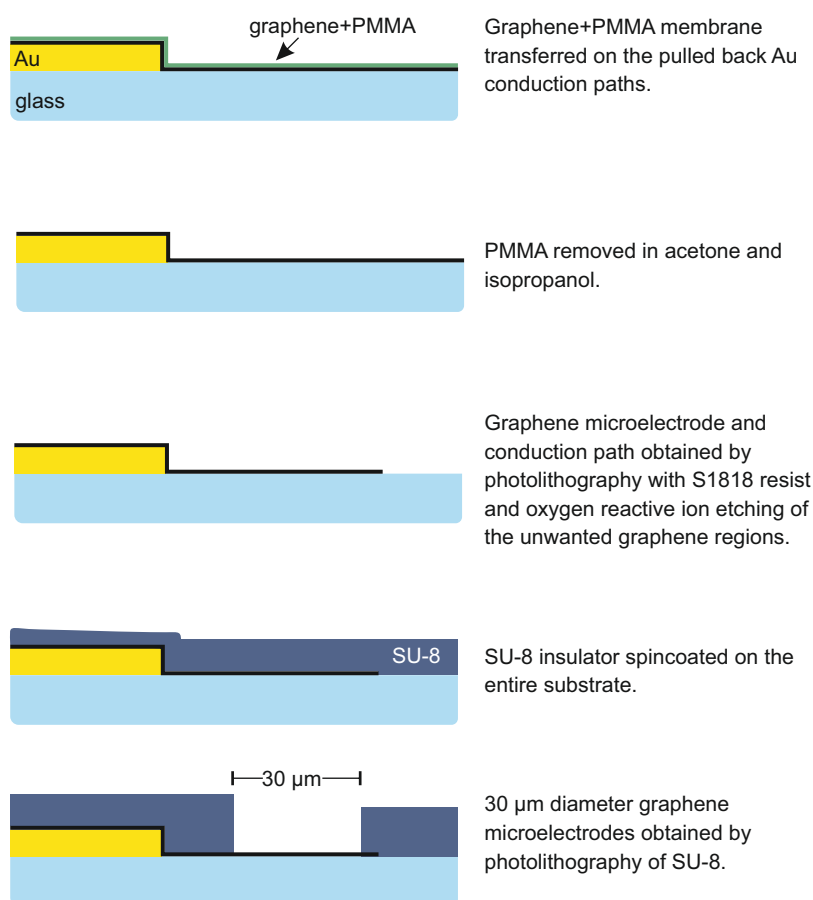
Figure 3.3 Graphene MEA fabrication scheme producing Au conduction paths leading up to 30 µm diameter graphene electrodes with SU-8 insulator on 1 mm thick glass.

MA6, pattern in Figure 3.2 (c)) and post-exposure baked for 5 min at 95 °C. SU-8 was developed for 1 min in mr-Dev 600 and rinsed with isopropanol, then substrates were baked at 170 °C for 30 min in an oven. The substrates were ramped from and to room temperature. The result was 40 µm diameter graphene microelectrodes with Au conduction paths and SU-8 insulator with 30 µm openings.

3.2.3 Graphene/PEDOT:PSS MEA fabrication

Ethylenediethoxythiophene (EDOT, Aldrich USA) was mixed in 1 % poly (sodium p-styrenesulfonate) (NaPSS, $M_w \approx 70\,000\,g\,mol^{-1}$, Acros organics USA) producing 0.02 M solution. The recipe was modified from [53]. Electropolymerisation was achieved by passing 15 nA current through the graphene microelectrodes for controlled durations of 0.2 s, 0.5 s, 1 s, 2 s, 5 s and 10 s. The representative electrodeposition cell is shown in figure 3.4 (a). Figure 3.4 (b) shows the recorded potential vs the deposition time for 1 s, 0.5 s and 0.2 s. Charge passing through the microelectrode can be calculated following the equation 3.1. Furthermore, PEDOT:PSS film thickness can be estimated by extrapolating the thickness vs charge curve
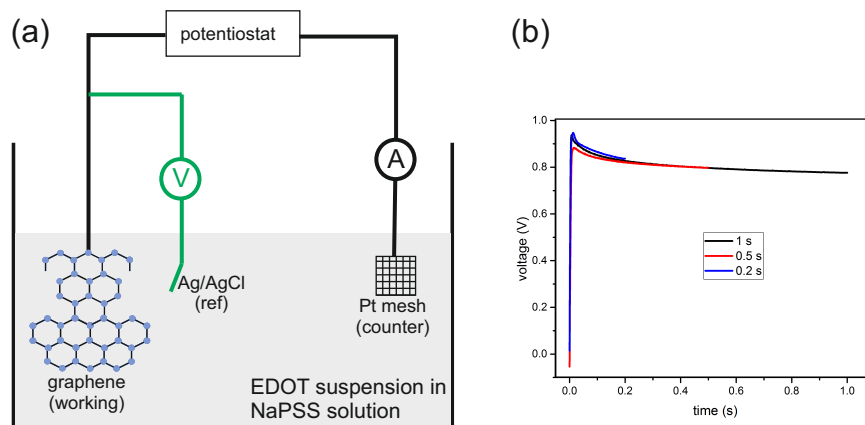
Figure 3.4 (a) Representative PEDOT:PSS electrodeposition cell where graphene is the working electrode with Ag/AgCl as reference and a Pt mesh as the counter electrode in NaPSS+EDOT electrolyte. (b) Recorded voltage when 15 nA current was applied for 1 s, 0.5 s and 0.2 s.

from the dissertation of Dr. Ramona Samba [53] (see figure 3.5).

$$Q = I * t \tag{3.1}$$

where Q is charge in Coulomb, I is current in Ampére and t is electrodeposition time in seconds. In this work, 15 nA current was passed for controlled durations of time.
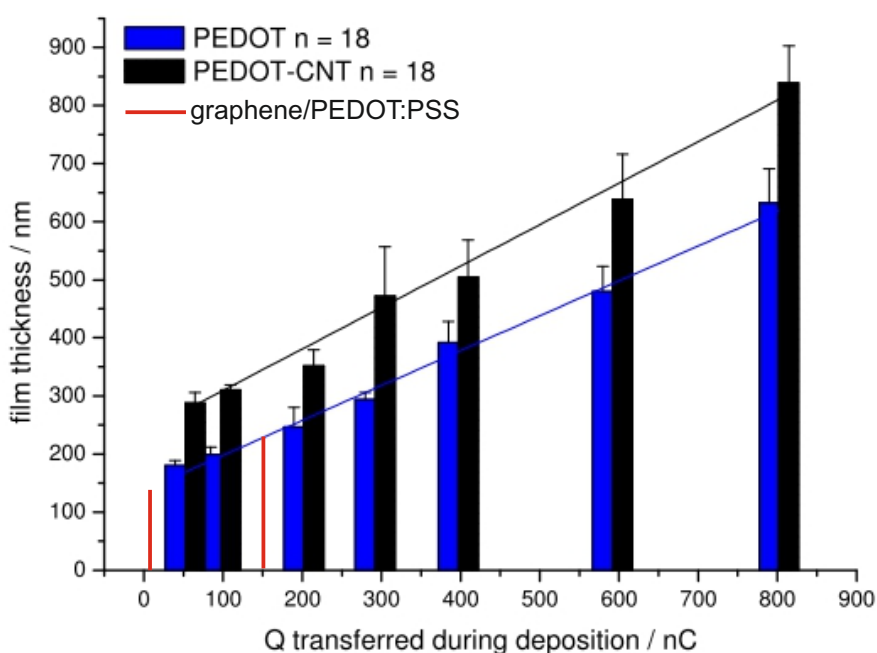
Figure 3.5 PEDOT:PSS film thickness vs the charge transferred during the electrodeposition. The red vertical lines indicate charge transfer for the longest, 10 s (150 nC), and shortest, 0.2 s (3 nC), deposition times used in the present case. The graph is modified from doctoral dissertation of Dr. Ramona Samba [53].

Electrochemical impedance spectroscopy and cyclic voltammetry were performed before and after PEDOT:PSS deposition to understand and analyse the contribution of PEDOT:PSS on the graphene microelectrodes.

3.3 Cardiac cell culture and retina slice

3.3.1 Cardiac cell culture on MEA

Cardiomyocytes were cultured on all three electrode types - carbon nanostructure, graphene and graphene/PEDOT:PSS in the lab of Udo Kraushaar. The MEAs were sterilized in ethanol and subsequently coated with nitrocellulose (Roth, Germany, HP42.1) from methanol solution. MEAs were plated with 20.000 cells/µl density and the cells, when healthy, began showing autorhymic activity from 3–4 d. During this time the cells were maintained at 37 °C in 100 % humidity.

3.3.2 Cardiomyocytes-carbon interface ultrastructure

After recording the cardiomyocyte fAPs, the cells were chemically fixed on the carbon nanostructure MEA in 3 % formaldehyde and 2.5 % glutaraldehyde in phosphate buffered saline (PBS), stained with 1 % osmium tetroxide and 1 % uranyl acetate and embedded in epoxy resin. After embedding, the electrode field region was cleaved with a wire saw and ground down to ∼1 mm thickness and polished to achieve a smooth surface. The goal behind this study was to visualize the carbon nanostructure - biology interface and mechanical stability of the microelectrode. The analysis is detailed in section 4.2

4 Methods

4.1 Scanning electron microscopy
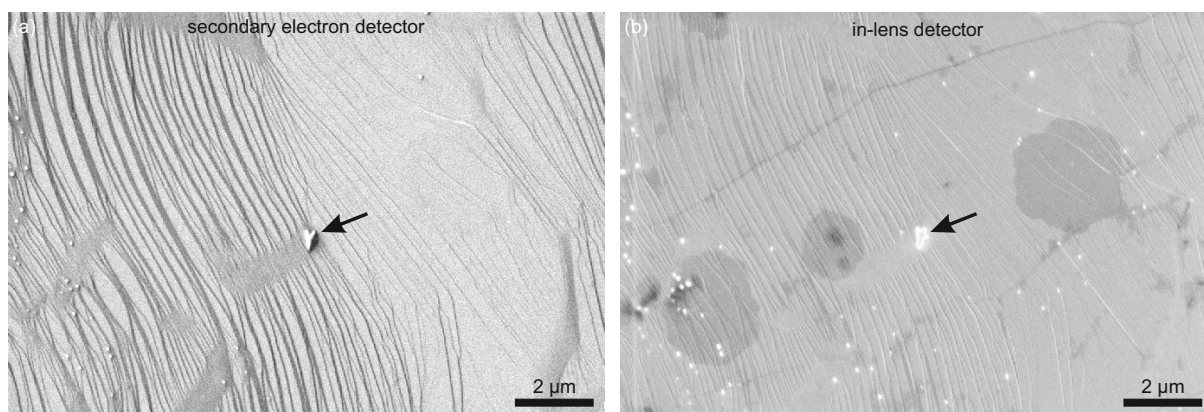
Figure 4.1 SEM images of graphene on Cu with (a) secondary electron and (b) in-lens detector. The arrow indicates one of the particles which are observed on the Cu foils after graphene production process.

Scanning electron microscopy (SEM) is popularly used for topological and elemental analysis. An electron beam with an accelerating voltage in the range of 0.02–30 keV interacts with atoms in the substrate producing a wide range of signals with topology and composition information. The secondary electrons (SE) collected by the in-lens detector located inside the beam column, in addition to the surface topography, show contrast corresponding to the work function of the substrate material. This is especially important in characterizing few layers of graphene with SEM. The in-lens image contrast is substantially better than that of the SE detector. As seen in figure 4.1 (a) the SE detector reveals the topography of Cu after the CVD process wherein the metal catalyst is subjected to 800 °C. The same region, when imaged with the in-lens detector, shows contrast between different layers of graphene (darker regions).

In the present work, the substrates were investigated using a Crossbeam AURIGA 40 (Zeiss) and Crossbeam X1540 (Leo) with 3 keV accelerating voltage.

4.2 Focused ion beam

Focused ion beam (FIB) milling is used in materials science and in biological fields to investigate layered structures, deposition and ablation of the material. The FIB set ups are often coupled with SEMs and use ion beams with high accelerating voltage. A focused beam of Ga^+ ions penetrates the substrate with currents in the range of 10 pA - 10 nA and can be used for cross-sectioning. A protection layer, e.g. Pt, protects the surface from the high energy ions and maintains the topological information.

A Pt protection layer of $\sim$100 nm was deposited using the gas injection system in the respective SEM chambers. FIB milling was started approximately in the center of the Pt layer making sure that the width of the cross section is > 1.5 times the depth of the final section. This ratio is important for visualizing the deepest substrate layer in the final FIB cross section. FIB milling was performed on ALD-Ni with and without the carbon nanostructures. Carbon MEAs produced at 550 °C and 600 °C were investigated by FIB cross sections. *In vitro* cultured cardiomyocytes on the carbon nanostructured microelectrodes were fixed and stained as described in section 3.3.2 followed by FIB milling at the edge of the electrode.

4.3 Energy dispersive X-ray spectroscopy

Energy dispersive X-ray spectroscopy (EDX) is used for elemental analysis, and the X-ray detector is usually coupled with SEM. High energy electrons upon hitting the atoms in the substrate eject an electron from the inner shell, creating an electron-hole. The hole is filled by an outer shell electron with higher energy and the energy difference results in generation of X-rays which are detected. The collected emission spectrum contains unique peaks corresponding to the chemical composition of the substrate. The bright particle indicated in figure 4.1 and ALD-Ni substrates upon carbon deposition were analyzed with EDX to identify the chemical composition. The beam energy used in both cases was 3 keV.

4.4 Time of flight secondary ion mass spectrometry (ToF-SIMS)

A focused ion (Cs^+ or Ga^+) beam ablates the substrate surface producing secondary ions. The created ions/particles are accelerated into a flight path towards the detector. Time between the ablation to detection (time of flight) can be measured and hence this technique offers very high resolution mass spectrometry. The strong ion beam can mill through the substrate producing three-dimensional elemental tomographs which offer comprehensive elemental information. This is especially important in characterizing few nm thin films. In this work, 3D ToF-SIMS tomographs were obtained from the ALD-Ni substrates to investigate the layer system before and after carbon nanostructure deposition.

4.5 Electrochemical Characterization

4.5.1 Electrochemical impedance spectroscopy

Impedance spectroscopy is a powerful technique used to examine the electrochemical processes in solids. A sinusoidal voltage is applied, and the ability of the electrical circuit to resist the electrical current is recorded. The resulting impedance (Z) is the contribution of a real (Z') and imaginary (Z'') part and the angle of the Cartesian is the phase (see figure 4.2). The magnitude impedance, calculated following equation 4.1, is plotted against the logarithm of the measured frequency. This type of plot is called Bode plot. The phase is often plotted on a second Y-axis. The shape and position of the resulting curve indicates the electrochemical characteristic of the system. For pure resistors, only the real part contributes to the magnitude impedance and for pure capacitors, only the imaginary part contributes.

$$Z = \sqrt{Z'^2 + Z''^2} \tag{4.1}$$

For simple circuits the expected and observed impedance curves are straightforward. The analysis becomes complicated when, for example, charge transfer resistance in the electrolyte, a constant phase element corresponding to the Helmholtz double layer capacitance and Warburg impedance representing the diffusion of the charge species are to be accounted for.
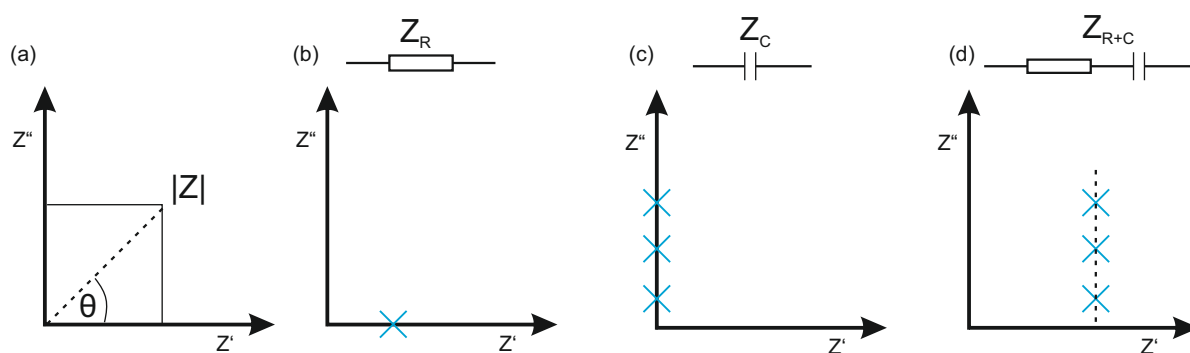

Figure 4.2 (a) Magnitude impedance includes the contribution of real and imaginary parts. Blue cross(es) indicates expected data position for pure resistor (b), pure capacitor (c), and a resistor-capacitor in series (d) for different frequencies.

For microelectrodes, magnitude impedance at 1 kHz is often used as quality control while investigating new materials. This particular frequency is chosen as the neuron firing rate is around 1 ms [22]. Lower impedance values are desirable as they correspond to low thermal noise. The correlation of impedance and noise is discussed in the next section. All three types of carbon materials were investigated by electrochemical impedance spectroscopy to characterize the electrical behaviour and estimate noise during biological recordings.

In the case of carbon nanostructure electrodes, electrochemical impedance spectroscopy was performed in PBS using a Solartron SI 1260 system. The electrode field was covered with a drop of ethanol to ensure good wetting of the hydrophobic carbon. Impedance spectra were obtained over the frequency range 1 Hz-1 MHz at 10 points per decade with 1 V amplitude against the internal counter electrode on the MEA substrate.

In the case of graphene and graphene/PEDOT:PSS microelectrodes, the impedance spectroscopy was performed with the potentiostat (VMP and VSP Bio-logic SAS, France) in a two-electrode set up where reference and counter electrodes were connected to the internal reference electrode of the MEA, which has a large area compared to the microelectrode, with the respective microelectrode being the working electrode in presence of PBS solution. The impedance and phase were recorded over the 1–10 000 Hz frequency range with 10 mV amplitude. The impedance magnitude and real impedance plotted against the measured frequency provide insights into the type of, capacitive or resistive, behaviour of the respective carbon materials.

4.5.2 Noise recording

An electrophysiology recording consists of the electrogenic signal from the cell and the noise. The signal detection is discussed in section 4.9. In a broad sense, the recorded noise is the combination of thermal (from the electrode), instrumental (internal electronics of the measurement set-up) and biological (isolation of the target cell by the surrounding cells) noise. The signal amplitude and noise are affected by the recording bandwidth, electrode impedance (defined by the electrode dimensions) and the density of the cells surrounding the recording electrode [70]. The total noise can be estimated following the equation 4.2 where v_t, v_b and v_i are the standard deviations of the thermal, biological and instrument noise, respectively.

$$v = \sqrt{v_t^2 + v_b^2 + v_i^2} \tag{4.2}$$

Biological noise is different for every system and its contribution is beyond the scope of the current work. The precise instrument noise is unknown but can be estimated to be $\sim 2\,\mu V$. The current flowing through the conductor is the result of the charge transfer which comes from the thermal agitation of the charge carriers. This agitation inside the electrical conductor is termed Johnson-Nyquist noise and can be quantified following the equation 4.3 where the thermal noise (v_t) is the square root of the Boltzmann constant (k_B), measurement temperature (T), and the real impedance over the measured bandwidth (Δf). Thermal noise levels are highly dependent on the electrode-tissue impedance (real impedance) and the selected bandwidth (wider bandwidth will increase the thermal noise levels) [70]. Lempka et al. reported that, theoretically, a wide recording bandwidth (100–10 000 Hz) resulted in 35 % and 25 % increase in the thermal noise and cell recording amplitude, respectively, compared to a narrow bandwidth (450–5000 Hz).

$$v_t = \sqrt{4 k_B T Z'_{avg} \Delta f} \tag{4.3}$$

$$Z'_{avg} \Delta f = \int_{f=1Hz}^{f=3500Hz} Z' df \tag{4.4}$$

In the present work, the real impedance data extracted from the electrochemical impedance spectroscopy described in section 4.5.1 was integrated over the recording bandwidth 1–3500 Hz (shaded region in figure 4.3) following the equation 4.4. The noise recordings were performed with the MEA 2100 (Multi Channel System MCS GmbH) system using PBS solution.
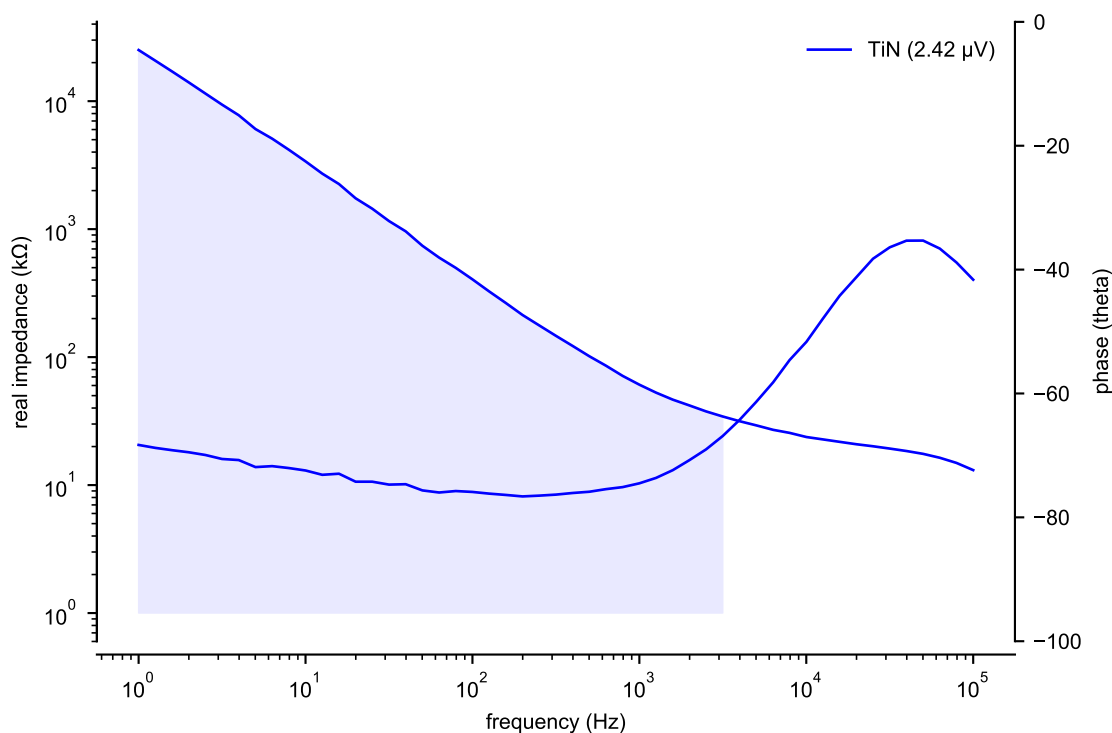
Figure 4.3 Real impedance and phase plotted against frequency for 30 μm diameter TiN microelectrodes. The real impedance is integrated over the shaded region which represents the noise measurement bandwidth (1–3500 Hz).

4.5.3 Cyclic voltammetry

Cyclic voltammetry (CV) is an electrochemical technique popularly used to investigate surface reactions such as adsorption. CV can also be used for electrochemical cleaning of metal surfaces prior to electroplating, electrodeposition, or evaluating the capacitance. The potential is varied between the start potential, E1, and the end potential, E2, with a particular scan rate. E1-E2-E1 marks one 'cycle' (see figure 4.4 (a)). The potentiostat measures current resulting from the applied potential and produces a plot between current and voltage (see figure 4.4 (b)). The system under investigation shows oxidation and reduction peaks which provides information about electrochemical properties.

The number of cycles is decided based on the electrode material, electrolyte and expected information. For example, when a certain material is under investigation for battery application, more than 500 cycles are applied. The amplitude of oxidation and reduction peaks (see figure 4.4 (b)) usually decreases with increasing number of cycles. This indicates loss of battery capacity. The capacitance is calculated following equation 4.5.

$$C = \frac{\int_{E1}^{E2} I dE}{\nu(E_2 - E_1)} \tag{4.5}$$

where C is the capacitance, E1 and E2 are the potentials limits, I the recorded current, and ν is the scan rate.

Graphene and graphene/PEDOT:PSS microelectrodes were investigated with CV using the same potentiostat as the electrochemical impedance measurements described in section 4.5.1. The two-electrode set up was identical to the impedance measurements. The voltage was swept from −0.8 V to 0.8 V with 200 mV s^{-1} scan rate. The capacitance was calculated following the equation 4.5 in the −0.5 - 0.5 V voltage range. The goal was to compare the capacitance for different PEDOT:PSS deposition times.
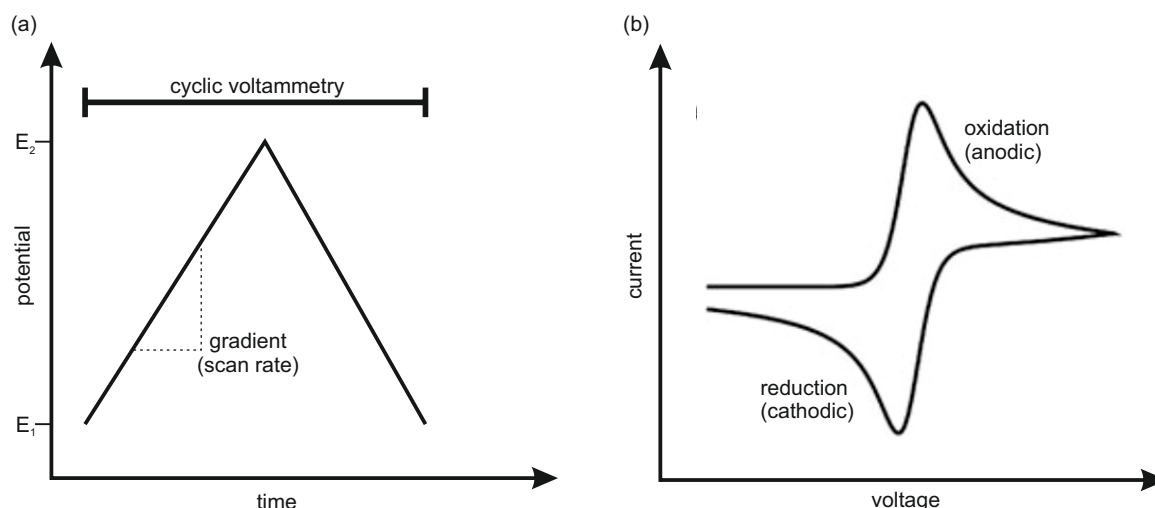
Figure 4.4 (a) One cyclic voltammetry (E1-E2-E1) cycle where the potential is increased at a certain scan rate. (b) CV curve shows the oxidation and reduction peaks.

4.6 Confocal Raman spectroscopy
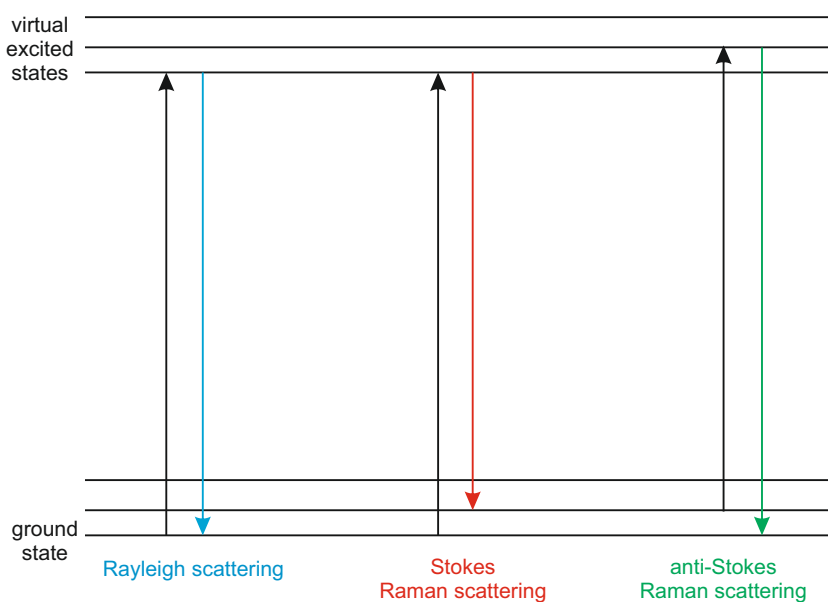
Figure 4.5 Schematic showing Rayleigh and Raman scattering processes.

The Raman effect, since its first experimental observation in 1928 [71], is widely used in chemistry, physics, materials science and biomedical research. Raman spectroscopy is a non-destructive and quick technique requiring minimal or no sample preparation. A laser source with a wavelength in the visible range of the electromagnetic spectrum irradiates the sample and most of the interaction is elastic (Rayleigh scattering), meaning the incident and scattered light have the same wavelength. A small percentage of the interaction is inelastic and the scattered light in this case is of different wavelength than the incident light. Rayleigh scattering is when the electron in the ground state is excited by the incoming light and falls back to the original ground level without any energy change (see figure 4.5). On the other hand, in the case of Raman scattering the scattered light has either lower (Stokes) or higher (anti-Stokes)

energy. Stokes is where the electron is excited from the ground state and falls to higher energy state and hence the Raman scattered light has less energy (longer wavelength) than the incident light. On the contrary, anti-Stokes is where the the electron is excited from higher energy state which falls back to ground state and hence the Raman scattered light has more energy (shorter wavelength) than the incident light. The Raman spectra contain Raman intensity plotted against the Raman shift calculated following equation 4.6.

$$Raman shift(cm^{-1}) = \frac{1}{\lambda_0} - \frac{1}{\lambda_1} \tag{4.6}$$

where λ_0 and λ_1 are the incident and measured wavelengths, respectively.

In this work, Raman spectroscopy was used to distinguish between different types of carbon materials. The following sections describe the revealing of Raman spectroscopy in characterizing carbon based materials.

4.6.1 Raman fingerprint of carbon materials

Raman spectroscopy is used to distinguish between different forms of carbon. The honeycomb lattice of carbon atoms, either rolled up (carbon nanotubes) or a sheet (graphene), shows three major peaks – D ($\sim$1350 cm^{-1}), G ($\sim$1580 cm^{-1}) and 2D ($\sim$2700 cm^{-1}). The location, width and intensity of the peaks provide information about the quality (defects) and quantity of graphene layers. The details of the Raman characterization of graphene are explained in detail here [72–75]. The D-peak results from two scattering processes consisting of one elastic scattering event by defects of the crystal and one inelastic scattering event by emitting or absorbing a phonon. For the 2D peak both processes are inelastic scattering and two phonons are involved. The G band is the only band coming from a normal first order Raman scattering process in graphene. In the case of bilayer graphene, both the electronic and phonon bands split into two components with special symmetries. G- and 2D-peak positions change depending on the base substrate [76].

Optical visualization of graphene on layers of varying SiO$_2$ thickness was reported back in 2007. $\sim$90 nm and $\sim$280 nm were found to be ideal thicknesses with Si as base substrate [77]. Since then, graphene exfoliation on $\sim$300 nm SiO$_2$/Si wafers is a common practice. It is important to note that the number of graphene layer determination, based on the refractive index controlled optical contrast change, is merely indicative. This layer estimate must be confirmed by other characterization tools such as Raman spectroscopy, transmission electron microscopy, low-energy electron microscopy, low-energy electron diffraction or scanning tunneling microscopy. Among these techniques, Raman spectroscopy is the quickest with minimal sample preparation requirement and non-destructive.

Figure 4.6 (a) shows individual Raman spectra obtained from substrate, mono-, and bi-layer of graphene indicated in (b). In the case of a monolayer, the 2D peak intensity is more than twice as high as the G-peak. With increasing number of layers (here 2) the 2D peak intensity decreases and G peak intensity increases. The 2D/G ratio map shows a better comparison. The 2D peak originates from the double resonance (DR) Raman process. The number of possible DR processes increases with the number of graphene layers, for example 4 DR processes in bilayers, and hence the 2D peak widens and the intensity decreases. On the contrary the G-peak results from first order Raman scattering processes and it intensifies from mono- to bi-layer [73, 78]. The rectangle indicated in the optical image (b) was mapped with a green laser (532 nm). The spot size of the laser and the resolution of the map were both 1 μm.

The G- and 2D-peaks were integrated over the shaded region in (a), normalized and plotted for every pixel. It is important to note that the pixels towards the bottom right in (b) correspond to the substrate (Si/SiO$_2$). The histogram at the bottom of the 2D/G, 2D peak and G peak Raman maps shows the distribution of the data. The dotted lines in the histogram correspond to the range of data forming the Raman map and these lines were adjusted for better contrast of the maps while making sure that the Raman spectroscopy information is not lost. Pixels corresponding to monolayer (right) have lower G-peak intensity compared to bilayer (towards left). As explained before, the 2D peak intensity decreases and the peak broadens with increasing number of layers. This is due to the increase in the DR contributions to
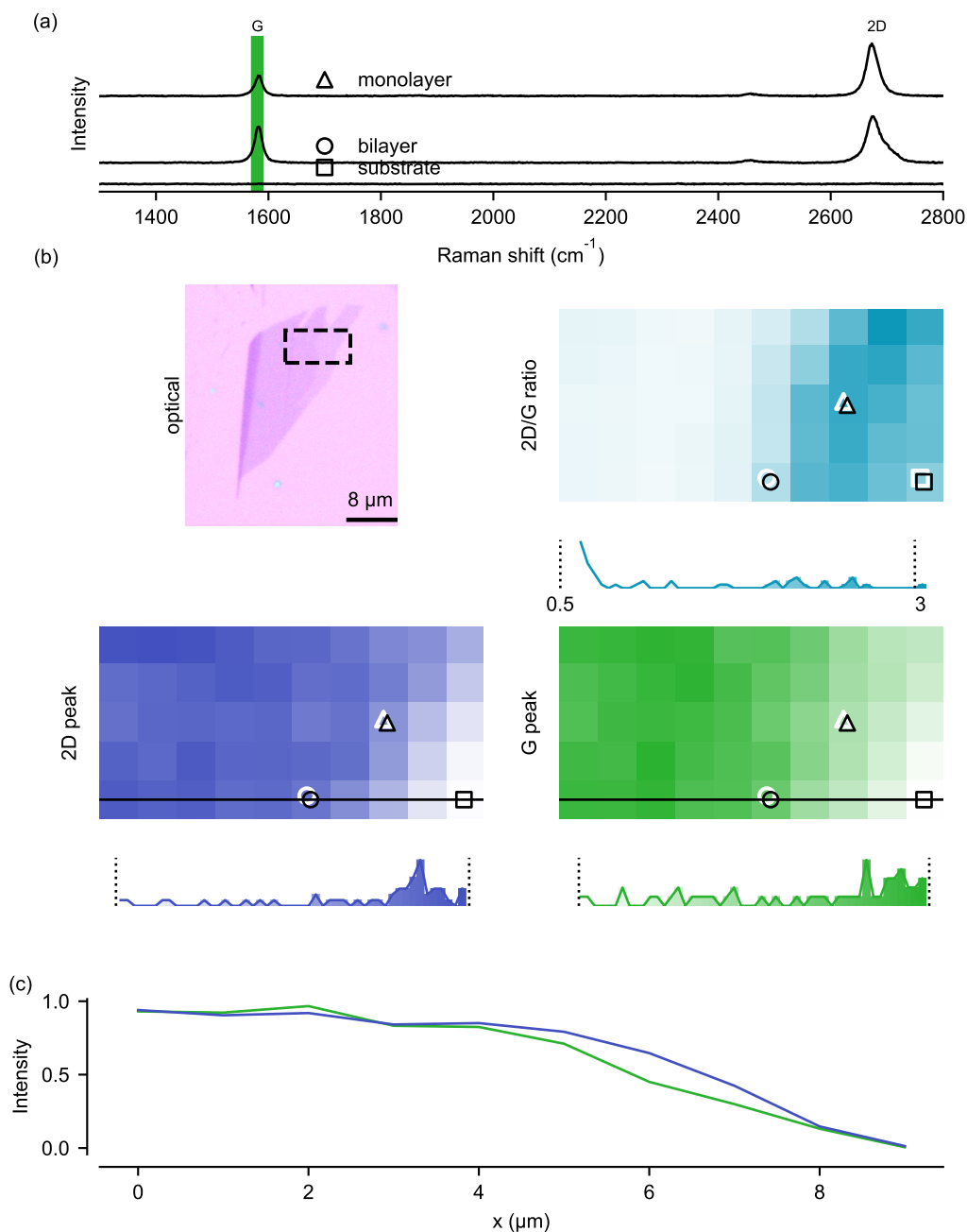
Figure 4.6 (a) Raman point spectra of the substrate, mono- and bi-layer corresponding to the pixels indicated in (b). (b) Optical image of the exfoliated graphene. The G and 2D peak intensities were integrated over the shaded regions in (a) and the normalized values (with the maximum of the Raman intensity summation as 1) plotted producing Raman maps in (b). The 2D/G ratio is obtained by dividing maximum peak intensities. (c) The G and 2D peak intensities over the lines shown in the respective Raman maps in (b).

the 2D-peak - 1 for one and 4 for two layers. The G- and 2D-peak normalized intensities are plotted (c) over the line indicated in the maps. The 2D/G ratio map is plotted by dividing the highest respective

peak values in the shaded region. The linescans in (c) are the normalized peak values. Similar data analysis was performed on all the Raman characterizations discussed in this work.

4.6.2 PEDOT:PSS and SU-8 Raman fingerprint

In the case of PEDOT:PSS, thiophene ring stretching is reflected in the Raman spectrum at $1434\,\mathrm{cm}^{-1}$ with the reported exictation wavelength as $514\,\mathrm{nm}$ [79]. The vibrational modes at $1429\,\mathrm{cm}^{-1}$ and $1509\,\mathrm{cm}^{-1}$ correspond to the symmetric and antisymmetric C=C stretching in-plane modes, respectively [80, 81].

SU-8, which is used as the insulator in this work, exhibits a Raman band at $1610\,\mathrm{cm}^{-1}$ upon annealing [82].

The Raman characterization was done with the in via Reinshaw Raman spectrometer where a $532\,\mathrm{nm}$ (green) laser was shone on the substrates with a certain duration and intensity. The rest of the parameters are included in the respective sections and figures. To obtain the Raman map, the integration of the Raman peak intensities is performed in the specified range and the normalized values are plotted for every pixel. The range is specified in the corresponding Raman maps and the normalization was done by considering the highest Raman peak summation value as 1. In some cases, the plotted range varies from 0 - 1 and is specified accordingly. This analysis was performed for bare graphene, graphene+SU-8 and graphene/PEDOT:PSS Raman characterization.

4.7 Optical transparency analysis

In the case of carbon nanostructures, the optical transmission spectra were obtained on the test substrates over the 300–1000 nm wavelength range with a binning of 0.5 nm and the measurement speed of $1000\,\mathrm{nm\,min}^{-1}$ with a Jasco V-630 UV-vis spectrometer.

In the case of graphene and graphene/PEDOT:PSS microelectrodes, the optical transparency was analysed with the set up built by Simon Dickreuter at the University of Tuebingen in Prof. Dr. Monika Fleischer's group. Optical transmission was measured at 400 nm - 700 nm. Light from a halogen lamp transmitted through the MEA was captured by a Zeiss Axio Scope A1 microscope with an EC Epiplan-Neofluar 100x/0.90 HD objective. Spectra were obtained with an Andor Shamrock SR-303i spectrometer with a slit width of 100 µm and an iDus DU416A-LDC-DD detector. This set-up achieved a spot size of 1 µm. The background dark signal of the spectrometer was subtracted from the measured spectra. Maps with 1 µm resolution were acquired by scanning the MEA with a PI P-545.xR7 piezo stage [24].

The transmittance was calculated for every pixel according to:

$$T_{400-700\,\mathrm{nm}} = \frac{\sum_{i=400}^{700} \dfrac{T_i - T_{dark}}{T_{lamp} - T_{dark}}}{n(i)}$$

where $T_{400-700\,\mathrm{nm}}$ is the relative transmittance over 400–700 nm, T_i is the value from the substrate under investigation at the certain wavelength i, the T_{dark} value is obtained by switching off the lamp, T_{lamp} value with lamp on and $n(i)$ is the number of points in the wavelength range.

4.8 Biological methods

4.9 Electrophysiology of cardiomyocytes

Electrophysiology is where complex biological systems are studied by recording the electrical activity (voltage) arising from the ion exchange through the ion-channels within the cell body. Na^+, K^+, Ca^+ ion conduction causes a potential difference between the inside and outside of the cell, which is recorded when the cell comes in the vicinity of the microelectrode. Cardiomyocytes cultured from embryonic chicken hearts, when healthy, begin showing autorhymthic contraction activity 2–3 d onwards. The ion channel exchange driven activity is recorded on cells coming either in contact or in the vicinity of the microelectrodes. The field action potential (fAP) depicted in figure 4.7 is the cellular equivalent of an electrocardiogram (ECG). The beginning of the fAP is the depolarizing component mainly driven by the

Na$^+$ ions. The fAP lasts until the repolarization which is K$^+$ driven. [83] The regularity of the fAP indicates good health of the cells, and irregularity upon test-drug introduction to the cell-culture medium shows the effect of the drug on the heart cells. In the current work, electrophysiology of cardiomyocytes was performed to check the applicability of the carbon based microelectrodes.
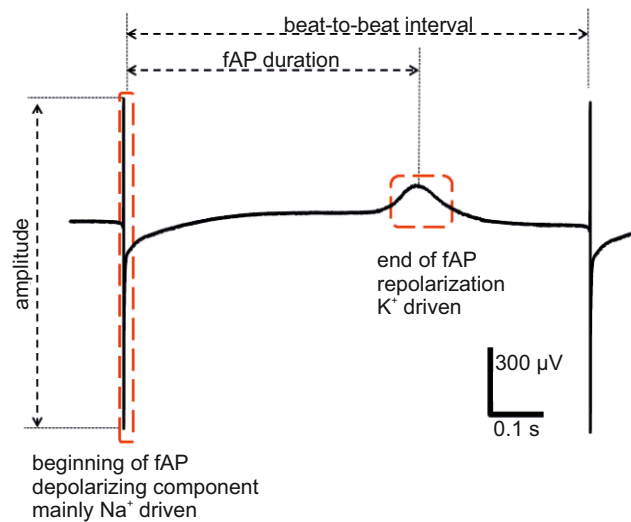
Figure 4.7 A typical action potential from *in vitro* cultured cardiomyocytes.

Upon optical investigation, recordings were performed after 5 d while maintaining the MEAs with cells at 37 °C and 5 % CO$_2$ using a MEA 2100 amplifier (Multi Channel Systems MCS GmbH, Reutlingen, Germany) with a bandpass filter of 1 Hz to 3.5 kHz and sampling at 10 kHz.

4.10 Fluorescence microscopy

Genetic modification of mice, transgenic mouse technology, has revolutionized biology and genetics by providing new genetic approaches to model many human diseases [84]. The ganglion cells in the mouse retina are labelled with green fluorescent protein (GFP). Observation of the fluorescent cells through the transparent microelectrode is one of the basic and main applications of the carbon based microelectrodes developed in this work. To test the functioning of the transparent electrodes, a part of the mouse retina was placed on the graphene microelectrode field and observed by confocal fluorescence microscope. The imaging was performed with an Axio Observer Z1 microscope (Carl Zeiss AG, Germany).

5 Development of carbon nanostructure MEA

5.1 Carbon deposition

The aim of the present work was to grow carbon nanostructures to increase the surface area of the micro-electrode to decrease the impedance which is necessary for improved cell action potential recording. The focus was on reducing the process temperature for two reasons. Firstly, the base substrate for the MEA device was a 1 mm float glass which softens at $> 600\,°C$. Secondly, the carbon material was deposited on a indium-tin-oxide (ITO) conduction path which was found to decompose into indium and tin at $550\,°C$ process temperature with atomic layer deposited Ni [68]. Here a correlative study of the carbon deposition on the atomic layer deposited (ALD) Ni with focussed ion beam (FIB) coupled with SEM, EDX and 3-dimensional tomographs from time of flight secondary-ion mass spectrometry (ToF-SIMS) was performed. The ALD-Ni layers were deposited by Daniel Hähnel at Plasma Electronic GmbH. The ToF-SIMS analysis was done by the advanced instrumentation for ion nano-analytics technology line team at the Luxembourg Institute of Science and Technology (LIST). The FIB/SEM, EDX analysis and carbon material deposition was performed at the NMI, Reutlingen. The work was performed within the framework of the C4Health project. The results are summarized later in this section.
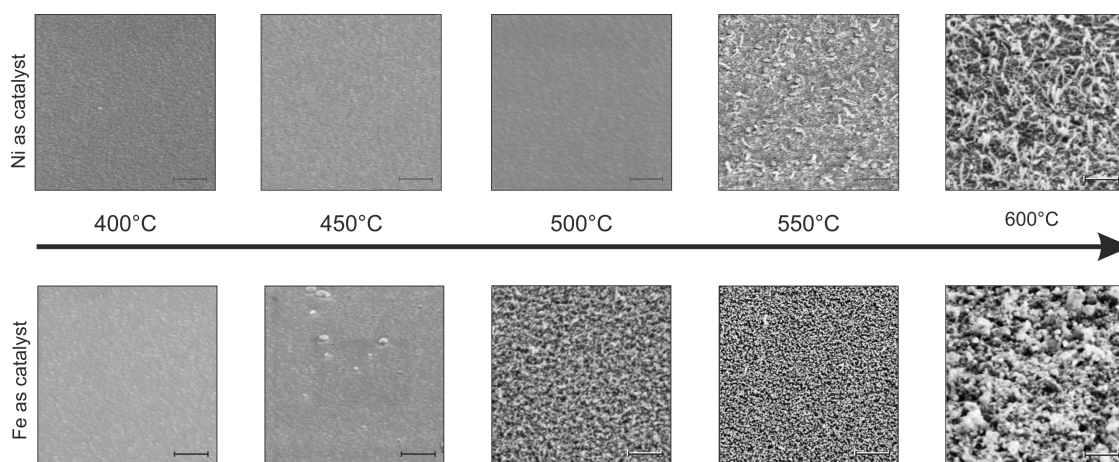
Figure 5.1 SEM images of carbon depositions with Ni and Fe as catalyst at different temperatures. The scale bar corresponds to 200 nm.

Carbon deposition on Fe and Ni as catalyst was studied for five temperatures in the range 400–600 °C with 50 °C steps. Fibrous structures appear from 550 °C and 500 °C onwards for Ni and Fe, respectively. It is important to note that the carbon depositions seen in figure 5.1 were performed on test substrates of substantially larger sputtered catalyst area compared to microelectrodes. Ni was deposited, on similar set of test substrates, following the ALD process to study the catalytic activity. The idea was to understand and compare the effect of ALD and sputtered Ni on carbon nanostructure deposition. Owing to the difficulties with handling the precursor, ALD deposition of Fe was not carried out.

ALD-Ni squares were obtained on ITO coated float-glass and carbon was deposited following the process described in section 3.1.1 (figure 5.2 (a)). The appearance of the bead-like structures after carbon deposition was unexpected and hence analysed further with EDX. Appearance of fibre like carbon structures (figure 5.2 (b)) confirmed the catalytic activity of the ALD-Ni. An EDX linescan was obtained across the bead-like structure (figure 5.3). The increase in the In, Sn signals and decrease in the O signal confirms that the bead is composed of In and Sn. The only source of In and Sn on the substrates and in the carbon deposition chamber is the ITO layer between the float-glass and ALD-Ni. Hence, it is safe to

(a)

(b)
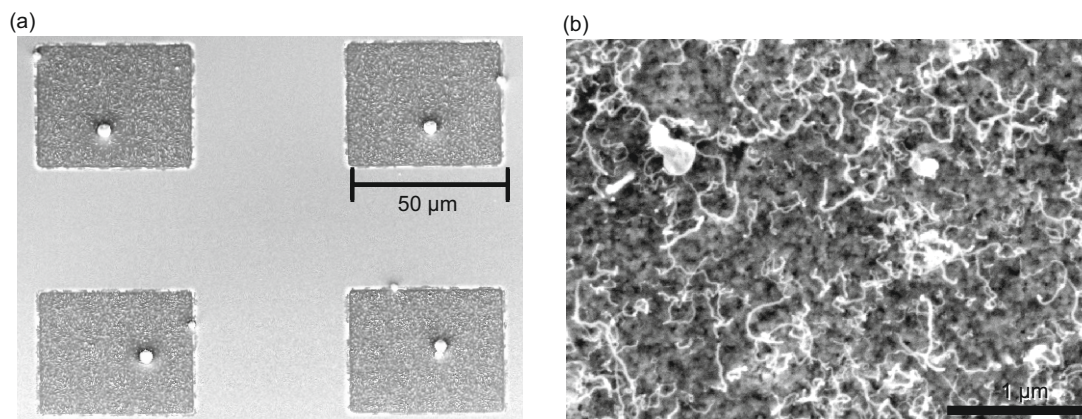
Figure 5.2 (a) SEM image of four 50 μm x 50 μm ALD Ni squares after carbon deposition. (b) Higher magnification image shows the fibre like carbon structures on one of the squares. (Ni was deposited by ALD process by and at Plasma Electronic GmbH and the carbon deposition and further characterization was done at the NMI.)

speculate that the ITO underneath the ALD-Ni, during the carbon process, decomposed into the In and Sn which migrated to the surface. FIB/SEM analysis was performed to inspect the ITO layer with and without the carbon process.

A thin layer of Pt was deposited directly before the FIB milling to avoid damaging the top layer which in this case was either Ni, ITO or carbon. ITO (bright, indicated) is distinctly visible in the FIB cross section of the substrate without carbon process (see figure 5.4 (b)). The Ni layer is not visible as the thickness ($\sim$8–10 nm) is beyond the image resolution limit. The ToF-SIMS tomographs (figure 5.4 (c)) show Ni on top of In and O signal which is consistent with the layers in the FIB cross section. The ToF-SIMS characterization depth changes from substrate to substrate and hence the Si^+ signal in (c) and (f) begins at different depths. After the carbon process, the ITO below ALD-Ni appears modified. The ToF-SIMS tomographs show that Ni percolated through the substrate and In migrated to the surface. These findings are consistent with the EDX results in figure 5.3 where the In and Sn were shown to form the bead-like structure. The ITO under Ni + CNT is visibly damaged.

Owing to the ITO decomposition, another physical vapour deposition process, sputtering, was chosen over ALD for Ni deposition. Microelectrodes were analysed with FIB/SEM upon carbon nanostructures deposition with sputter coated Ni as catalyst and the results are discussed in section 5.3. The ITO damage was minimal with sputtered Ni over the ALD Ni when the carbon deposition was carried out at 550 °C. The ALD process for Ni deposition consists of $\sim$999 cylces of hydrogen and water plasma which might result in the ITO modification and subsequent decomposition during the carbon nanostructure deposition. On the other hand, sputtering is expected to be less invasive than the ALD process and hence, the method of choice for the present wok.
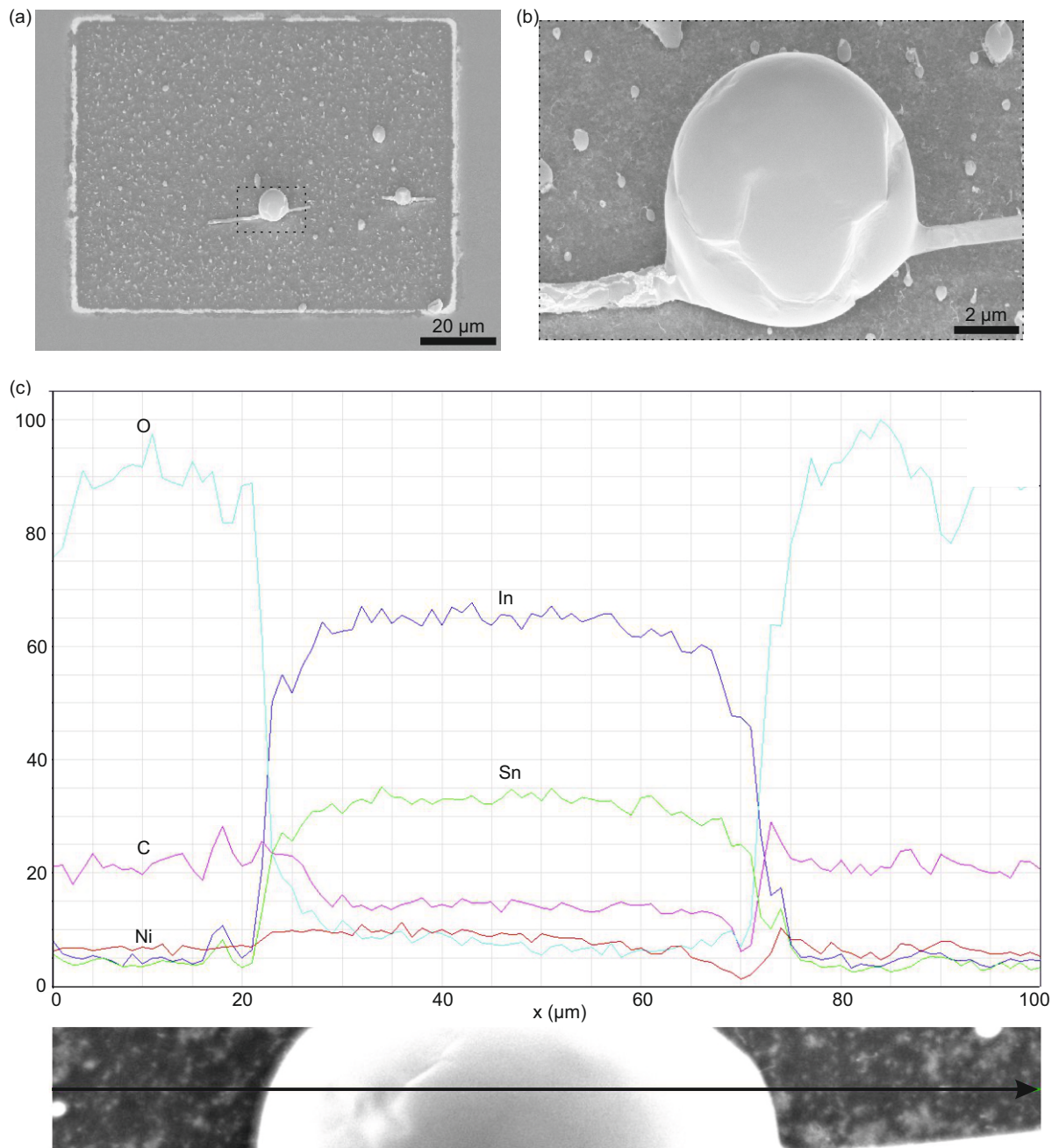
Figure 5.3 (a) SEM image of a square with Ni after carbon deposition. (b) Higher magnification image on the square showing the bead-like structure. (c) EDX linescan was obtained across the line (green) indicated in the image below the elemental signal. Ni, Sn, O, C and In signals are plotted across the line. (Ni was deposited by ALD process by and at Plasma Electronic GmbH and the carbon deposition and further characterization was done at the NMI.)
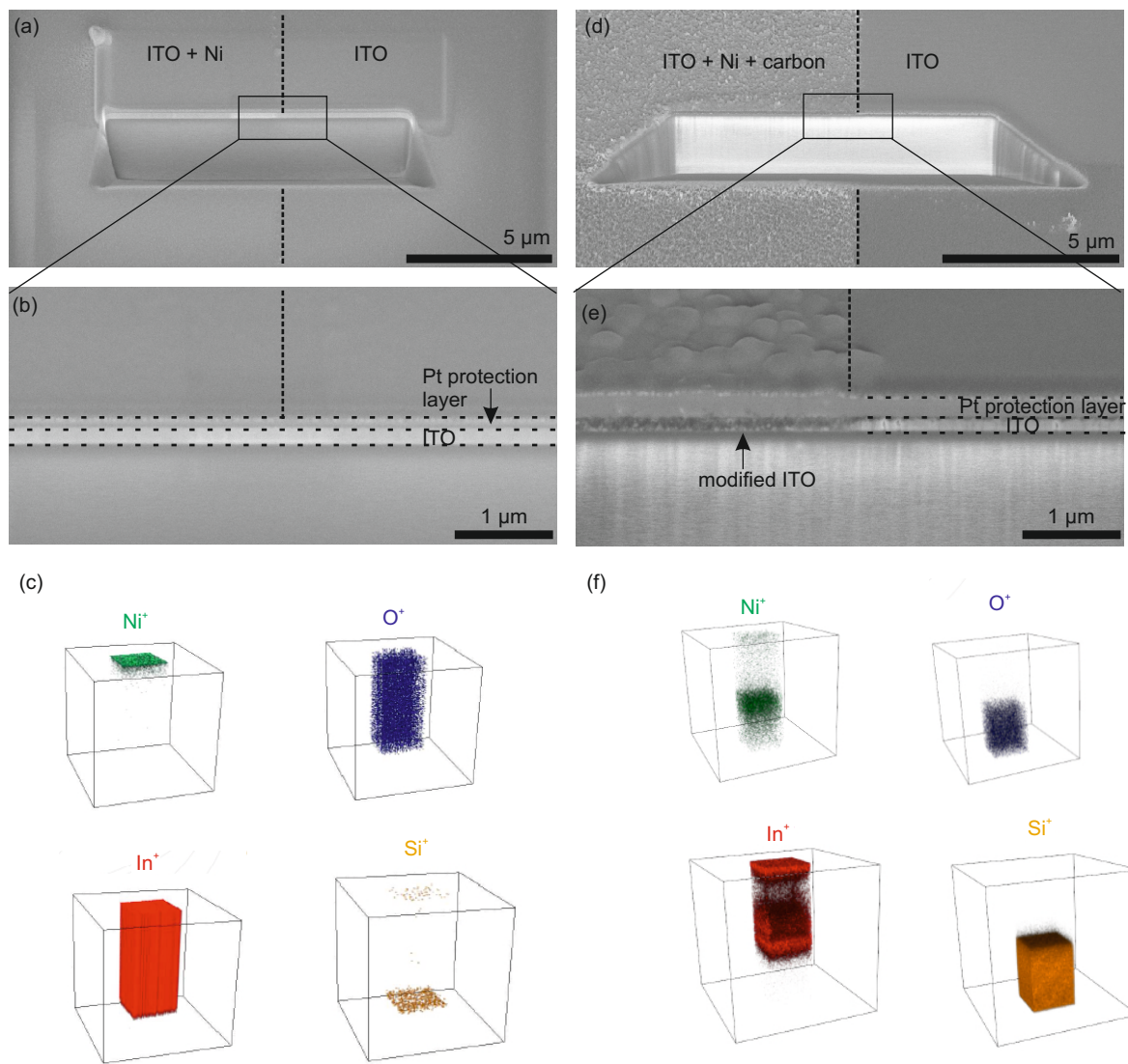
Figure 5.4 SEM image of the FIB cross section after ALD-Ni deposition before (a, b) and after (d, e) carbon deposition. FIB cross sections were done at the edge of one of the squares similar to the ones in figure 5.2. 3-dimensional ToF-SIMS tomographs of Ni^+, O^+, In^+ and Si^+. Upon carbon deposition, ITO underneath ALD-Ni (e) was decomposed in In and Sn and migrated upwards as seen in (f). The 3-dimensional ToF-SIMS tomographs in (c) and (f) were obtained by one of the four C4Health project partners - LIST.

5.2 Raman spectroscopy and optical characterization
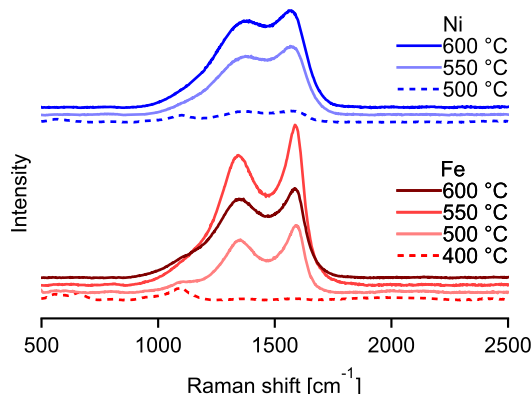
Figure 5.5 Raman spectra collected from carbon deposition on Ni and Fe as the catalyst at varying temperatures [67].

The typical Raman bands for sp^2 carbon appear around $1350\,cm^{-1}$ (D-peak) and $1580\,cm^{-1}$ (G-peak). In the case of graphene and CNTs, these two peaks are sharp. However, for amorphous carbon the peaks merge into a broad peak. The sp^3 hybridized carbon displays a peak centered around 1500–$1600\,cm^{-1}$. [72, 74, 75]

Raman spectroscopy was performed to investigate the carbon layers deposited on Ni and Fe at different processing temperatures. In the case of Ni, distinct D and G peaks appear for $550\,°C$ and $600\,°C$ which is consistent with the SEM images in figure 5.1. In the case of Fe, the Raman peaks appear from $500\,°C$ onwards which aligns with the SEM characterization. As previously mentioned, CNTs display two sharp peaks. Here, the peaks are broad which indicates that some other kind of carbon is contributing to the Raman peaks. Amorphous carbon shows broad peaks in the same region. This means that the carbon nanostructures are surrounded by amorphous carbon. It is worthwhile to note that the Raman spectra presented here are obtained from a $\sim$1 μm region on the substrate with carbon fibers of $\sim$50 nm diameter, hence they include contribution from several of the nanostructures and the surrounding amorphous carbon. The peaks are sharper for Fe compared to Ni. The broader D and G peaks in the case of Ni are due to the large amorphous carbon contribution. The focus of the present work was on the application of carbon microelectrodes and hence other characterization techniques took precedence over in-depth Raman characterization of the carbon nanostructures.
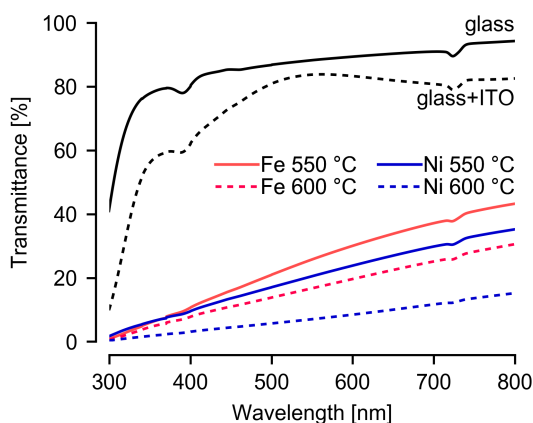
Figure 5.6 Optical transparency of glass, ITO coated glass and carbon depositions on Ni and Fe at, both, $550\,°C$ and $600\,°C$ [67].

The optical characterization was performed on the test substrates seen in figure 5.1 and figure 5.5. Based on the Raman spectroscopy results, optical transparency of carbon layers deposited on both cat-

alysts at 550 °C and 600 °C was evaluated. For a complete overview, transparency of float-glass and ITO coated glass was also checked. 1 mm float-glass shows transparency of about 90 % in the visible range. The transparency reduced to about 80 % (for $\lambda > 500$ nm) after 200 nm ITO deposition and further declined upon deposition of carbon layers. The carbon deposited on Fe displays roughly linearly increasing transparency with wavelength of up to 40 % and 20 % (at 800 nm) for process temperatures 550 °C and 600 °C, respectively. Similar trends are observed for Ni where the value drops from 30 % to 10 % when the temperature is increased from 550 °C to 600 °C.

5.3 Fabrication of carbon microelectrodes

The production of vertically aligned CNTs requires high process temperatures which are typically >600 °C. Carbon microelectrodes were fabricated following the processes detailed in section 3.2.1. Carbon structures were deposited on microelectrodes at 550 °C and 600 °C. FIB cuts were performed at the edge of the microelectrodes to investigate the ITO decomposition based on results presented in the previous section 5.1. The ITO looks almost completely destroyed after the 600 °C process (Figure 5.7 c,d) compared to the minimal morphology change upon a 550 °C process 5.7 a,b). The highest permissible process temperature was sought because carbon tends to become amorphous for lower process temperatures. Hence 550 °C was found to be the most suited process temperature for carbon deposition on the MEA devices. Carbon nanostructures at 550 °C are expected to have higher contribution of amorphous carbon compared to higher process temperatures and the optical transparency was found to be 40 %. Figure 5.8 shows a SEM image of a typical 30 µm diameter microelectrode after the carbon nanostructures deposition. The higher magnification image shows the carbon nanostructures are mostly vertically oriented.
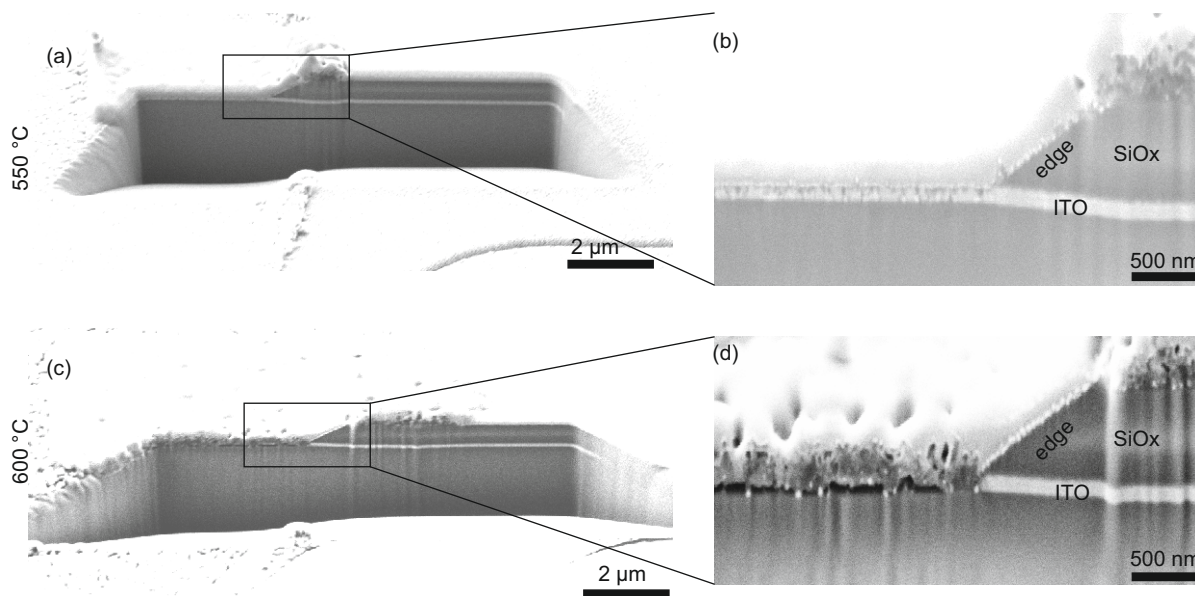
Figure 5.7 SEM images of the FIB cuts for carbon deposition processes at 550 °C (a,b) and 600 °C (c,d). The ITO (bright) is completely damaged for 600 °C compared to 550 °C.
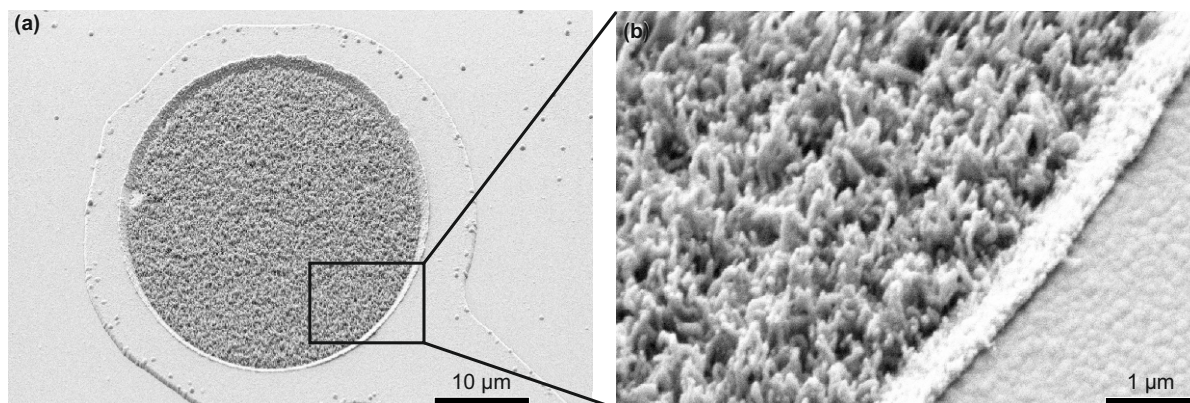
Figure 5.8 (a) SEM image of a 30 µm diameter microelectrode after the uniform carbon deposition. (b) Higher magnification SEM image of the region indicated in (a). Here the edge of the microelectrode is seen with mostly fibrous carbon structures.

5.4 Electrochemical characterization
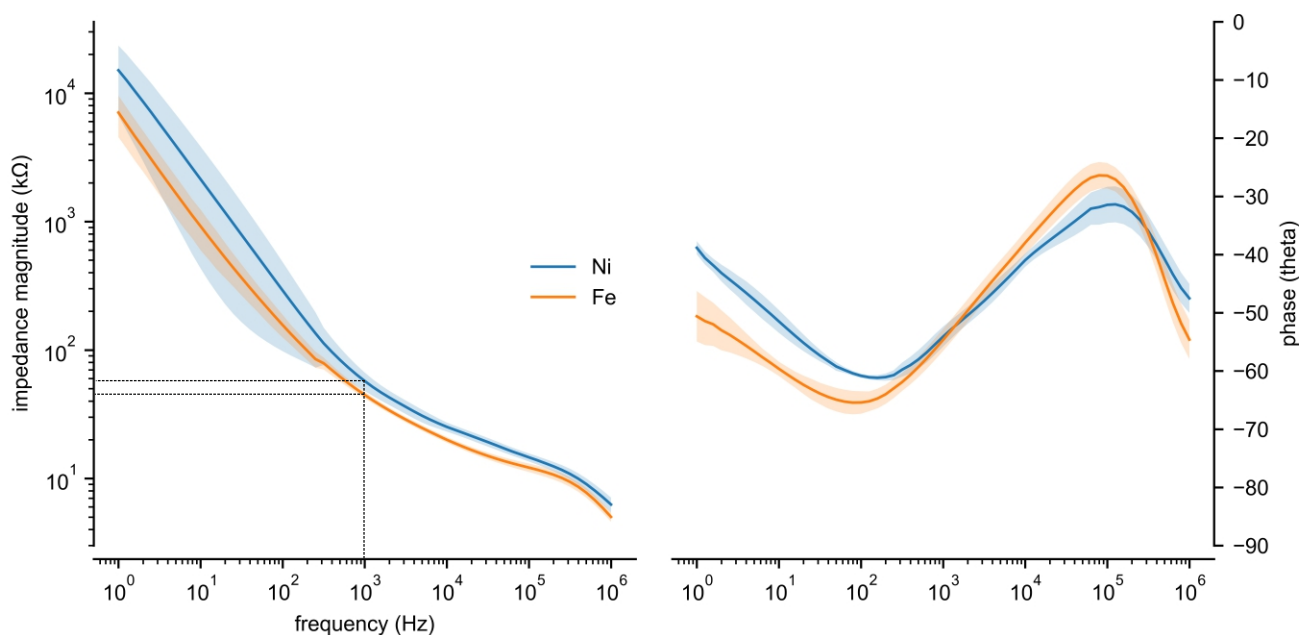
Figure 5.9 Magnitude impedance and phase of the semitransparent carbon microelectrodes with Ni and Fe as catalyst.

Traditionally the magnitude impedance at 1 kHz is considered as the benchmark when investigating a potential new material as microelectrode. The aim was to produce semitransparent microelectrodes with <100 kΩ. The impedances were well below the target value ((45 ± 3) kΩ for Ni-carbon and (57 ± 9) kΩ for Fe-carbon, see figure 5.9) and within the range of commercially available MEAs [23]. The electrochemical impedance spectroscopy is usually performed with 10 mV amplitude. The impedance decreases with the measurement amplitude. The impedance measurements reported here were performed at 1 V which underestimates the electrode impedance. However, the suitability of these microelectrodes was studied with the electrophysiological recordings. The phase appears to have more features than expected. This might be the result of the 100 times higher measurement amplitude. When

going from high to low frequencies, the phase becomes resistive-capacitive-resistive again. Typically the phase should be resistive for higher and capacitive for lower frequencies as the capacitive (imaginary impedance) contribution dominates at low frequencies. Compared to the high imaginary contribution, the real impedance is low for most of the frequencies in the range 1–3500 Hz and hence, lower thermal noise during electrophysiology.

5.5 Application of carbon nanostructure MEA and cardiomyocyte-carbon interface ultrastructure
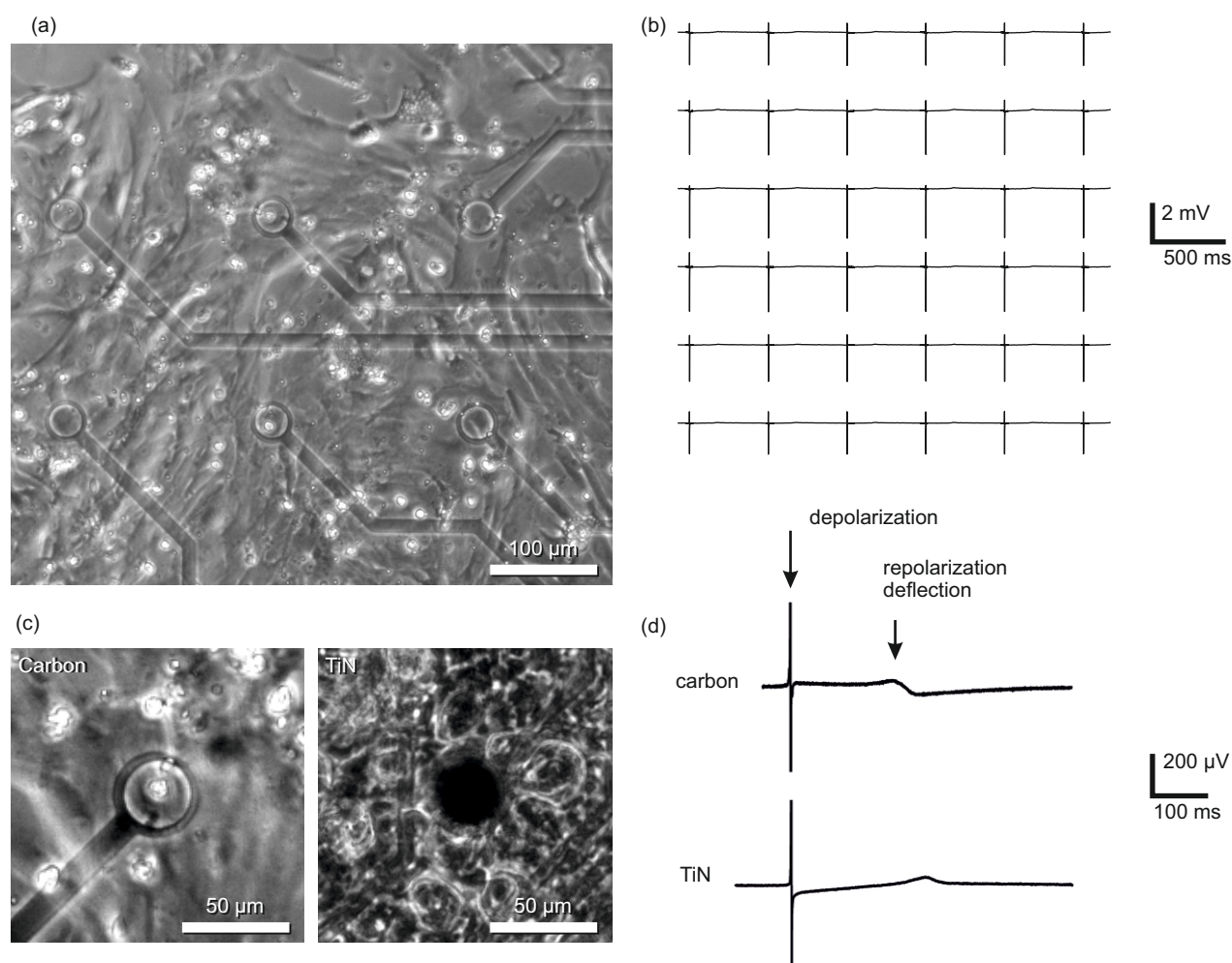
Figure 5.10 Application of semitransparent carbon MEA. (a) Transmission mode optical microscopic image of the cultured chicken heart cells through the semitransparent carbon microelectrodes with transparent ITO conduction paths. (b) Field action potentials (fAP) of cardiomyocytes recorded in parallel from six carbon microelectrodes. Six depolarization deflections at the beginning of the fAPs recorded from six microelectrodes over 3 s with peak-to-peak 3 mV amplitude and 20 µV noise. (c) Magnified semitransparent carbon and opaque TiN microelectrodes where the cells are visible through the former in contrast to the latter. (d) Comparative averaged fAPs (26 sweeps) measured with carbon and standard TiN MEA. Here the amplitude is cut-off for better visualization of the repolarization voltage deflection. [67]

Embryonic chicken heart cells were cultivated for up to 5 d *in vitro*. The autorhythmic contraction was visible after 2–3 d. The visualization of the cardiomyocytes through the carbon microelectrodes on, both,
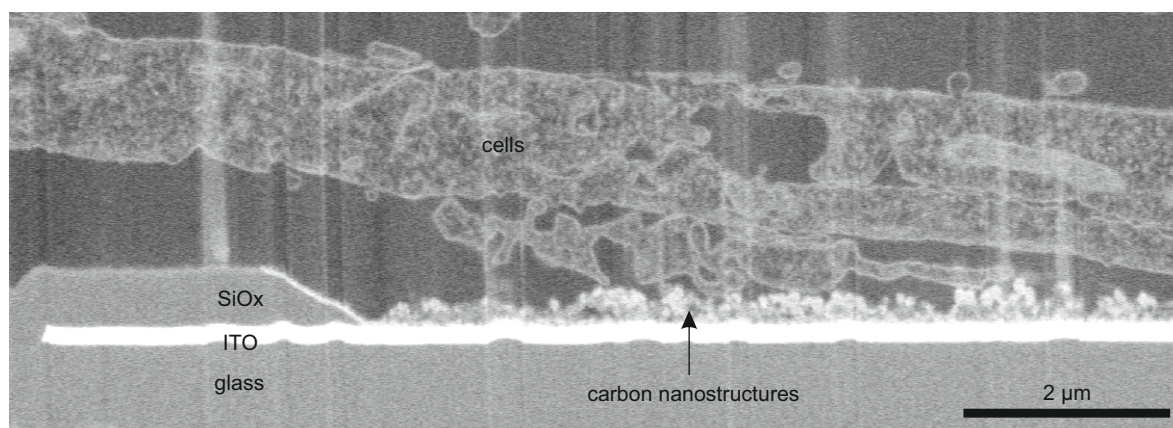
Figure 5.11 SEM image of the FIB cross section of cardiomyocyte-carbon interface at the edge of an electrode. The layered system of the carbon MEA and the close proximity of the cells indicates the biological acceptance of the carbon nanostructures. [67]

Fe and Ni was possible owing to their optical semi-transparency. An example is seen in figure 5.10 (a) where the heart cells on the ITO conduction paths leading to semitransparent microelectrodes are captured in the transmission mode. This is an improvement over the opaque TiN microelectrode where the optical inspection is not possible (figure 5.10 (c)). Each carbon MEA is comprised of 54 microelectrodes and the signals were recorded from all of them simultaneously. Figure 5.10 (b) shows six of the representative recordings where the synchronized depolarization deflection is visible. In addition to the optical visualization, electrophysiological recordings were obtained at day 5 *in vitro* with peak-to-peak signal amplitudes of up to 3 mV and less than 20 µV noise, which is comparable to the standard opaque TiN electrodes. These results confirm the good adhesion and viability of the cells on the carbon deposited on both the catalysts. The depolarizing, Na^+ channel-mediated, peak-to-peak amplitude up to 3 mV and a visible K^+ channel-mediated repolarization after 200 ms are comparable to the signals measured with a TiN MEA (figure 5.10 (d)). The carbon MEA could be reused after overnight immersion in a Tegazyame solution prepared according to the manufacturer's instructions (Alconox, Inc.).

The FIB milling of the cardiomyocytes stained and fixed on a carbon microelectrode revealed the layered system (figure 5.11). The 200 nm ITO conduction path with 500 nm SiO_x insulator and a rough 200–300 nm layer of carbon nanostructures on the ITO are visible. The ITO decomposition seen in figures 5.4 and 5.7 is not observed here. The carbon nanostructures survived cell culture, electrophysiology and fixation indicating the stability of the ITO-carbon and support the use of this combination in biological applications.

5.6 Chapter Summary

This chapter discussed the development of carbon nanostructure electrode MEAs. Carbon nanostructures were also deposited on ALD Ni (by C4Health project partners - Plasma Electronic GmbH) in which case the ITO underneath was found to be destroyed after the 550 °C process. The ITO modification was further analysed with ToF-SIMS (performed by and at C4Health project partners - LIST) where the In and Sn was found to migrate to the surface and the ALD-Ni to percolate through the ITO layer. The modified Sn and In upon migrating to the surface formed bead-like structures and the composition was confirmed further by EDX.

To avoid ITO base degradation and softening of the float-glass substrate, the carbon deposition process was optimised by studying the deposition at 5 different temperatures in the range 400–600 °C in 50 °C steps. The carbon deposition was visualized with SEM where the nanostructures appeared from 550 °C and 500 °C onwards for Ni and Fe, respectively. Catalytic activity of Ni and Fe was studied for all the temperatures followed by detailed Raman spectroscopy and optical transparency characterization. The characteristic carbon peaks appeared on both the catalysts and were consistent with the SEM char-

acterization. The transparency being the aim of this work, the optical characterization was performed where the 550 °C and 600 °C were found to display transparencies varying from ∼10 % near ∼400 nm to ∼40 % near ∼800 nm.

Based on the results obtained on the test substrates, carbon was deposited on electrodes opened in the MEA substrate with ITO as conduction path. FIB milling in combination with SEM revealed the modification of ITO underneath the carbon deposition for the 600 °C. On the other hand, for lower temperature of 550 °C, the ITO was intact after the carbon nanostructure deposition. The main purpose of ITO underneath was to provide electrical contact between the carbon microelectrode and the rest of the conduction path leading to the opened contact pad at the edge of the MEA device and hence slight ITO modification was acceptable. Carbon was deposited with Ni and Fe as catalysts on MEA substrates at 550 °C and showed acceptable electrical impedance. The impedance at 1 kHz was lower than the target value 100 kΩ when measured with 1 V amplitude.

$$v_t = \sqrt{4k_B T(52.5\,\text{k}\Omega * 3499\,\text{Hz})} = 1.7\,\text{µV for Fe - carbon}$$
$$v_t = \sqrt{4k_B T(31.8\,\text{k}\Omega * 3499\,\text{Hz})} = 1.3\,\text{µV for Ni-carbon}$$

The averaged real impedance integrated over the measured bandwidth was 52.5 kΩ for Fe and 31.8 kΩ for Ni which translates to 1.7 µV and 1.3 µV thermal noise, respectively. Electrophysiology was performed by culturing embryonic chicken heart cells on Fe-carbon (40 % transparent) and Ni-carbon (30 % transparent) microelectrodes. Depolarization deflections with 3 mV peak-to-peak amplitude with 20 µV noise were recorded. The cardiomyocyte-electrode ultrastructure was visualized by staining, and fixing the cells atop carbon microelectrodes followed by FIB milling at the edge of the electrode. The SEM revealed the carbon nanostructures on the unmodified ITO with cells on top. The close proximity of the cells indicated the biological acceptance of the carbon nanostructures.

6 Development of graphene MEA

6.1 Graphene Growth

CVD growth of graphene is extensively researched as this process is scalable for industries. Transition metals like Cu, Pt, Ni or Co are annealed at >500 °C where the surface rearranges and the defects, such as impurities and holes, are reduced. Following the annealing step, a carbon source (e.g. methane) is introduced in the process chamber. The combination of high temperature and catalyst reduces the carbon source producing carbon which deposits on the catalyst surface. The carbon is deposited/dissolved on/in the metal forming a hexagonal carbon lattice, graphene. Several theories have been proposed about the graphene growth mechanism on the transition metal surfaces. Cu is reported to outperform other catalysts in terms of cost-effective graphene growth. However, wrinkles and structural defects in graphene are some of the drawbacks of using Cu as the CVD process catalyst [85].

The growth mechanisms depend on the catalyst in use [86, 87]. The dissolution of carbon in the transition metal and catalytic reduction of the carbon precursor at the metal surface are the two main growth mechanisms. Cu and Ni are popularly used transition metals because of their favorable catalytic properties and low cost. In the case of Ni, graphene growth is solubility driven owing to the relatively high solubility of carbon in Ni compared to Cu [88]. Carbon dissolves in Ni at the process temperature and segregates upon cooling down. In the case of Cu, the catalytic activity dominates due to low solubility of carbon in Cu. The mechanisms of growth on Cu and Ni were studied by carbon isotope labelling [89]. Here it was shown that more carbon atoms dissolving in Ni pose difficulty in controlling the density of nucleation sites and, in turn, the number of graphene layers. In the case of Cu, the carbon comes from the decomposed methane. The thermodynamic interaction between graphene and the two lattice planes of Cu, Cu(111) Cu(100), is understood by employing density functional theory calculations [90]. Here the atomic carbon was found to be energetically unstable on the surface of Cu and hence the graphene growth is concluded to be nucleation driven. The difference in growth on oxygen free and deficient copper foils was studied in [69]. Also, the pre-treatment of copper prior to annealing and growth was optimised. In the current work, oxygen rich copper foil with the optimised Cu pre-treatment was used.

In the ideal case, single crystalline Cu would serve as a catalyst upon which a nucleation site can be introduced for utmost control over the dimension and the number of graphene layers. In reality, Cu is polycrystalline. The nucleation of graphene initiates at defect sites like holes or grain boundaries. Large grain sizes ensure a lower number of grain boundaries and hence better control of uniform graphene layers. Annealing, wherein metal is subjected to high temperatures to relieve internal stress and in turn increase grain size, is popularly used as part of the Cu pre-treatment prior to graphene growth. The main objective of Cu annealing is to increase the grain size in order to decrease the number of grain boundaries, which in turn reduces the possible number of nucleation sites.

The Cu grain size increased with increasing annealing temperature (at 600 °C to 800 °C in Figure 6.1 (a)). The difference in the contrast among the grains in the SEM images results from the orientation of Cu. At higher magnification, an evident difference in the number of nucleation sites between the two temperatures is observed. In the case of 600 °C nucleation sites are substantially abundant compared to 800 °C. In the case of 800 °C, a junction of three grain boundaries and the deformed hexagonal dark regions of the second graphene layer in addition to the uniform monolayer are visible in figure 6.1. The graphene appears deformed as it follows the copper surface which is soft at 800 °C and becomes wavy upon cool down to room temperature. The bright spots (indicated), similar to the ones seen here, were analysed with energy dispersive X-ray spectroscopy (EDX).

The nanoparticles appearing on Cu after the CVD process have been investigated by several groups. The CVD chambers, which are made of quartz glass, are subjected to several cycles of high temperature processes. Reaction of the quartz chamber with hot hydrogen, contamination within the Cu bulk and Cu emissions hitting the quartz tube are some of the proposed origins of these particles [91]. Figure 6.2 (a)
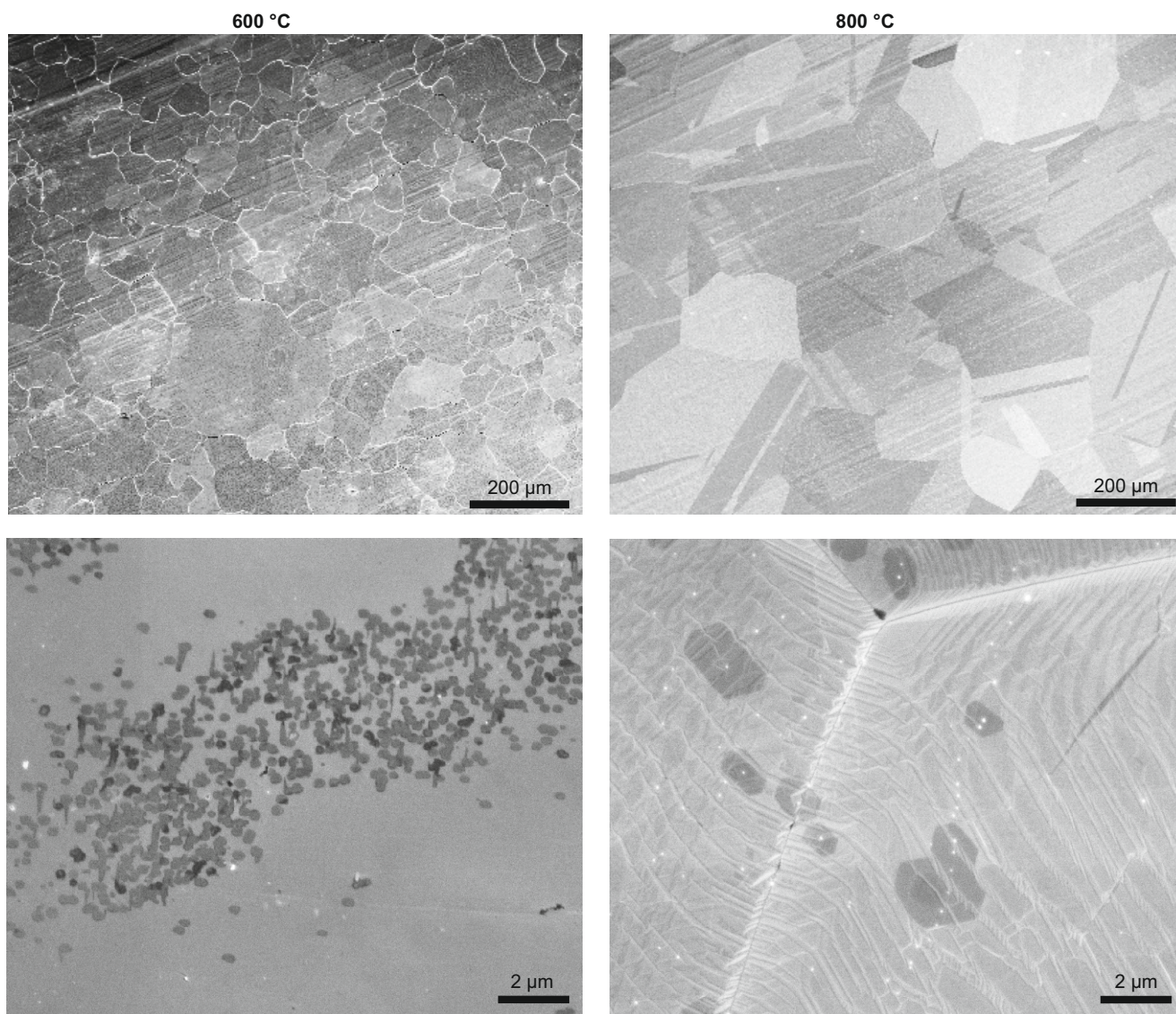
Figure 6.1 SEM images of graphene grown on Cu at 600 °C and 800 °C. Graphene grown at 600 °C has smaller grains than at 800 °C. The number of nucleation sites (darker regions) decreases with increasing process temperature.

shows a SEM image of graphene on copper with several bilayers (dark spots). One of the bright spots (indicated) was analysed with an EDX line scan. (b) Shows the line scan for oxygen, carbon, Cu and silicon. The Cu signal drops on the particle and the oxygen and silicon signals shoot up on the particle confirming the composition of the contaminant as SiO_x. The Cu foils used in this work are commercially available where the source claims 99.9 % purity. Hence, it is safe to assume that these contaminants arise from the quartz processing chamber. For the purpose of this work, the current amount of contaminants is acceptable.
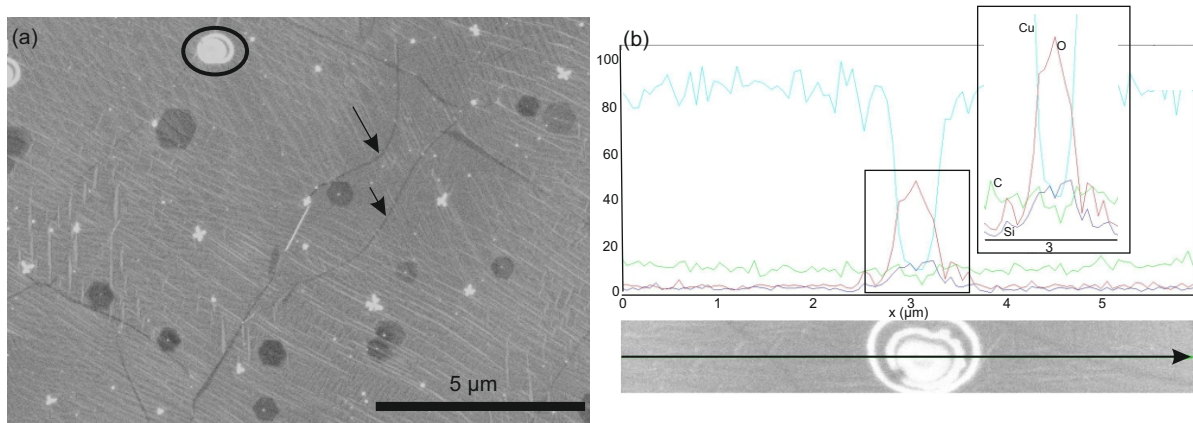
Figure 6.2 (a) SEM image of graphene on Cu. The dark lines (indicated by the arrows) are the graphene grain boundaries and the hexagonal dark spots are the second / third graphene layers. The bright structure (circled) was analysed with EDX. (b) Oxygen, carbon, silicon and Cu elemental scan over the green line indicated on the SEM image.

6.2 Fabrication of graphene MEA

Graphene MEAs were fabricated following the steps mentioned in 3.2.2 and the SEM analysis was performed after different processing steps (Figure 6.3). The CVD grown graphene on Cu (a) is transferred onto the Au conduction paths (b) using a polymer-based transfer technique. The dark hexagons are second and third (darker) layers of graphene. The graphene here is polycrystalline with the dark lines being the grain boundaries. It is important to note that graphene is also on the Au conduction paths (bright). The transferred graphene was structured into 40 µm diameter graphene microelectrodes (dark discs in Figure (c)) followed by the application of an insulator (SU-8) (d). At stage (c), the electrodes are 10 µm larger than the final microelectrodes to compensate for the possible misalignment in the photolithography process. The SU-8 was opened by photolithography yielding microelectrodes of 30 µm diameter. (e) shows an overview of the MEA with a glued cell-culture chamber. At this stage the graphene MEA is ready for electrophysiology.
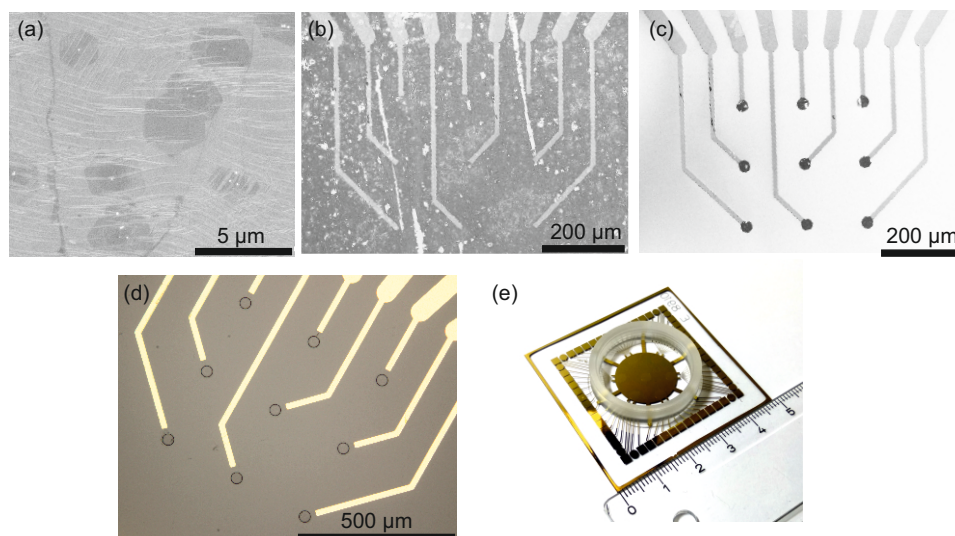
Figure 6.3 (a) SEM image of polycrystalline graphene grown on Cu. (b) Graphene transferred from Cu to Au conduction paths following a polymer-based transfer method. (c) Graphene structured by photolithography. The dark discs are 40 μm diameter graphene microelectrodes. (d) Optical image of a finished graphene-MEA with Au conduction paths leading to the transparent graphene electrodes of 30 μm diameter. The image was acquired after the SU-8 deposition. (e) A graphene 6-well MEA with cell culture chamber.

6.3 Raman characterization

The signature graphene peaks, G and 2D, appear around $1580\,cm^{-1}$ and $2700\,cm^{-1}$, respectively. Fig 6.4 shows correlative SEM and Raman spectroscopy of a graphene conduction path and microelectrode. Here, the graphene conduction path (65 μm in length) and microelectrode (40 μm diameter) are imaged with SEM. The microelectrode diameter is larger to compensate for the possible misalignment in the SU-8 photolighography. CVD graphene is polycrystalline, and the grain boundaries can be seen in the SEM image. The number of graphene layers can be estimated based on the contrast in the SEM image. The dark spots on the rather uniform monolayer (grey) graphene are the second or third hexagonal carbon layer. It should be noted that this quantification is only contrast based and hence only indicative. The exact number of layers should always be confirmed with Raman spectroscopy. Part of the Au conduction path (bright) overlapped with the graphene is visible (indicated) on the left side of the SEM image. From the electrical contact point of view, damaged graphene is acceptable as long as some overlap exists between graphene and Au which ensures charge flow.

Raman spectra were obtained over a 100 μm x 40 μm area with 300 nm pixel spacing. The G (red) and 2D (green) peak intensities were integrated and plotted for each point resulting in the Raman maps (figure 6.4 (b)). The 2D/G ratio map shows the data plotted in the range between 1 and 2.5. As previously mentioned, a ratio of 2 and higher means the graphene is single layer. Based on this one can conclude that most of the graphene seen here is monolayer with patches of bi and/or multilayer. The defects seen in the SEM image are reflected in the G and 2D maps. Graphene on Au has lower signal intensity compared to graphene on glass. The Raman activity is substrate governed, with conducting substrates exhibiting stronger interaction with graphene compared to insulating substrates. The electron transfer between SiC, Ni, Co and graphene dampens the Raman signal. In the case of Au and Ag, lattice strain is more dominating than the electron transfer effect [76, 92].

Raman spectroscopy was performed upon SU-8 application to inspect possible contamination of graphene microelectrodes. SU-8 annealed at 200 °C exhibits a Raman band at $\sim 1610\,cm^{-1}$ [82]. Figure 6.5 shows a SEM image of an electrode and conduction path made of graphene before applying the SU-8 insulator. A Raman map was obtained after the SU-8 application over the indicated rectangle with 1 μm spacing. The graphene, SU-8 and graphene covered with SU-8 point spectra are offset and shown in (a) corresponding to the indicated pixels in the Raman map. In the case of graphene + SU-8
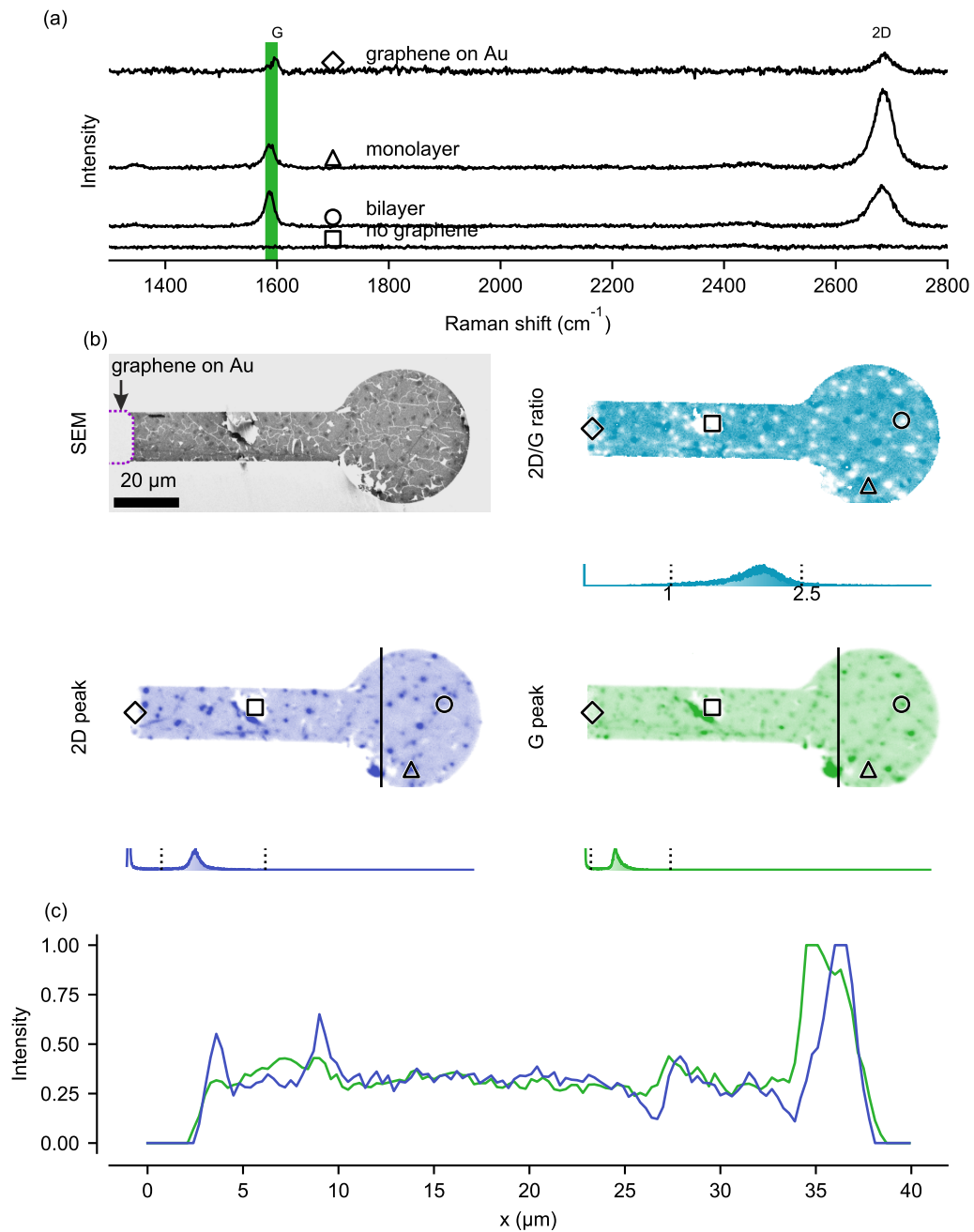
Figure 6.4 (a) Raman point spectra obtained from the glass substrate, graphene mono- and bi-layers from the regions indicated in the Raman map (b). (b) SEM image, obtained after the graphene structuring, shows the end of the graphene covered Au (bright) and graphene only conduction path (dark). The electrode at this point is $\sim$40 μm diameter to compensate for the possible misalignment in the SU-8 lithography step. The graphene peaks, G and 2D, were integrated over the shaded region indicated in (a) and the normalized values plotted as the Raman map. The 2D/G ratio map was obtained from the highest peak intensities for both 2D and G. (c) The graphene peak intensities over the line indicated in the maps.

the graphene peaks appear and, in addition, the epoxy groups in SU-8 lead to a peak at $1610 \, \text{cm}^{-1}$. The lower intensity of the 2D in the case of graphene + SU-8 compared to pure graphene can be explained in two ways. Either 5 µm thick SU-8 dampens the signal or the contribution of SU-8 is substantially larger than graphene. The intensified left shoulder of the SU-8 peak includes the graphene (G-peak) contribution. The superposition of the 2D and SU-8 peak provides detailed analysis of the finished graphene microelectrode. The 2D peak was selected instead of G because the intensity of the latter might include contribution from the SU-8 peak. In conclusion, Raman spectroscopy showed no SU-8 contamination of the graphene microelectrodes.
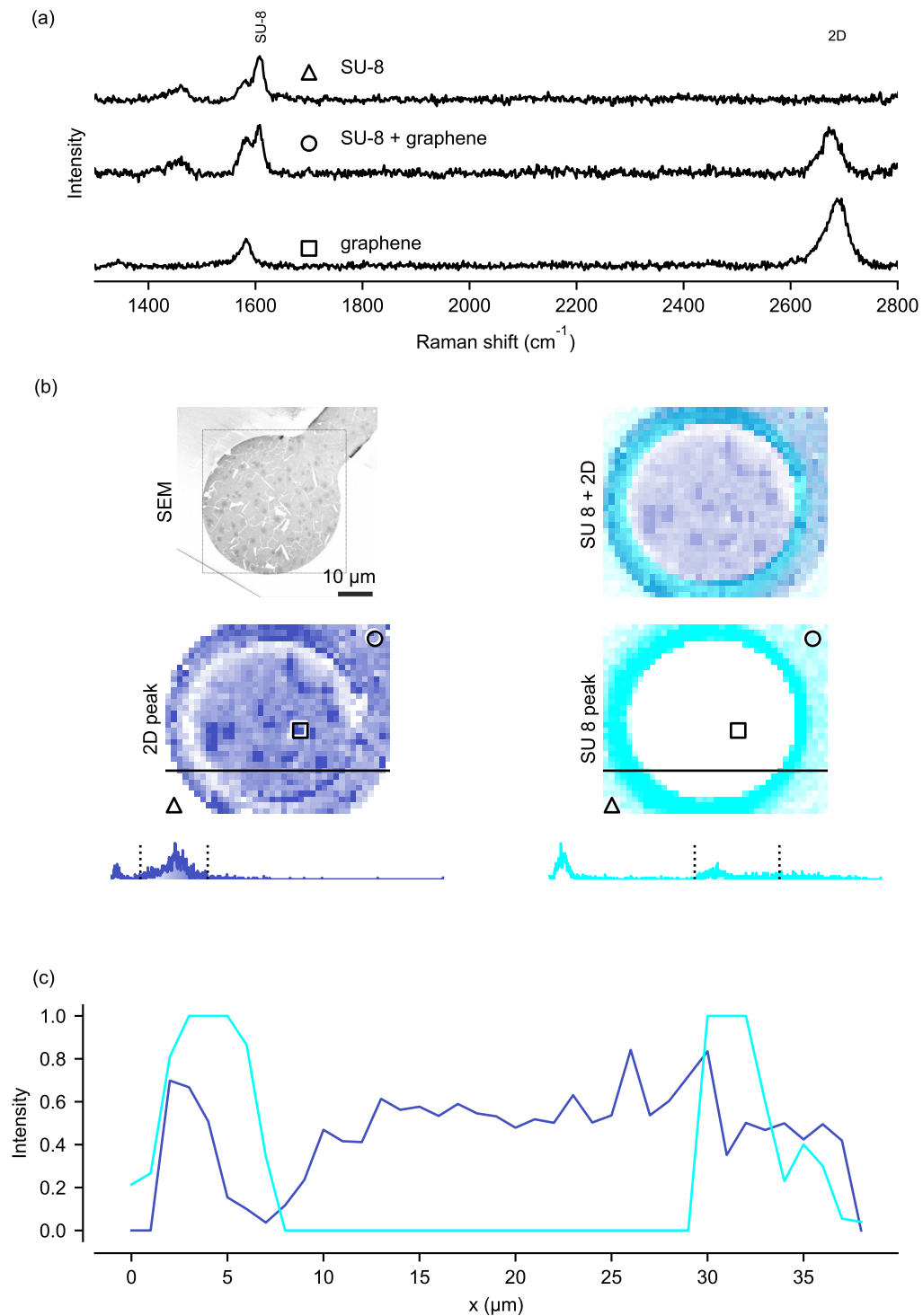
Figure 6.5 (a) Raman point spectra for SU-8, graphene and SU8+graphene. (b) SEM image and Raman maps of the indicated graphene microelectrode obtained with 532 nm laser at 7.6 mW, 1 s exposure and 1 μm resolution. The SU-8 and graphene (2D) peaks were integrated over the shaded region indicated in (a) and normalized. (c) Peak intensities over the indicated line (across the electrode).

6.4 Electrical characterization
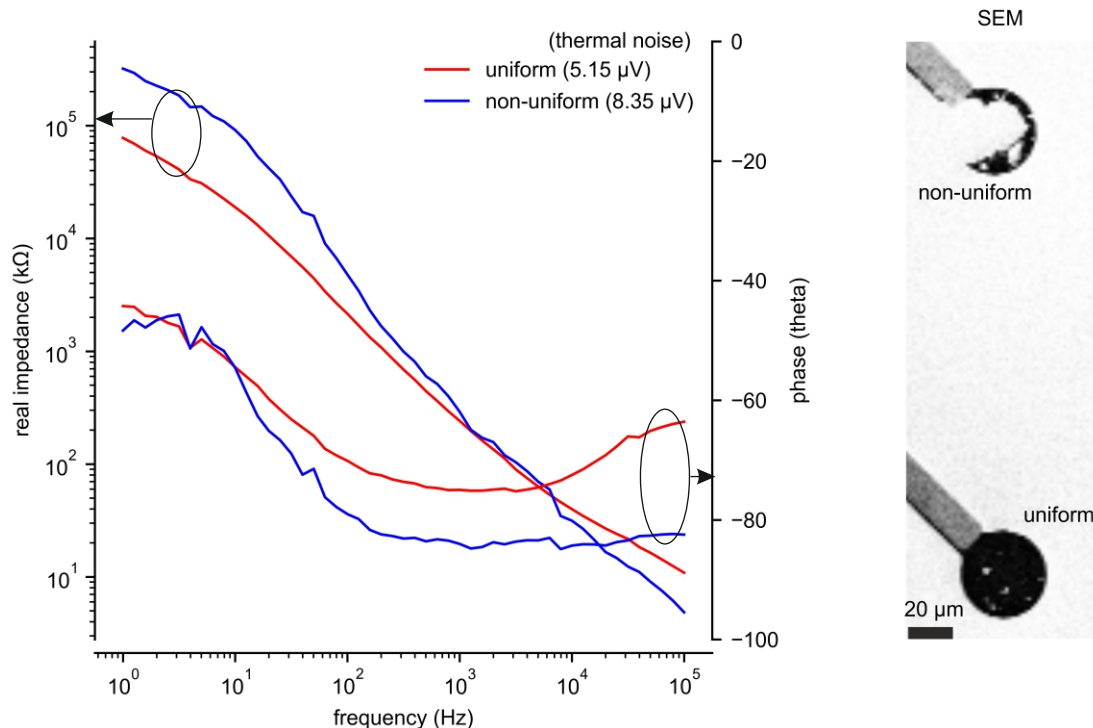
Figure 6.6 Impedance and phase curves over the 1 Hz-100 kHz frequency range for uniform (bottom) and non-uniform (top) CVD graphene microelectrode.
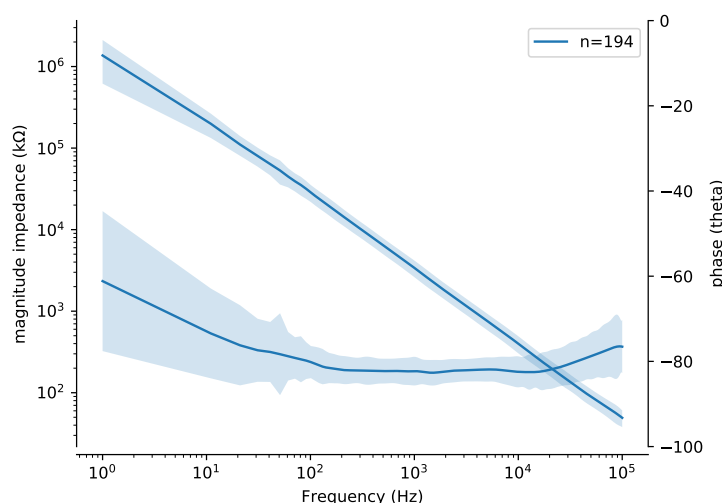
Figure 6.7 Impedance magnitude and phase curves over the 1 Hz-100 kHz frequency range averaged over 194 transparent graphene microelectrodes of 30 μm diameter. The non-uniform graphene coverage explains the large standard deviation.

Graphene microelectrodes are reported to display specific impedances (multiplication of impedance magnitude at 1 kHz and electrode area) 31–150 Ω cm^2 [19, 20, 58, 62] which translate to 4.4–2.1 MΩ impedance at 1 kHz for microelectrodes of 30 μm diameter. The presence of 1 % defects in highly ori-

ented pyrolytic graphene is estimated to result in a 10^3 factor increase in the heterogenous electron transfer rate constant [93, 94]. The effect of defects on the charge transfer is more pronounced in the case of graphite and minimal in the case of mono or bilayer graphene [95]. In the case of microelectrodes, the magnitude impedance of $<100\,\text{k}\Omega$ at $1\,\text{kHz}$ is usually used as the proxy and as mentioned in section 4.5.2, the integration of real impedance over the measured bandwidth provides estimations of the thermal noise following the Johnson Nyquist equation. The uniform and non-uniform graphene microelectrodes showed similar real impedance curves with the non-uniform electrode displaying a slightly steeper slope (see figure 6.6). The phase for both, on the other hand, was largely capacitive in the high frequency range and becomes Warburg dominant for the lower frequencies. The non-uniform graphene, as seen from the values in figure 6.6, displays 1.6 fold higher RMS noise than the uniform graphene.

Figure 6.7 shows the averaged impedance and phase curves for 194 graphene microelectrodes. The average impedance magnitude at $1\,\text{kHz}$ was found to be $(2.9 \pm 0.3)\,\text{M}\Omega$. Graphene displays poor impedance values which is expected to be reflected in the signal-to-noise ratio of the electrophysiological recordings. High impedance values mean high real impedance in the recording bandwidth (1–$3500\,\text{Hz}$) which leads to higher thermal noise of graphene. The high thermal noise shadows the electrogenic signals from the cells which is undesirable. Another disadvantage of high impedance, especially in the lower frequencies is, the cellular signals not picked up leading to information loss. The low signal-to-noise ratio mainly comes from higher noise levels. The low signal-to-noise ratio can be acceptable for basic cellular recordings but poses hurdles when the cellular activity is in the smaller frequency ranges. The standard deviation increased for lower frequencies. For lower frequencies, the impedance reached values close to the sensitivity of the measuring device hence the large deviations. The defective graphene showed higher impedance values which increases the standard deviation of the curves.

6.5 Optical characterization

Optical transparency of exfoliated graphene reportedly decreases with increasing number of layers with that of mono- and bi-layers being (in air) 98 % and 94 %, respectively. [43] The 1 mm glass substrate is reported to be 90 % transparent and hence limits the optical properties of the CVD grown graphene mono- and bi-layers. The CVD graphene, as mentioned before, is wrinkled and might carry PMMA residues from the transfer process. Hence for thorough optical analysis, transmittance maps were obtained over the 30 μm microelectrode and SU-8 covered glass region (figure 6.8). The bright-dark-bright outline of the microelectrode results from the scattering of light at the edge between the graphene and the 5 μm higher SU-8. The photolithography of SU-8 results in a sharp edge between the electrode and the rest of the substrate. The scattering can be better visualized in the linescans across the microelectrode (red) where the normalized transmittance value goes above 1. Graphene and SU-8 on glass show almost consistent 90 % transparency in the visible range. The transmittance was found to reduce by $\sim$3 % when the average data over the glass+SU-8 (upper line on the map) is deducted from the linescan over the graphene electrode (middle). The uniform transparency over the visible range allows for the flexibility in the application.

(a)

optical image

(b)

transmittance map

25 µm

(c)
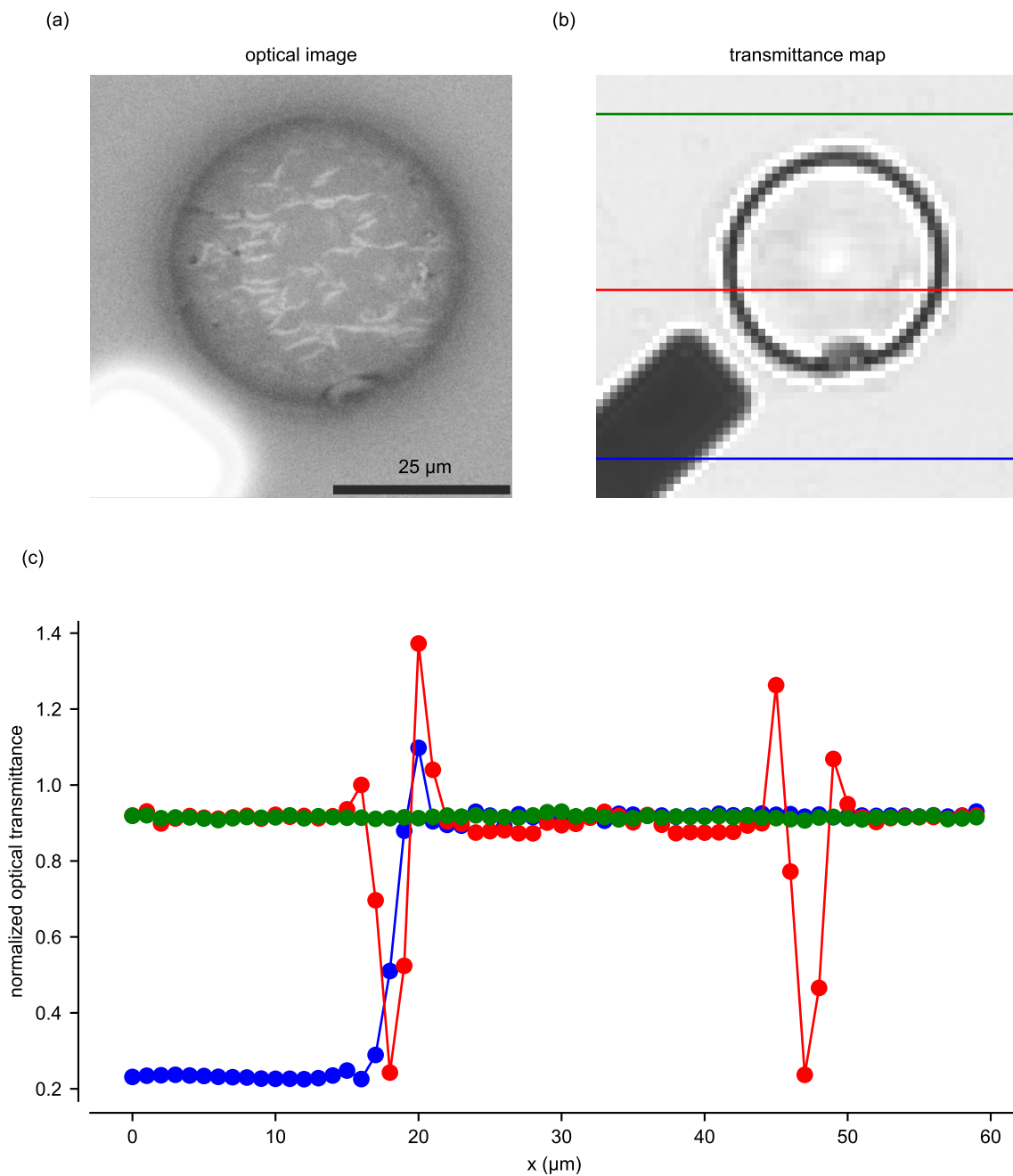
Figure 6.8 Optical microscopy image (a) and optical transmittance map (b) of 30 µm graphene microelectrode with Au conduction path (bright in (a) and dark in (b)). At this stage the entire MEA is covered in 5 µm SU-8 insulator except the electrode. (c) The linescans along the lines in (b) show light scattering at the edge of the electrode where the transmittance drops and jumps at the graphene - SU 8 edge.

6.6 Application of graphene MEA

Chicken heart cells were cultured on graphene microelectrodes by Sandra Buckenmaier and inspected in the transmission mode of the optical microscope where the cells directly on the transparent electrodes are visible (see figure 6.9 (a)). The electrophysiological recordings obtained at day 5 showed signal amplitudes of up to 2 mV peak-to-peak and noise below 50 µV. The fAPs, seen in figure 6.9 (b), are in synch for all the nine electrodes, which is expected in the case of cardiac cells that tend to grow next to each other forming a carpet of cells atop the electrode field. However, the lower amplitude on the right bottom electrodes can be attributed to the distance of the active cell area from the sensing electrode. The signal-to-noise ratio in the case of graphene microelectrodes was 40 with the noise peak-to-peak being $<$50 µV (d). The noise can be directly correlated to the real part of the magnitude impedance. Figure 6.9 (e) compares the magnitude and real impedance of standard TiN and graphene microelectrodes of the same size (30 µm). At 1 kHz, graphene (3 MΩ) displays 15-times larger magnitude impedance compared to TiN (200 kΩ).

The averaged real impedance, over the 1 Hz-3.5 kHz frequency range, is 7.7 MΩ for graphene and 370 kΩ for TiN. From these values and the equation 4.2, the thermal noise of graphene (21 µV) is ~ 5 times higher than TiN (4 µV). The real noise during electrophysiology is a combination of thermal and biological noise. Hence the real noise is several times larger than the theoretically calculated thermal noise as seen in figure 6.9 (d). The repolarization at the end of the fAP, which is driven by the K^+/Ca^+ ions, is barely visible in the case of transparent graphene microelectrodes.

Fluorescence microscopy of transgenic mouse retina with EYP-labelled ganglion cells through the graphene MEA demonstrated imaging of neurons directly through the transparent microelectrodes (figure 6.10). The experiment was performed by Meng-Jung Lee at the NMI. The non-transparent Au conduction paths were terminated 65 µm before the invisible microelectrodes. The opaque conduction paths are visible and so is the autofluorescent SU-8 (insulator). The electrodes are visible through the autofluroscent insulator.
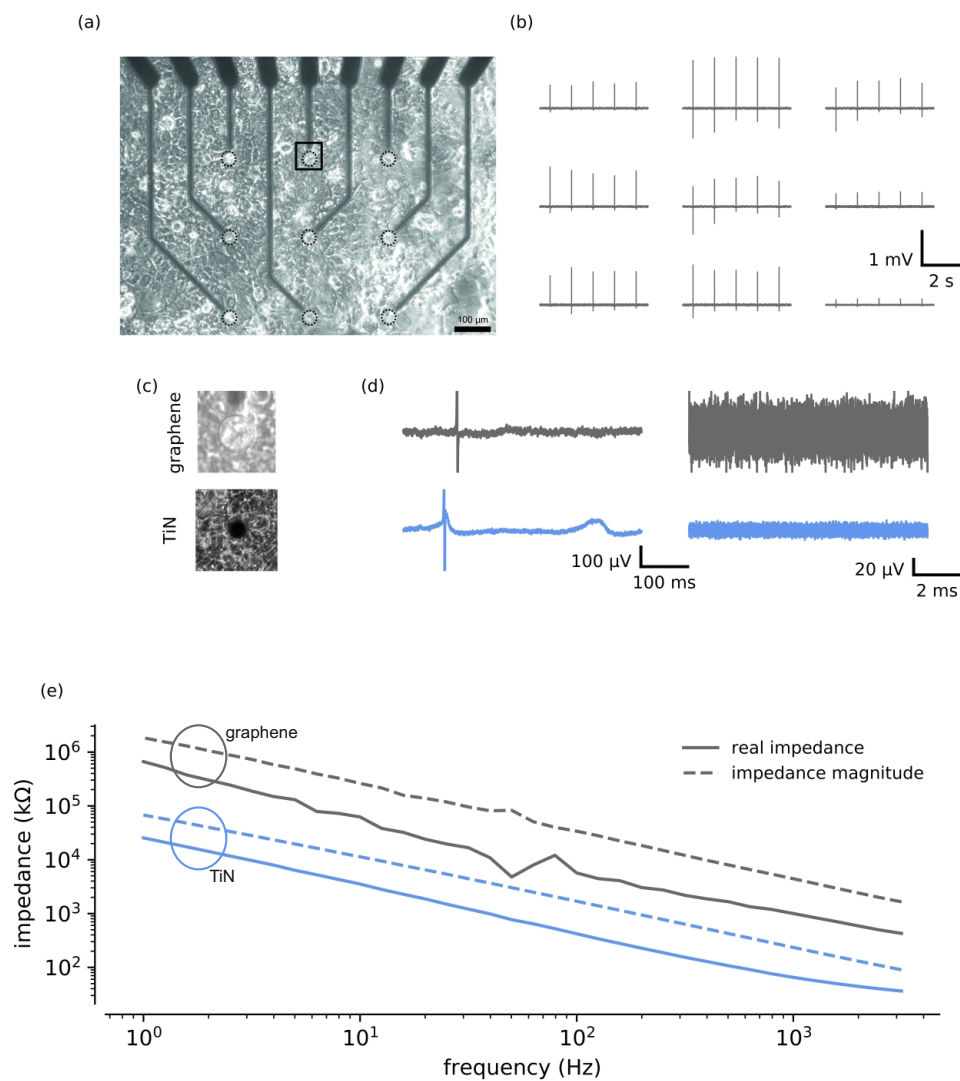
Figure 6.9 (a) Optical image, obtained with an inverted microscope, of a graphene microelectrode field with 9 electrodes where cardiac cells from chicken heart were cultivated. (b) The electrophysiological recordings of the cardiomyocytes on day 5 *in vitro* obtained with the electrodes seen in (a). The fAPs have up to ∼2 mV amplitude which confirms the functionality of graphene microelectrodes. (c) The cells are visible through the graphene electrode as compared to the commercially available TiN microelectrode. (d) One of the fAPs recorded with a graphene (grey) and TiN (blue) microelectrode. The "bump", which indicates the end of fAP, is missing in case of graphene. This can either be due to the cell-preparation or because of the high noise of graphene microelectrodes compared to TiN. (e) Impedance magnitude and real impedance of the graphene (grey) and TiN (blue) microelectrodes plotted against logarithm of frequency. The high impedance values of graphene compared to TiN explain the high noise levels seen in (d).

retina slice (wholemount) on graphene MEA
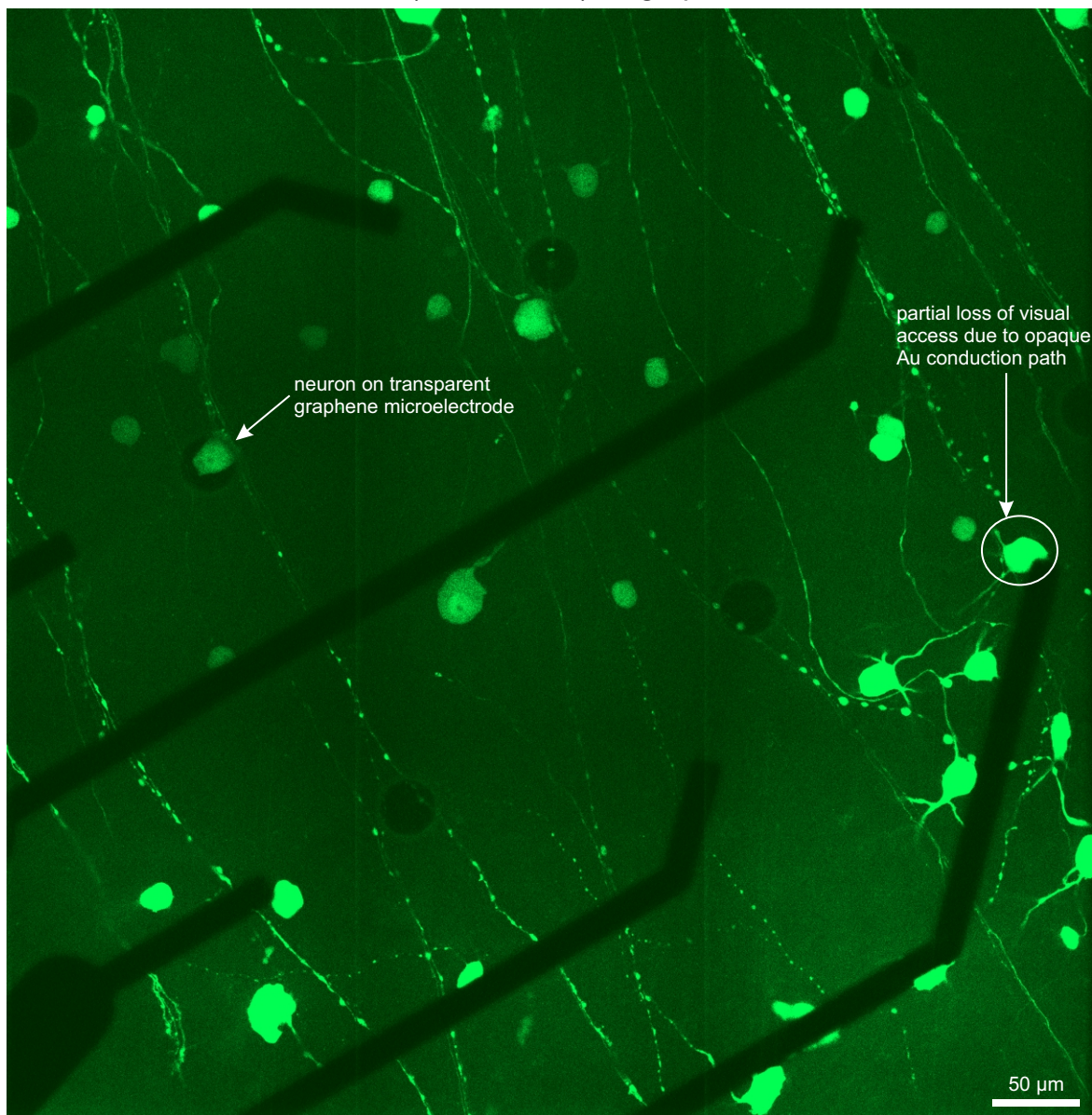
Figure 6.10 Fluorescent retina ganglion cells in the transgenic mouse retina observed through the graphene microelectrode field. The retina slicing and fluorescence microscopy was performed by Meng-Jung Lee.

6.7 Chapter summary

Graphene was produced by CVD at 800 °C, using commercially bought Cu foil as catalyst, and methane as the carbon source in argon and hydrogen atmosphere. The CVD process can be divided into three parts - Cu pretreament, annealing and graphene growth. The Cu was pretreated for 1 min in APS which is the Cu etchant, followed by annealing in the presence of argon. Graphene nucleation initiates at the (thermodynamically favourable) defect sites which are mainly the grain boundaries. Annealing at >700 °C increased the Cu grain size, reducing the grain boundaries which in turn reduced the nucleation density. The graphene grown on Cu was transferred onto the Au conduction paths following the polymer based transfer method where a thin layer of PMMA was spincoated onto the Cu with graphene, the Cu etched and the PMMA-graphene membrane fished out on the target region. Graphene was structured into ∼40 µm microelectrodes followed by SU-8 insulation of the Au conduction paths with ∼30 µm openings.

The graphene electrodes were investigated with Raman spectroscopy to check for SU-8 contamination where no SU-8 peaks were observed, hence contamination-free electrodes were confirmed. The defects, 2nd/3rd layer of graphene and wrinkles were reflected well in the Raman maps. Combination of Raman and SEM provides comprehensive information about the graphene quality.

The graphene microelectrodes were electrochemically characterized by performing electrochemical impedance spectroscopy. The impedance spectroscopy revealed (2.9 ± 0.3) MΩ magnitude impedance at 1 kHz. This value is more than 10 fold higher than that for the commercially available TiN microelectrodes and in synch with the theoretically calculated and the reported literature values. The thermal noise, calculated based on the electrochemical impedance results, of the graphene electrodes is 21 µV, about 5 fold larger than for the TiN electrodes. In addition, the measurement set-up has a noise in the range of 1.5–2 µV.

This magnitude of noise can be acceptable for recording the cardiac activity of the embryonic chicken heart cells. But in the case of neurons, where the activity can be as small as 50 µV, the noise can be an issue as it can be misinterpreted for activity. The optical transparency of graphene microelectrodes on 1 mm float-glass was 90 %. This enabled the optical inspection of cells through the graphene microelectrodes which was the aim of this work. However, the relatively poor electrical impedance of bare graphene makes it unsuitable for neuronal recordings.

The functionality of the graphene microelectrodes was confirmed by recording beating cardiomyocyte activity from chicken heart cells cultured *in vitro*. The confocal fluorescence imaging of transgenic mouse retina revealed the advantage of the transparent electrodes where the neurons directly on top of the electrodes were visible while the opaque Au conduction paths blocked the optical access.

7 Development of graphene/PEDOT:PSS MEA

Graphene microelectrodes were coated with the conducting polymer, PEDOT:PSS, essentially to lower the impedance while maintaining the optical transparency. The graphene/PEDOT:PSS microelectrodes were critically analysed by correlative Raman spectroscopy, optical and SEM imaging. Electrochemical analysis included impedance spectroscopy and cyclic voltammetry before and after PEDOT:PSS deposition. Optical transmittance was performed and correlated with specific impedance of the different electrodes. This chapter includes the fabrication details, optical transparency investigation, detailed Raman spectroscopy, electrochemical characterization and the electrophysiological recordings. This work was published in [24].

7.1 Fabrication of graphene/PEDOT:PSS microelectrodes

Spincoating PEDOT:PSS solutions (with or without other chemicals) and electropolymerization of EDOT in NaPSS solution are the most common methods of fabricating substrates with this conducting polymer. PEDOT:PSS is mixed with graphene oxide for applications such as supercapacitors [96, 97], thermoelectrical nanogenerators [98] and solar cells [99]. In other cases, graphene nano-platelets combined with PEDOT:PSS solution were spin coated for organic solar cells [100] and solid state capacitors [101]. Optical transparency was not a limitation for any of these applications and hence the values are seldom reported.

Reducing the electrochemical impedance was the main motivation for coating graphene microelectrodes. Electrodeposition of PEDOT:PSS has been reported on Iridium oxide [102], Au [6, 103, 104], alginate hydrogel with dispersed CNTs [105], or Au and Au/IrO$_x$-meshes [106] to record cellular electrical activity, both, *in vivo* and *in vitro*. Improved transparency (70 %), together with reduced impedance (0.64 Ω cm^2 for Au and 1.92 Ω cm^2 for Au/IrO$_x$), was reached with the aim of *in vivo* brain mapping by concurrent optical imaging and optogenetic interventions. [106]

Electrochemical deposition can be carried out galvanostatically (constant current) [6, 107, 108], potentiostatically (constant potential) [109] or by changing current and potential (cyclic voltammetry) [110, 111]. Morphology and electrochemical properties of the polymer are mainly governed by the deposition method and quality of the electrode surface. Scratches on the Au surfaces were reported to be the favorable nucleation sites during PEDOT:PSS deposition [112]. In the case of galvanostatic deposition, the thickness of PEDOT:PSS can be controlled by the current flown through the working electrode and the time of deposition. Slowly ramped current ensures uniform and well defined electropolymerization, in contrast to the fluffy structures resulting from the rapid current pulses. The nucleation and growth mechanism of the EDOT polymerization in NaPSS solution is under investigation, and the generally accepted mechanism is summarized below [110, 112].

The classical nucleation consists of induction periods and steady (or stationary) periods. During the induction periods, the monomer (EDOT) diffuses from the solution to the electrode surface followed by oxidation and coupling with the radical cation. The saturation of these oligomers (coupled monomer cations) in front of the electrode leads to precipitation of the oligomer clusters generating the polymer nuclei. At this point, the process is (monomer) diffusion controlled. Progressive nucleation is defined as activation of new nucleation sites over the course of the electrochemical deposition, in addition to the nuclei formed at the beginning. The combination of different nucleation processes leads to the inhomogeneously grown PEDOT:PSS films. At the end, the different nuclei combine together and form polymer globules. The expansion of the polymer chains and growth of the globules on the electrode surface are the significant processes. When the oxidation potential is applied for a certain amount of time, the globules start overlapping and a second layer of much bigger polymer globules is formed. This observation was supported by optical and atomic force microscopy [112].
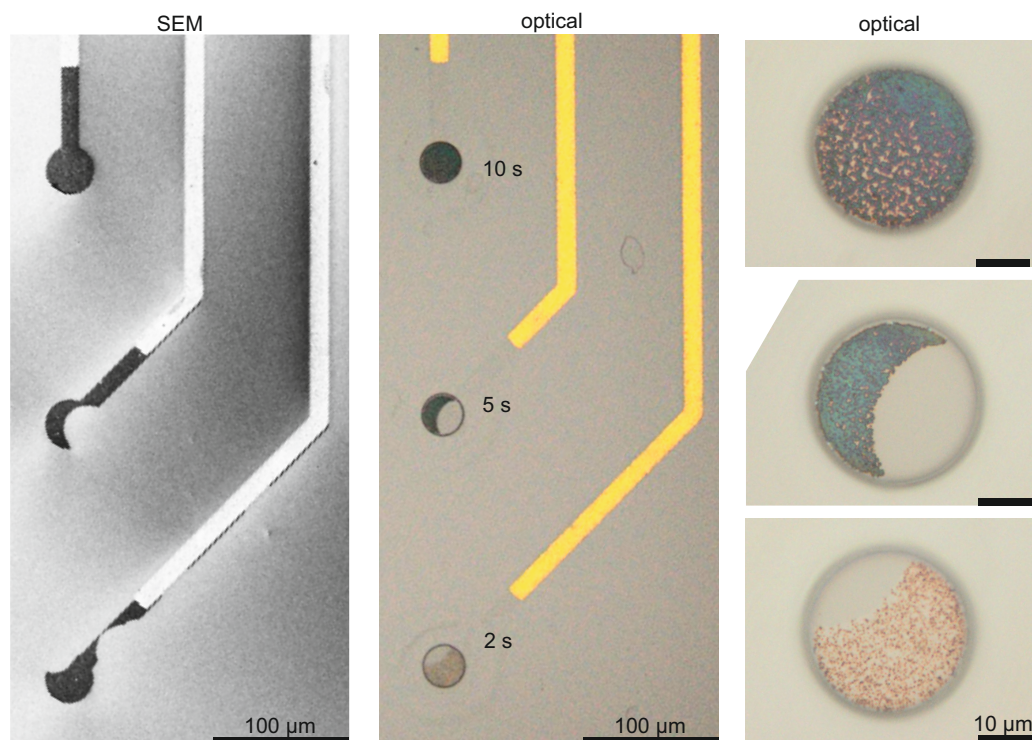
Figure 7.1 SEM and optical microscopy analysis of microelectrodes with different PEDOT:PSS electrodeposition times. The SEM was performed prior to insulator deposition and optical imaging upon electrodeposition. The PEDOT:PSS showed continuous coverage for 10 s, 5 s and 2 s and followed the graphene structure.
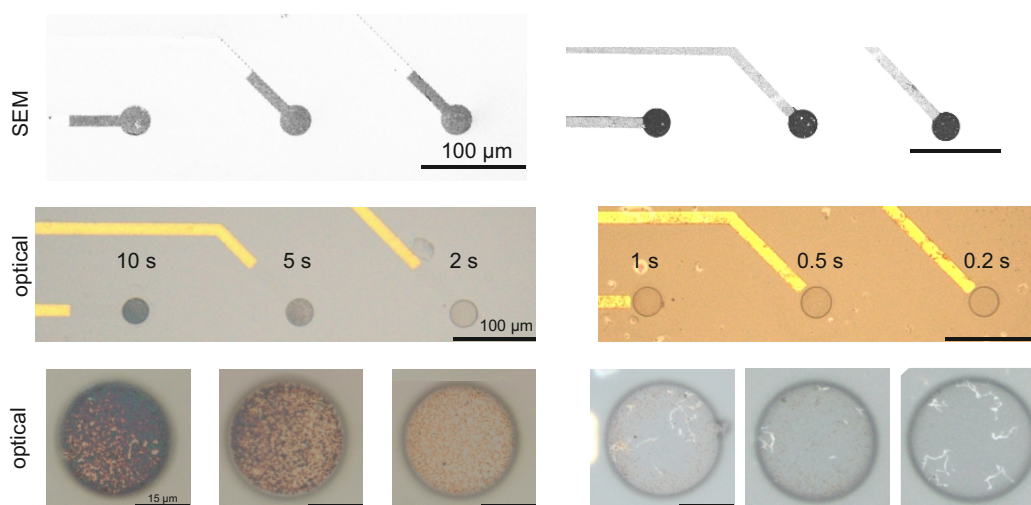
Figure 7.2 SEM and optical microscopy analysis of microelectrodes with different PEDOT:PSS electrodeposition times. The SEM was performed prior to insulator deposition and optical imaging upon electrodeposition. The PEDOT:PSS showed uniform coverage for 10 s, 5 s, and 2 s and selective coverage for 1 s, 0.5 s, and 0.2 s.

PEDOT:PSS was galvanostatically deposited on graphene microelectrodes following the details mentioned in section 3.2.3. The structured graphene electrode field was investigated with SEM prior to application of the SU-8 insulator. As mentioned before, the SEM in-lens detector offers strong contrast between the graphene covered Au conduction paths (bright) and graphene (dark) (see figure 7.1) revealing electrically active CVD graphene. PEDOT:PSS was found to change from light brown (2 s) to dark blue (10 s). The conducting polymer was observed to follow the graphene surface which confirmed the success of electrodeposition and ruled out the possibility of any other kind of deposition.

The amount of PEDOT:PSS increases with increasing electrodeposition time, which in turn is expected to lower the electrochemical impedance. Keeping the impedance and optical transparency in mind, the electrodeposition time was further reduced down to 0.2 s. The PEDOT:PSS globules became sparse with decreasing electrodeposition time (see figure 7.2). The short deposition times reduced the contribution of progressive nucleation, which means the activation of new nucleation sites over the course of the electrodeposition process is controlled. This argument is supported by the absence of a continuous PEDOT:PSS layer optically for 1 s, 0.5 s and 0.2 s. The graphene/PEDOT:PSS microelectrodes were further analysed by Raman spectroscopy and the results were correlated with SEM and optical images. The electrochemical impedance effect of the graphene quality is discussed in section 7.3.

7.2 Qualitative analysis - Raman spectroscopy, SEM and optical imaging
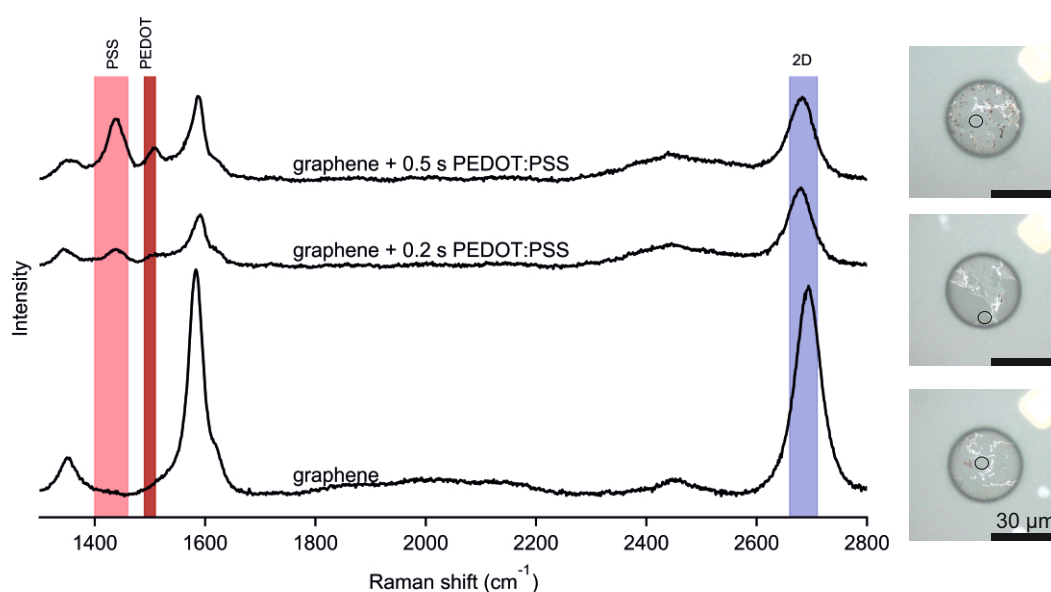
Figure 7.3 Raman point spectra obtained from three different microelectrodes using 532 nm (green) laser with 6.5 mW power and 10 s integration time after baseline subtraction. The black circle in the optical images indicates the Raman acquisition region. The PEDOT, PSS and the graphene (2D) peaks are highlighted. The PEDOT:PSS layer damps the graphene intensity and the polymer peaks are stronger with increasing electrodeposition times. The curves are vertically offset for clarity

The symmetric and antisymmetric C=C in-plane stretching modes in PEDOT:PSS appear at 1429 cm^{-1} and 1509 cm^{-1}, respectively. Thiophene ring stretching is seen at 1434 cm^{-1} and the π-π stacking interaction between PEDOT:PSS chains and graphene leads to a 2D peak shift. This peak shift is concrete evidence for the interaction between graphene and the conducting polymer. [79, 80, 98, 110, 113]

For longer ($>$2 s) electrodeposition times, PEDOT:PSS optically appeared to uniformly cover the graphene microelectrode. On the other hand, for shorter ($<$2 s) durations, brown clumps were observed along the cracks, wrinkles in graphene. Raman spectroscopy revealed the characteristic PEDOT:PSS peaks, around 1434 cm^{-1} and 1505 cm^{-1}, and the graphene peaks, G at 1590 cm^{-1} and 2D at 2700 cm^{-1} (see figure 7.3). PEDOT and PSS peak intensities increased with increasing thickness and damped the graphene signals. The spectrum from the brown clumps was expected to show stronger PEDOT and PSS signals and the spectra were acquired from regions which appeared transparent (circled in figure 7.3). In addition, the individual spectra are obtained from a $\sim$1 μm ($\sim$0.785 μm^2) region on the sample which is very small compared to the microelectrode with 30 μm diameter ($\sim$707 μm^2). Hence, a collec-

tive Raman spectra - Raman map was obtained from 2 s (figure 7.4), 0.5 s (figure 7.5) and 0.2 s (figure 7.6) electrodeposition to investigate the PEDOT:PSS coverage of the 30 µm graphene electrode. The Raman spectroscopy parameters such as the laser, power, exposure time and Raman map resolution are given in the respective figure captions.
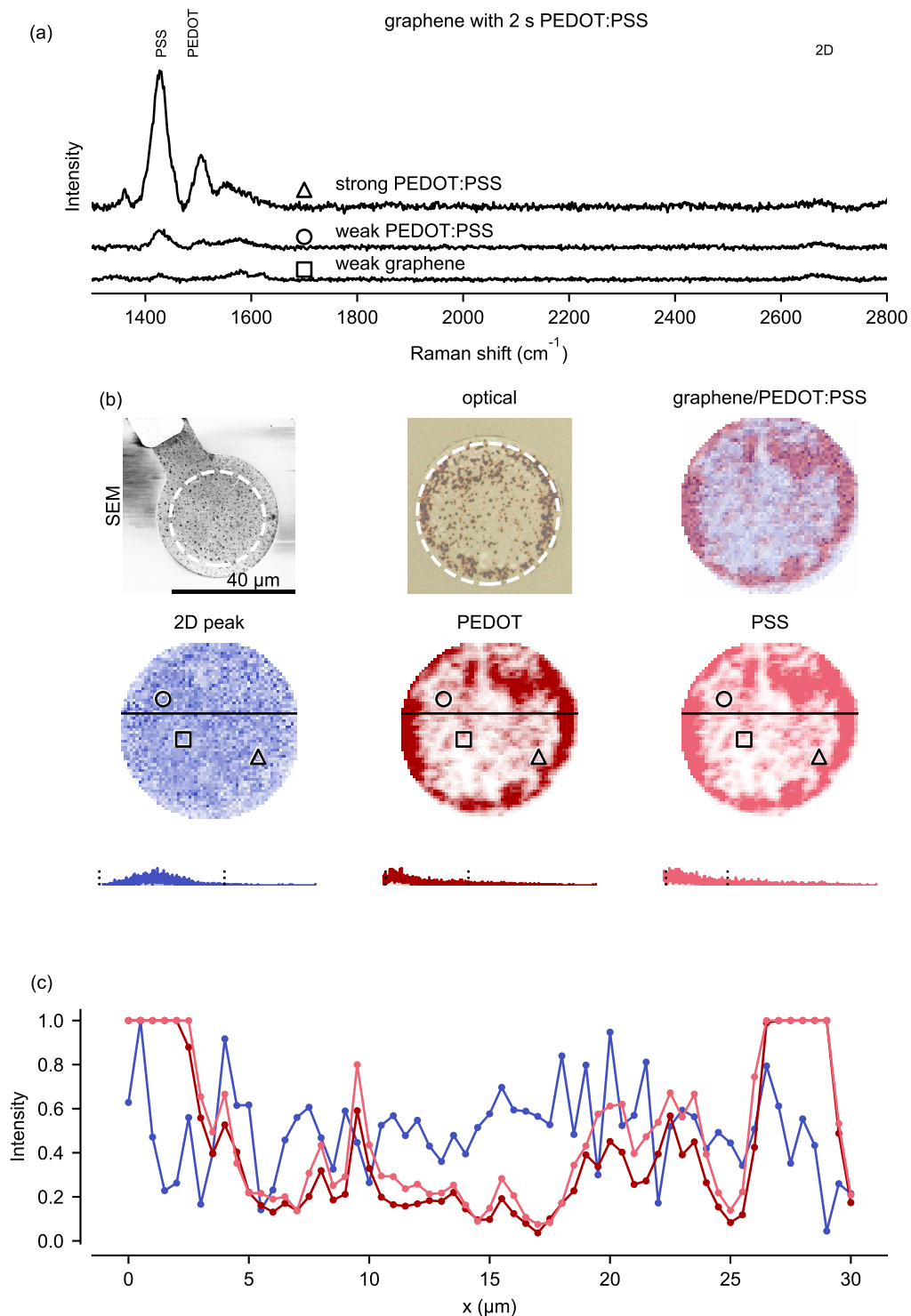
Figure 7.4 Qualitative analysis of the graphene/PEDOT:PSS electrodes with 2 s electrodeposition. Raman specta were obtained with 0.5 µm resolution using 532 nm laser with ∼33 mW and 0.5 s acquisition time.

Graphene (2D) and PEDOT:PSS peaks were integrated, normalized and plotted producing the re-
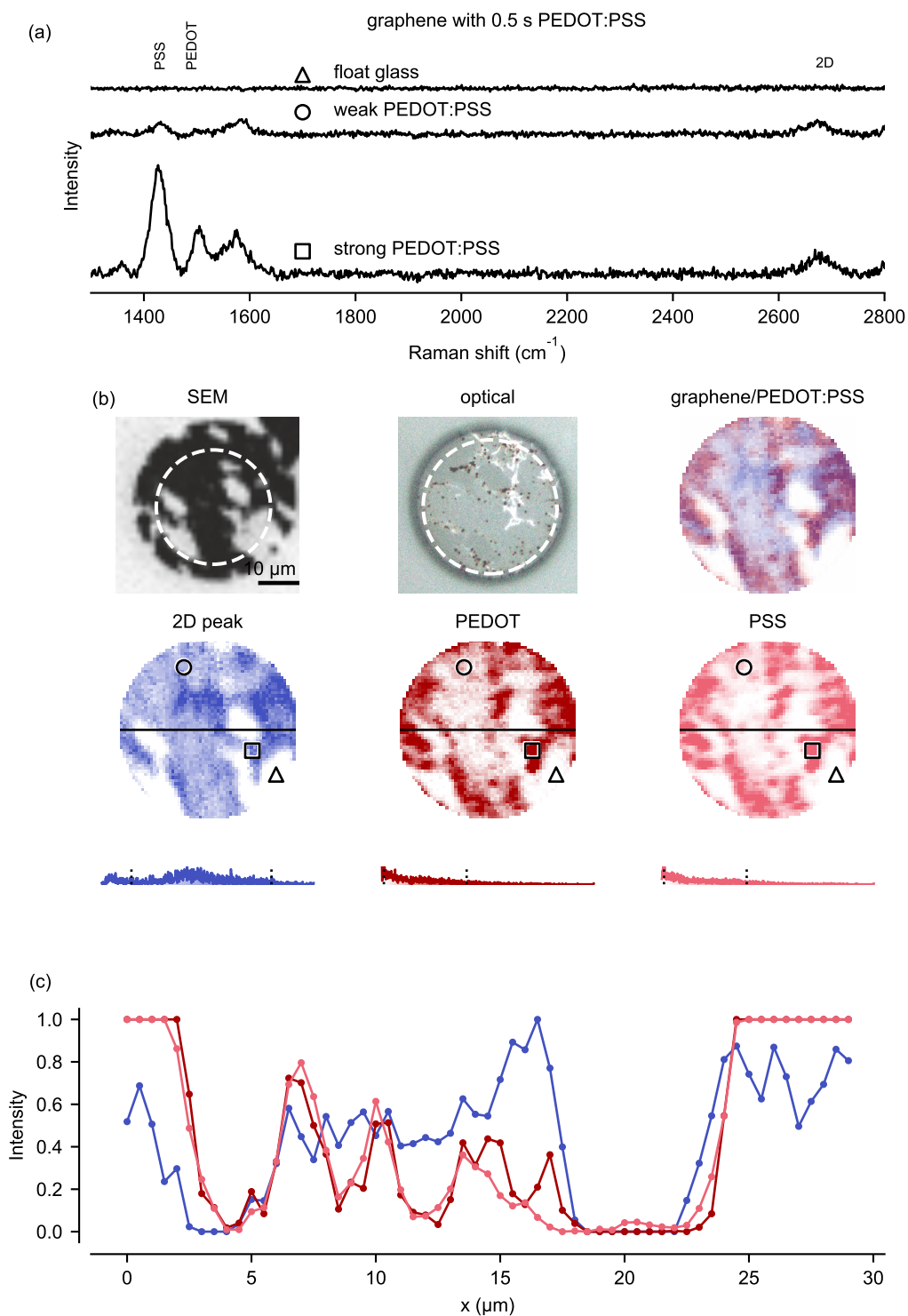
Figure 7.5 Qualitative analysis of the graphene/PEDOT:PSS electrodes with 0.5 s electrodeposition. Raman spectra were obtained with 0.5 μm resolution using a 532 nm laser with ∼33 mW and 0.5 s acquisition time.

spective Raman maps. 2D was chosen over the G peak as the latter is closer to the PEDOT:PSS peaks and hence the integration might contain conducting polymer contribution. Graphene and PEDOT:PSS maps were merged for better understanding of the microelectrode. SEM images in all three cases were obtained prior to SU-8 deposition. Optical images and Raman maps were acquired after PEDOT:PSS electrodeposition. The point spectra are vertically offset for clarity. Windowing ranges are shown in the
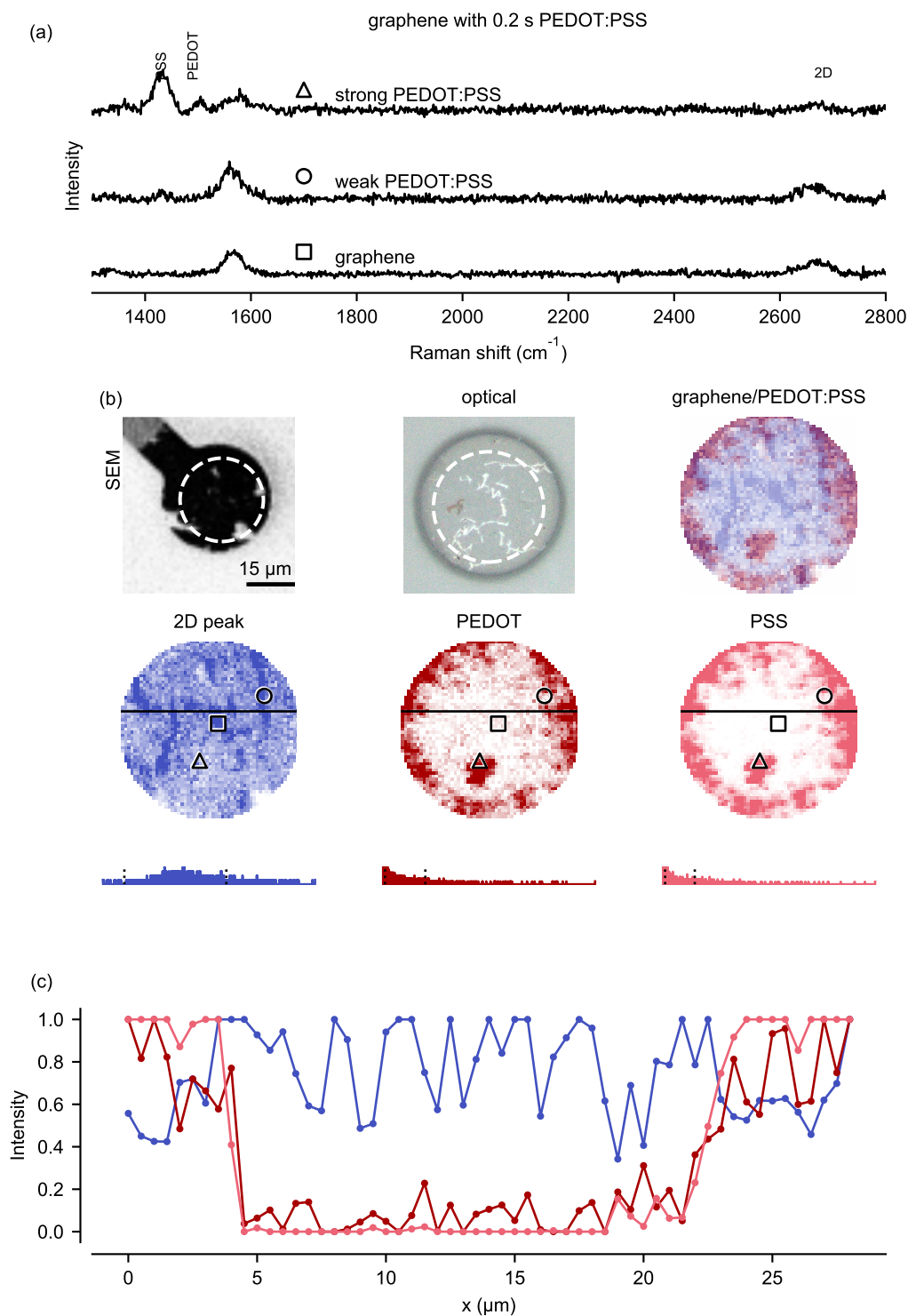
Figure 7.6 Qualitative analysis of the graphene/PEDOT:PSS electrodes wit 0.2 s electrodeposition. Raman spectra were obtained with 0.5 µm resolution using a 532 nm laser with ∼33 mW and 0.5 s acquisition time.

histograms of the maps.

The PEDOT and PSS peaks were observed in the regions which optically appeared transparent with the peak intensity being smaller than that of the darker regions. Raman spectroscopy offered insights in the PEDOT:PSS coverage of the transparent graphene microelectrodes. The SEM, optical imaging and Raman spectroscopy altogether offered a comprehensive analysis of the graphene/PEDOT:PSS micro-

electrode.

7.3 Electrical characterization

Figure 7.7 Impedance magnitude and phase plotted against frequency for different PEDOT:PSS electrodeposition times. The impedance was found to decrease with increasing deposition time.

The PEDOT:PSS deposition brought down the magnitude impedance (at 1 kHz) from $(2.9 \pm 0.4)\,\text{M}\Omega$ $(21\,\Omega\,\text{cm}^2$ for pure graphene) to $(42 \pm 2)\,\text{k}\Omega$ $(0.3\,\Omega\,\text{cm}^2$, for graphene with 10 s PEDOT:PSS). The dashed line in figure 7.7 shows the drop of impedance magnitude at 1 kHz with increasing amount of PEDOT:PSS which aligns with the expectation. The phase curve reveals that the graphene/PEDOT:PSS microelectrodes are predominantly capacitive for lower and resistive for higher frequencies. This is different from pure graphene microelectrodes where the phase showed capacitive behaviour for most of the frequency range. Capacitance dominates for lower frequencies as the imaginary impedance contribution, which is inversely proportional to the frequency, increases. Hence, from the electrochemical impedance point of view, the capacitive behaviour should begin as late as possible while going from higher to lower frequency. The phase begins transitioning from capacitive to resistive around $\sim 100\,\text{Hz}$ for 10 s and $\sim 1000\,\text{Hz}$ for 0.2 s.

The frequency range of the flat region in the real impedance curves (figure 7.8) increases with increasing PEDOT:PSS amounts. This is because, while going from higher to lower frequency, the electrodes are resistive for a larger frequency range. The large noise in the lower frequencies can be background or instrument noise.

Improved signal-to-noise ratio is the main reason behind reducing the electrode impedance. Thermal, measurement set-up and biological are the three main sources of noise during electrophysiology. Thermal noise is generated by the charge carriers inside the electrical conductor and can be accounted for following the Johnson-Nyquist equation:

$$\upsilon = \sqrt{4k_B T R \Delta f}$$

where T is temperature and $R\,\Delta f$ is the integration of the real impedance over the measured bandwidth, which in this case was 0.1 Hz-3.5 kHz. The average real impedance was calculated over this bandwidth. The calculated rms noise values are listed in table 7.1. The expected thermal noise decreased $\sim$ 2-fold with $\sim$ 4-fold decrease in the average real impedance $(117 \pm 37)\,\text{k}\Omega$ (0.2 s) to $(28 \pm 3)\,\text{k}\Omega$ (10 s).
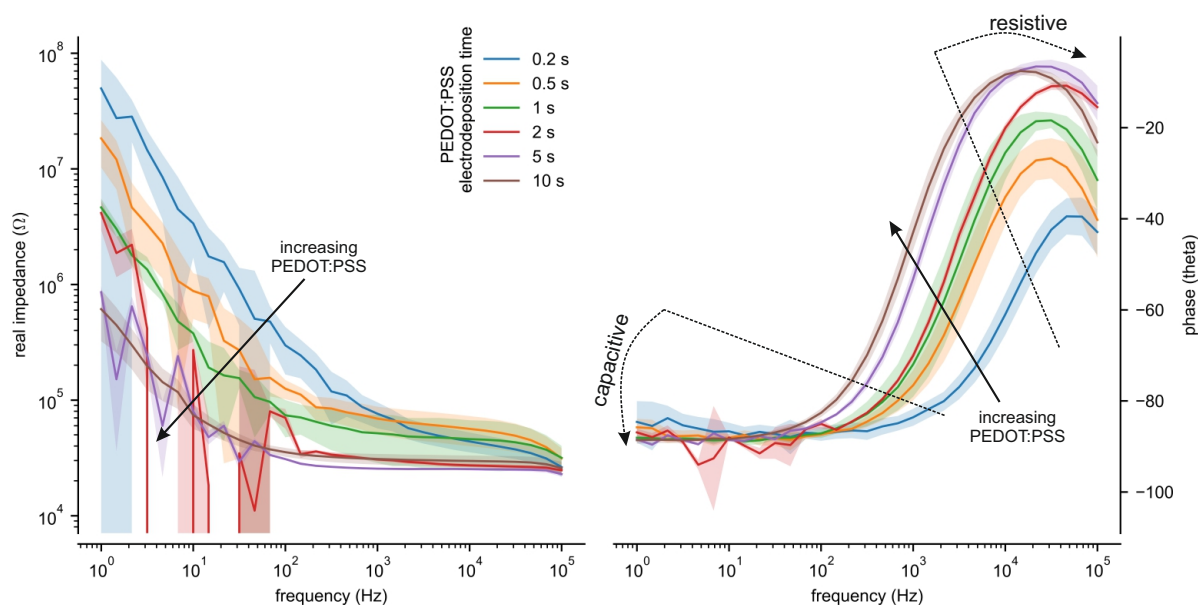
Figure 7.8 Real impedance and phase plotted against frequency for different PEDOT:PSS electrodeposition times. The impedance was found to decrease with increasing deposition time. The large standard deviation in lower frequencies results from the measurement noise.

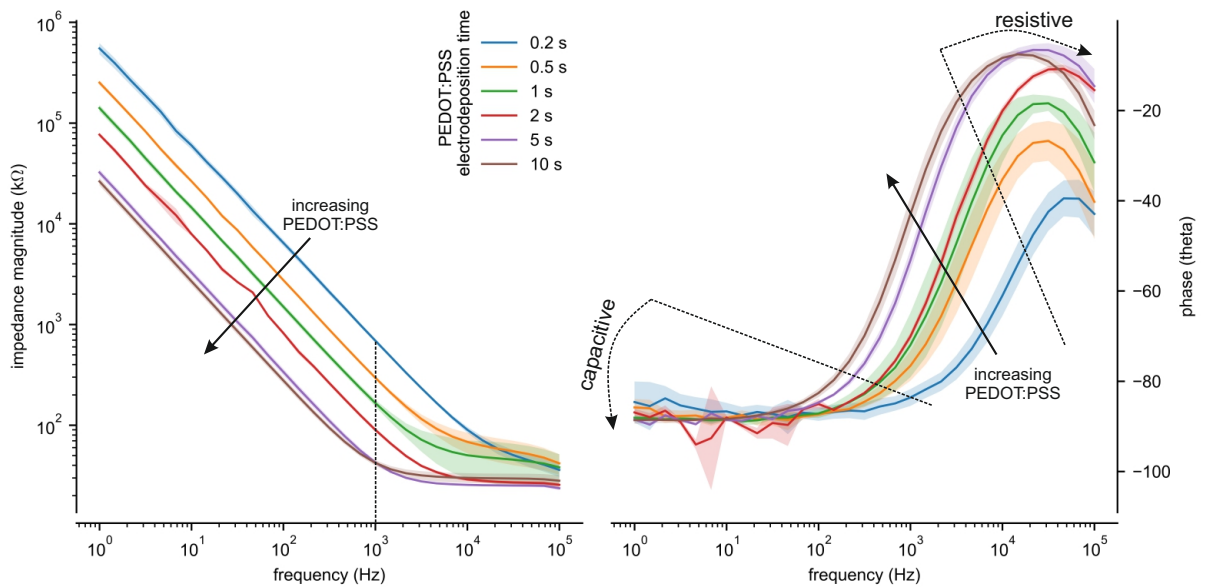| PEDOT:PSS deposition time	avg real impedance	thermal noise (rms)
10 s	$(28 \pm 3)\,k\Omega$	$1.27\,\mu V$
5 s	$(24.0 \pm 0.3)\,k\Omega$	$1.18\,\mu V$
2 s	$(28.0 \pm 2.5)\,k\Omega$	$1.27\,\mu V$
1 s	$(51 \pm 20)\,k\Omega$	$1.71\,\mu V$
0.5 s	$(75 \pm 19)\,k\Omega$	$2.01\,\mu V$
0.2 s	$(117 \pm 37)\,k\Omega$	$2.60\,\mu V$

Table 7.1 Average real impedance over 0.1 Hz-3.5 kHz and the calculated Johnson-Nyquist noise of graphene microelectrodes of PEDOT:PSS electrodeposited for different times.

7.3.1 Effect of non-uniform graphene

electrode	avg real impedance	thermal noise (rms)
uniform graphene	$461\,k\Omega$	$5.15\,\mu V$
non-uniform graphene	$1209\,k\Omega$	$8.35\,\mu V$
uniform graphene + 0.5 s PEDOT:PSS	$62\,k\Omega$	$1.89\,\mu V$
non-uniform graphene + 0.5 s PEDOT:PSS	$135\,k\Omega$	$2.79\,\mu V$

Table 7.2 Average real impedance and calculated thermal noise for uniform and non-uniform graphene microelectrodes shown in figure 7.9 before and after 0.5 s PEDOT:PSS deposition.

Non-uniformity of pure graphene was found to cause ~ 1.6 fold higher thermal noise compared to uniform polycrystalline graphene (see section 6.4). The disparity in the thermal noise is dependent on the extent of non-uniformity. The real impedances of the same electrodes upon 0.5 s PEDOT:PSS electrodeposition are plotted in figure 7.9. As expected, the thermal noise reduced ~ 3 fold after the PEDOT:PSS coating. However, PEDOT:PSS deposited on the non-uniform graphene displayed ~ 1.5 fold higher thermal noise.

The magnitude impedance at 1 kHz for both graphene/PEDOT:PSS microelectrodes was $\sim 300\,k\Omega$. This is because, the PEDOT:PSS preferentially nucleates on the defect sites and in the case of non-uniform graphene there are more defects, such as edges, than in the uniform graphene. Based on this
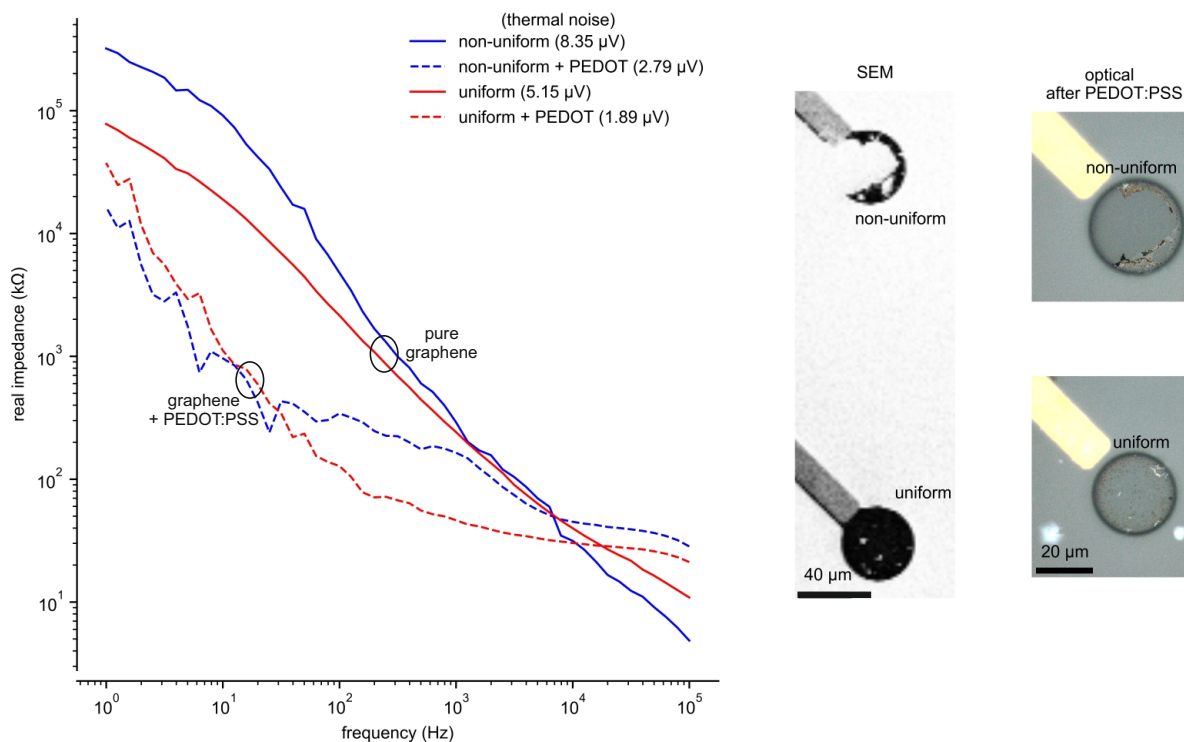
Figure 7.9 Real impedance vs frequency for uniform and non-uniform graphene before and after 0.5 s PEDOT:PSS electrodeposition time. The SEM images show the corresponding graphene microelectrodes before SU-8 and PEDOT:PSS deposition. Optical images were obtained after the PEDOT:PSS electrodeposition. The average real impedance and thermal noise values are in table 7.2.

value only, both the electrodes could pass the quality test. A closer look at the impedance magnitude curve meant extracting the real impedance which is plotted in figure 7.9. The average real impedance was found to be about twice as high which results in the non-uniform electrode showing ~ 1.5 fold higher noise than the uniform graphene electrode with the same duration of PEDOT:PSS electrodeposition. This stresses the fact that the current method of using magnitude impedance at 1 kHz is therefore an incomplete indicator in the production of low-noise microelectrodes.

7.3.2 Cyclic voltammetry

$$C = \frac{\int_{E1}^{E2} I dE}{\nu(E_2 - E_1)} = \frac{\int_{-0.5V}^{0.5V} I dE}{(0.2V/s)(0.5V - (-0.5V))} \tag{7.1}$$

The flat region in the CV curves indicates the capacitance of the electrode. The specific charge storage capacitance can be calculated by dividing the integrated current density of the capacitive region of the CV by the scan rate. The mostly rectangular shape shows that the graphene/PEDOT:PSS electrodes have higher capacitance than the bare graphene. The increases in the current density with increasing thickness of the PEDOT:PSS support the decrease in the impedance magnitude. Capacitance, calculated following the equation 7.1, increased with the amount of PEDOT:PSS. This is due to the higher surface area, owing to the porous nature of PEDOT:PSS, available for charge transfer. The capacitance of pure graphene was 0.65 nF, which increased up to 9.41 nF with the highest deposition time 10 s.
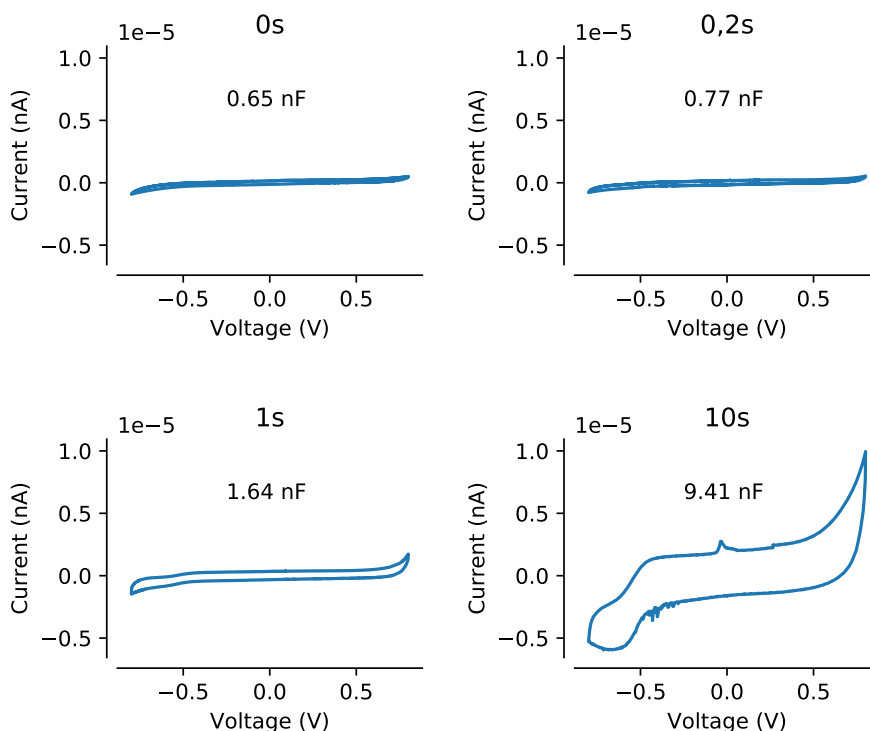
Figure 7.10 CV is measured as a curve between voltage (x-axis) and current (y-axis). The area under the curve is the specific capacitance which increases with increasing PEDOT:PSS amount (deposition time). The capacitance values in nF were calculated following equation 7.1. The impedance magnitude reduces (evident in figure 7.7) with increasing specific capacitance.

7.4 Optical characterization

PEDOT:PSS coated on a Au nanomesh was reported to display upto 65 % transparency for electrophysiology [106]. Here the optical characterization was performed following the details given in section 4.7. Graphene microelectrodes covered with different amounts of PEDOT:PSS were mapped with ~1 µm resolution (see figure 7.11 (a)). Each pixel in the transmittance map corresponds to the normalized value of the data averaged over 400–700 nm wavelength. The linescans across the microelectrodes with 0.5 s, 2 s and 5 s PEDOT:PSS were obtained separately with the same resolution of ~1 µm. The linescans for pure graphene and graphene with 0.2 s, 1 s and 10 s were extracted from the transmittance map along the lines indicated in figure 7.11 (a). Light scattering at the electrode-insulator edge leads to drastic changes which is evident in the line-scans (see figure 7.11 (b)) around 10 µm and 40 µm where the transmittance is observed to go above 1.0. The scattering results in the white-dark-white rings around the microelectrodes. The microelectrode spans between these two scatterings and the transmittance was further averaged over the electrode. Graphene microelectrodes had transmittance values of about 90 % which lowered with increasing amount of PEDOT:PSS with the lowest being 50 % for 10 s electrodeposition (see figure 7.12). The decrease in transmittance was in favour of the electrochemical impedance which decreased 14 fold compared to 0.2 s electrodeposition and 65 fold compared to graphene only microelectrodes.
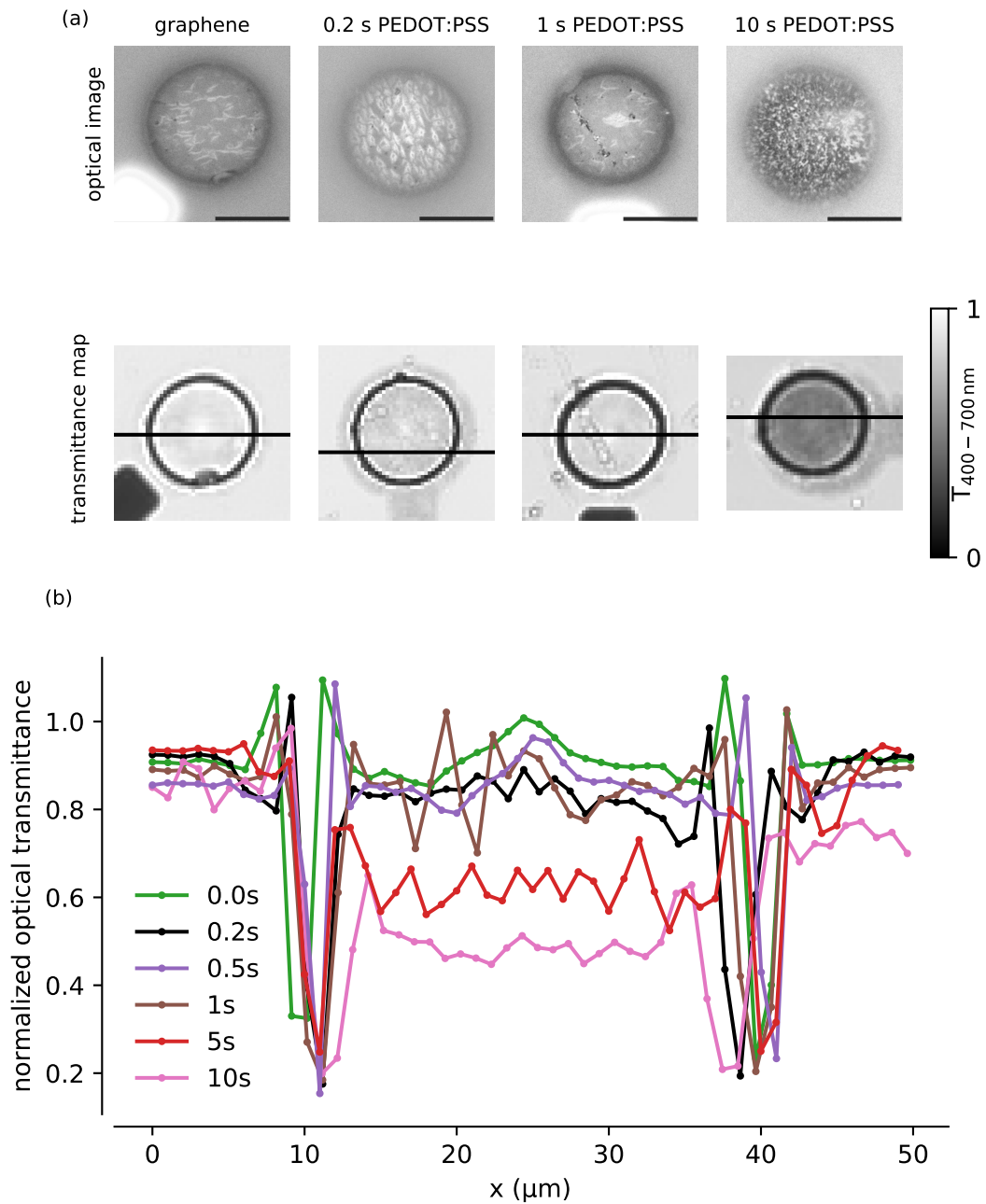
Figure 7.11 (a) Optical images and corresponding transmittance maps of (left to right) only graphene, graphene with 0.2 s, 1 s and 10 s plotted by averaging over the visible range (400 nm to 700 nm). The dark circle results from scattering of light at the edge between electrode and approximately 5 μm high SU-8 insulator. The scale bar corresponds to 20 μm. (b) Averaged transmittance value plotted across the electrode along the black lines indicated in (a). The electrode extends approximately between 10 μm and 40 μm on the x-axis.
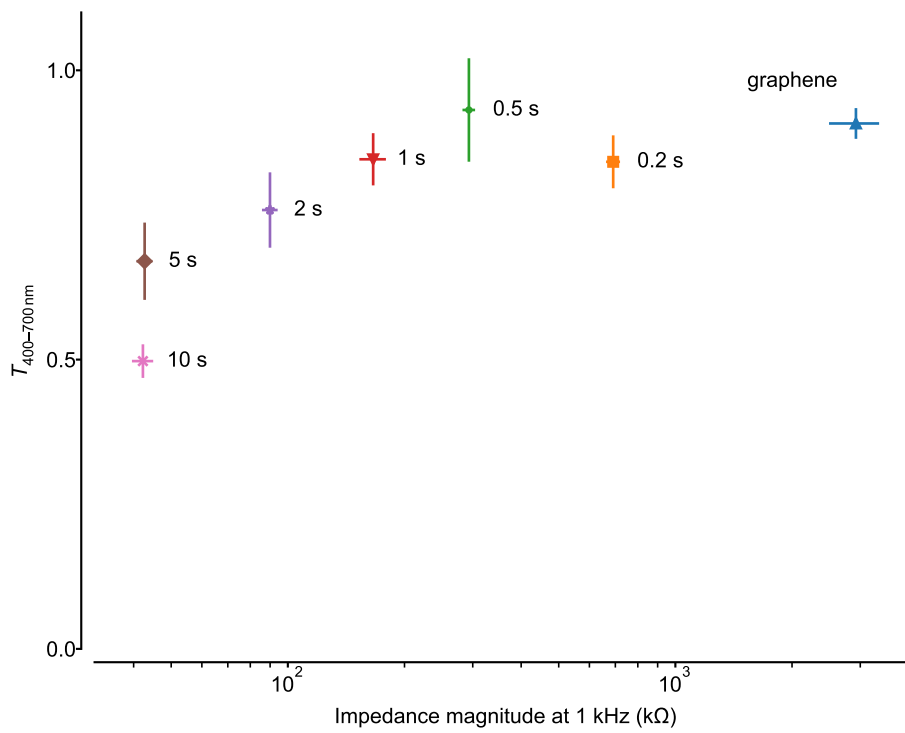
Figure 7.12 Transmittance averaged over the microelectrodes with different PEDOT:PSS amounts plotted against impedance magnitude at 1 kHz. The transmittance decreased from 90 % (pure graphene) to 50 % (graphene with 10 s PEDOT:PSS electrodeposition) with the advantage of a reduction in impedance magnitude that is 14 fold compared to 0.2 s electrodeposition and 65 fold compared to graphene only microelectrodes.

7.5 Application of graphene/PEDOT:PSS MEA
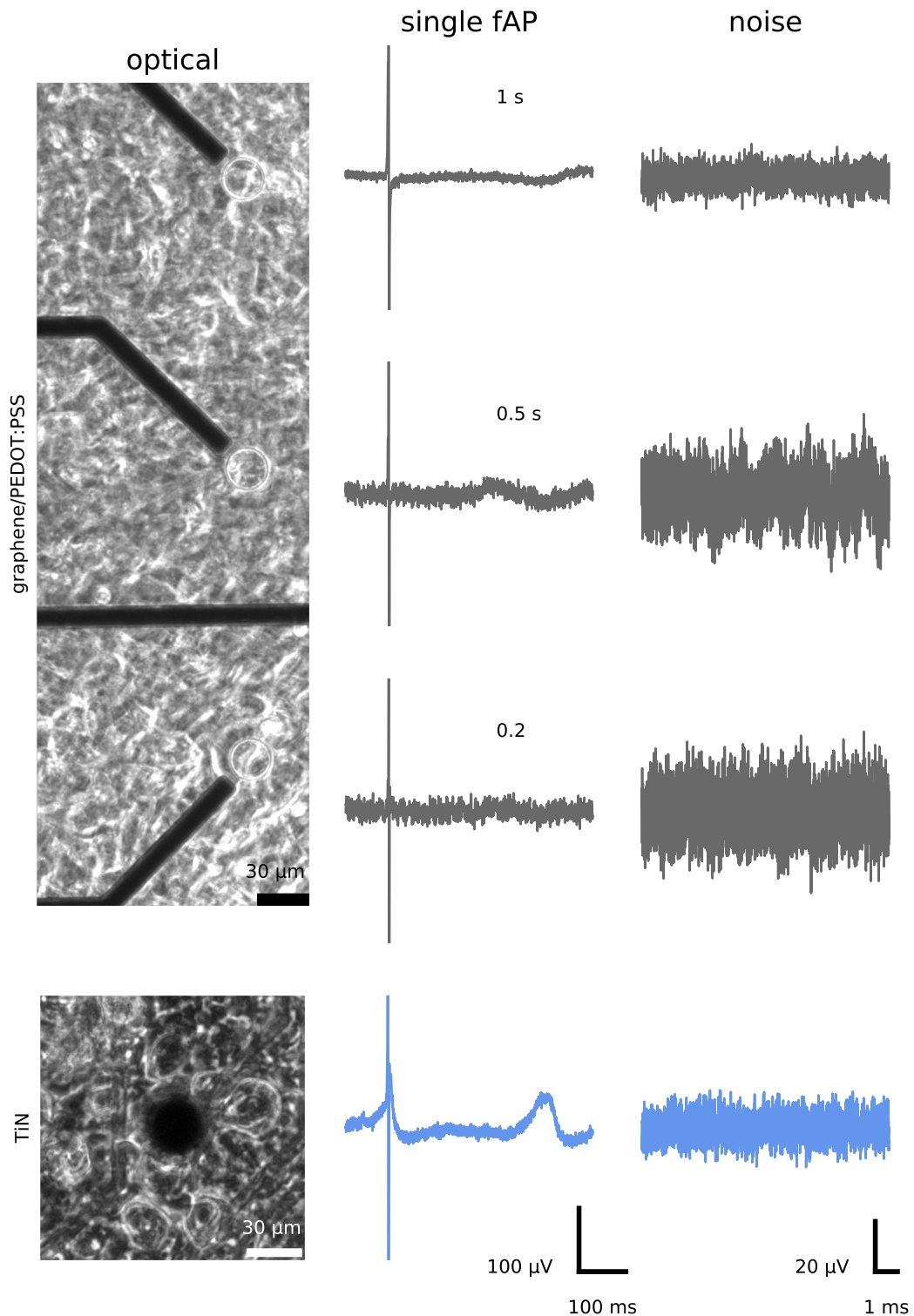
Figure 7.13 Optical microscopy and electrophysiology with graphene/PEDOT:PSS and TiN electrodes. Cardiomyocytes are visible through the transparent graphene/PEODT:PSS electrodes and the optical access is lost in the case of the TiN electrode. The single fAP signal amplitude is comparable in all cases. The noise, on the other hand, is observed to increase with decreasing amounts of PEDOT:PSS, namely for 0.5 s and 0.2 s depositions. The RMS noise for 0.2 s and standard TiN is comparable and about ∼2.5 μV.

The applicability of the graphene/PEDOT:PSS microelectrodes was accessed by culturing embryonic chicken heart cells. The field action potentials were recorded from the graphene microelectrodes with 1 s, 0.5 s and 0.2 s PEDOT:PSS (see figure 7.13). These microelectrodes were selected over the longer electro-deposition times as they displayed higher electrochemical impedance values and hence higher thermal noise values among the graphene/PEDOT:PSS microelectrodes. Graphene microelectrodes with 10 s, 5 s and 2 s showed lower electrochemical impedance values, hence lower thermal noise which is expected to result in better electrophysiological recordings. According to table 7.2, the thermal noise for 1 s, 0.5 s and 0.2 s is 1.71 μV, 2.01 μV and 2.6 μV, respectively. The thermal noise decreases with decreasing electrochemical impedance, which decreases with increasing PEDOT:PSS electrodeposition time. The depolarization component which is mainly driven by Na^+ was recorded for all three electrodes. However, the end of the fAP repolarization which is driven by K^+ was not observed. Electrophysiological recordings are heavily dependent on the health of the biological cells, which is different from culture to culture. The fAP repolarization was also missing in the control cell culture performed in parallel to these graphene/PEDOT:PSS microelectrodes on TiN microelectrodes. The recording and the optical image in the last row of figure 7.13 is from a different cell culture experiment performed on a different day.

Optical observation was possible with the inverted microscope with the cells atop. Similar to the Au conduction paths in case of the graphene/PEDOT:PSS electrodes, the conventional TiN electrodes blocked the view of the cells. This is especially critical in case of neurons as they grow more sparsely than the cardiomyocytes here.

7.6 Chapter Summary

PEDOT:PSS was electrochemically deposited on graphene microelectrodes, mainly to lower the impedance, which in turn would improve the signal-to-noise ratio of the electrophysiological recordings. The electrodeposition time was varied from 0.2 s to 10 s. The conducting polymer appeared to follow the graphene geometry with preference to defect sites such as edges. PEDOT:PSS thickness increases with the electrodeposition time, and the coverage was optically evident from 2 s onwards. Raman spectroscopy was performed to investigate the shorter deposition times where darker clumps were seen optically. Raman maps of graphene with 0.5 s and 0.2 s PEDOT:PSS confirmed the presence of PEDOT and PSS in the regions which appeared transparent optically. Raman spectroscopy, SEM and optical imaging results altogether provided comprehensive qualitative analysis of the graphene/PEDOT:PSS electrodes.

The magnitude impedance decreased with increasing PEDOT:PSS thickness at the cost of optical transparency over the visible range. The graphene/PEDOT:PSS microelectrodes displayed transparencies in the range of 50–90 % with 42–700 kΩ impedance at 1 kHz. The theoretical thermal noise decreased to half with the average real impedance decreasing $\sim$ 4-fold over 0.1 Hz-3.5 kHz. CV revealed that the capacitance increased with increasing PEDOT:PSS amounts. An optimum balance between transparency and impedance was obtained by keeping in mind the wide scope of the MEA devices. Recording of the beating chicken cardiomyocytes showed excellent functionality of the transparent graphene/PEDOT:PSS microelectrodes, low noise during electrophysiology and simultaneous optical access.

8 Conclusion and Outlook

The goal of this work, to produce and investigate carbon based transparent electrodes for electrophysiology coupled with optical investigation, was reached. Three different carbon based microelectrodes were fabricated using - carbon nanostructures, graphene and graphene/PEDOT:PSS. The functionality of the different electrodes was proven by recording the electrogenic activity of cardiomyocytes. Optical transparency offered the possibility to combine electro- and opto-physiology. The improved electrochemical impedance lowered the thermal noise, which is crucial in order to obtain refined electrical recordings.

Carbon nanostructures showed excellent electrical properties which was further confirmed by electrophysiological recordings which were as good as the commercially available TiN electrodes. The optical transparency values were upto $\sim$40 % and had room for improvement. Graphene microelectrodes showed superior optical transmittance (90 %) but were limited on the electrochemical impedance ((2.9 ± 0.3) MΩ) front. This limitation was overcome by combining graphene with the conducting polymer - PEDOT:PSS. The resulting graphene/PEDOT:PSS microelectrodes displayed excellent electrochemical impedance (42–700 kΩ) with very little optical transmittance (50–90 %) compromise.

This work also offered insights useful for materials science. A qualitative analysis protocol for graphene based microelectrodes was developed and includes a combination of Raman spectroscopy, scanning electron and optical microscopy. The results in this work open up new possibilities in the fields of biology and materials science. In biology, the transparent electrodes can be used for novel applications like optogentics and calcium imaging. A correlative electro- and opto-physiology offers better understanding of neuronal networks and other cell types. Further research needs to be carried out regarding the long-term stability of the graphene-based microelectrodes for *in vivo* and *in vitro* recording of cellular signals.

The transparency of graphene makes it a promising candidate for replacement of the conduction paths which currently are made of Au or ITO. For going in the direction of an all-transparent MEA experiments can be performed with graphene conduction paths pulled further back than in this work (65 µm). Other materials derived from graphene such as graphene oxide, reduced graphene oxide, graphene inks, dyes, nanoplatelets and other forms can be investigated as either the conduction path or microelectrode material.

Bibliography

1. Ryynänen, T. *et al.* All Titanium microelectrode array for field potential measurements from neurons and cardiomyocytes-A Feasibility Study. *Micromachines* **2,** 394–409 (2011).

2. Thiébaud, P., De Rooij, N. F., Koudelka-Hep, M. & Stoppini, L. Microelectrode arrays for electrophysiological monitoring of hippocampal organotypic slice cultures. *IEEE Transactions on Biomedical Engineering* **44,** 1159–1163 (1997).

3. Seker, E., Berdichevsky, Y., Begley, M. R., Reed, M. L., Staley, K. J. & Yarmush, M. L. The fabrication of low-impedance nanoporous gold multiple-electrode arrays for neural electrophysiology studies. *Nanotechnology* **21** (2010).

4. Cogan, S. F., Guzelian, A. A., Agnew, W. F., Yuen, T. G. H. & McCreery, D. B. Over-pulsing degrades activated iridium oxide films used for intracortical neural stimulation. *Journal of Neuroscience Methods* **137,** 141–150 (2004).

5. Eick, S., Wallys, J., Hofmann, B., van Ooyen, A., Schnakenberg, U., Ingebrandt, S. & Offenhäusser, A. Iridium oxide microelectrode arrays for in vitro stimulation of individual rat neurons from dissociated cultures. *Frontiers in neuroengineering* **2,** 16 (2009).

6. Gerwig, R., Fuchsberger, K., Schroeppel, B., Link, G. S., Heusel, G., Kraushaar, U., Schuhmann, W., Stett, A. & Stelzle, M. PEDOT-CNT Composite Microelectrodes for Recording and Electrostimulation Applications: Fabrication, Morphology, and Electrical Properties. *Frontiers in Neuroengineering* **5,** 8 (2012).

7. Stett, A., Egert, U., Guenther, E., Hofmann, F., Meyer, T., Nisch, W. & Haemmerle, H. Biological application of microelectrode arrays in drug discovery and basic research. *Analytical and Bioanalytical Chemistry* **377,** 486–495 (2003).

8. Khudhair, D., Nahavandi, S. & Garmestani, H. *Emerging Trends in Neuro Engineering and Neural Computation* 41–60 (Springer, Singapore, 2017).

9. Fejtl, M., Stett, A., Nisch, W., Boven, K.-H. & Möller, A. in *Advances in Network Electrophysiology: Using Multi-Electrode Arrays* (eds Taketani, M. & Baudry, M.) 24–37 (Springer US, Boston, MA, 2006).

10. Zeck, G., Jetter, F., Channappa, L., Bertotti, G. & Thewes, R. Electrical Imaging: Investigating Cellular Function at High Resolution. *Advanced Biosystems* **1 (11),** 1700107 (2017).

11. Thomas, C. A., Loeb, G. E. & Okunj, L. M. A Miniature Microelectrode Array To Monitor the Bioelectric Activity of Cultured Cells. *Experimental Cell Research* **74 (1),** 61–66 (1972).

12. Ghane-Motlagh, B. & Sawan, M. Design and Implementation Challenges of Microelectrode Arrays: A Review. *Materials Sciences and Applications* **04,** 483–495 (2013).

13. Obien, M. E. J., Deligkaris, K., Bullmann, T., Bakkum, D. J. & Frey, U. Revealing neuronal function through microelectrode array recordings. *Frontiers in Neuroscience* **9,** 423 (2015).

14. Wheeler, B. C. & Nam, Y. In Vitro Microelectrode Array Technology and Neural Recordings. *Critical Reviews™ in Biomedical Engineering* **39,** 45–61 (2011).

15. Buzsáki, G. Large-scale recording of neuronal ensembles. *Nature Neuroscience* **7,** 446–451 (2004).

16. Won, S. M., Song, E., Zhao, J., Li, J., Rivnay, J. & Rogers, J. A. Recent Advances in Materials, Devices, and Systems for Neural Interfaces. *Advanced Materials* **1800534,** 1–19 (2018).

17. Spira, M. E. & Hai, A. Multi-electrode array technologies for neuroscience and cardiology. *Nature Nanotechnology* **8,** 83–94 (2013).

18. Hai, A., Shappir, J. & Spira, M. E. Long-term, multisite, parallel, in-cell recording and stimulation by an array of extracellular microelectrodes. *Journal of neurophysiology* **104,** 559–568 (2010).

19. Kuzum, D. *et al.* Transparent and flexible low noise graphene electrodes for simultaneous electrophysiology and neuroimaging. *Nature Communications* **5,** 5259 (2014).

20. Park, D.-W. *et al.* Graphene-based carbon-layered electrode array technology for neural imaging and optogenetic applications. *Nature Communications* **5,** 5258 (2014).

21. Lu, Y., Lyu, H., Richardson, A. G., Lucas, T. H. & Kuzum, D. Flexible Neural Electrode Array Based-on Porous Graphene for Cortical Microstimulation and Sensing. *Scientific Reports* **6,** 1–9 (2016).

22. Humphrey, D. R. & Schmidt, E. M. Extracellular Single-Unit Recording Methods. *Neurophysiological Techniques, II,* 1–64 (1977).

23. Multi Channel Systems MCS GmbH. *Microelectrode array (MEA) manual,* 1–131 (2017).

24. Kshirsagar, P., Dickreuter, S., Mierzejewski, M., Burkhardt, C. J., Chassé, T., Fleischer, M. & Jones, P. D. Transparent graphene/PEDOT:PSS microelectrodes for electro- and optophysiology. *Advanced Materials Technologies* (2018).

25. Boyden, E. S., Zhang, F., Bamberg, E., Nagel, G. & Deisseroth, K. Millisecond-timescale, genetically targeted optical control of neural activity. *Nature Neuroscience* **8,** 1263–1268 (2005).

26. F. Shirai, A. H.-T. Optogenetics: Applications in psychiatric research. *Psychiatry and Clinical Neurosciences* **71,** 363–372 (2017).

27. Deisseroth, K. Optogenetics. *Nature Methods* **8,** 26–29 (2011).

28. Smetters, D., Majewska, A. & Yuste, R. Detecting Action Potentials in Neuronal Populations with Calcium Imaging. *Methods* **18,** 215–221 (1999).

29. Yang, W. & Yuste, R. In vivo imaging of neural activity. *Nature Methods* **14,** 349–359 (2017).

30. Iijima, S. Helical Microtubles of Graphitic Carbon. *Letters To Nature* **353,** 737–740 (1991).

31. Bacon, R. Growth, structure, and properties of graphite whiskers. *Journal of Applied Physics* **31,** 283–290 (1960).

32. Ruoff, R. S. & Lorents, D. C. Mechanical and thermal properties of carbon nano tubes. *Carbon* **33,** 925–930 (1995).

33. Harris, P. J. F. *Carbon Nanotube Science - Synthesis, Properties and Applications* (Cambridge University Press, New York, 2009).

34. Yang, W., Thordarson, P., Gooding, J. J., Ringer, S. P. & Braet, F. Carbon nanotubes for biological and biomedical applications. *Nanotechnology* **18,** 412001 (2007).

35. Liu, Z., Tabakman, S., Welsher, K. & Dai, H. Carbon nanotubes in biology and medicine: In vitro and in vivo detection, imaging and drug delivery. *Nano Research* **2,** 85–120 (2009).

36. Bareket-Keren, L. & Hanein, Y. Carbon nanotube-based multi electrode arrays for neuronal interfacing: progress and prospects. *Frontiers in Neural Circuits* **6,** 1–16 (2013).

37. Novoselov, K. S., Geim, A., Morozov, S. V., Jiang, D., Zhang, Y., Dubonos, S. V., Grigorieva, I. V. & Firsov, A. A. Electric Field Effect in Atomically Thin Carbon Films. *Science* **306,** 666–669 (2004).

38. Du, X., Skachko, I., Barker, A. & Andrei, E. Y. Approaching ballistic transport in suspended graphene. *Nature Nanotechnology* **3,** 491–495 (2008).

39. Mayorov, A. S. *et al.* Micrometer-scale ballistic transport in encapsulated graphene at room temperature. *Nano Letters* **11,** 2396–2399 (2011).

40. Balandin, A. A., Ghosh, S., Bao, W., Calizo, I., Teweldebrhan, D., Miao, F. & Lau, C. N. Superior Thermal Conductivity of Single-Layer Graphene. *Nano Letters* **8,** 902–907 (2008).

41. Lee, C., Wei, X., Kysar, J. W. & Hone, J. Measurement of the Elastic Properties and Intrinsic Strength of Monolayer Graphene. *Science* **321,** 385–388 (2008).

42. Bunch, J. S. *et al.* Impermeable Atomic Membranes from Graphene Sheets. *Nano Letters* **8,** 2458–2462 (2008).

43. Nair, R. R., Blake, P., Grigorenko, A. N., Novoselov, K. S., Booth, T. J., Stauber, T., Peres, N. M. R. & Geim, A. K. Fine Structure Constant Defines Visual Transparency of Graphene. *Science* **320,** 1308–1308 (2008).

44. Meyer, J. C., Kisielowski, C., Erin, R., Rossell, M. D. & Crommie, M. F. Direct Imaging of Lattice Atoms and Topological Defects in Graphene Membranes. *Nano Letters* **8,** 3582–3586 (2008).

45. Sun, X., Liu, Z., Welsher, K., Robinson, J. T., Goodwin, A., Zaric, S. & Dai, H. Nano-graphene oxide for cellular imaging and drug delivery. *Nano Research* **1,** 203–212 (2008).

46. Li, N., Cheng, Y., Song, Q., Jiang, Z., Tang, M. & Cheng, G. Graphene meets biology. *Chinese Science Bulletin* **59,** 1341–1354 (2014).

47. Cohen-Karni, T., Qing, Q., Li, Q., Fang, Y. & Lieber, C. M. Graphene and nanowire transistors for cellular interfaces and electrical recording. *Nano Letters* **10,** 1098–1102 (2010).

48. Pampaloni, N. P., Lottner, M., Giugliano, M., Matruglio, A., D'Amico, F., Prato, M., Garrido, J. A., Ballerini, L. & Scaini, D. Single-layer graphene modulates neuronal communication and augments membrane ion currents. *Nature Nanotechnology*, 1–10 (2018).

49. Ferrari, A. C. *et al.* Science and technology roadmap for graphene, related two-dimensional crystals, and hybrid systems. *Nanoscale* **7,** 4598–4810 (2015).

50. Groenendaal, B. L., Jonas, F., Freitag, D., Pielartzik, H. & Reynolds, J. R. Poly(3,4-ethylenedioxythiophene) and its Derivatives: Past, Present, and Future. *Advanced Materials,* 481–494 (2000).

51. Shi, H., Liu, C., Jiang, Q. & Xu, J. Effective Approaches to Improve the Electrical Conductivity of PEDOT:PSS: A Review. *Advanced Electronic Materials* **1,** 1–16 (2015).

52. Mantione, D., del Agua, I., Sanchez-Sanchez, A. & Mecerreyes, D. Poly(3,4-ethylenedioxythiophene) (PEDOT) derivatives: Innovative conductive polymers for bioelectronics. *Polymers* **9** (2017).

53. Samba, R. Development and characterization of PEDOT-CNT microelectrode arrays for advanced neuronal recording, stimulation and sensing. *PhD thesis, University of Tübingen* (2013).

54. Blau, A., Murr, A., Wolff, S., Sernagor, E., Medini, P., Iurilli, G., Ziegler, C. & Benfenati, F. Flexible, all-polymer microelectrode arrays for the capture of cardiac and neuronal signals. *Biomaterials* **32,** 1778–1786 (2011).

55. Sessolo, M., Khodagholy, D., Rivnay, J., Maddalena, F., Gleyzes, M., Steidl, E., Buisson, B. & Malliaras, G. G. Easy-to-fabricate conducting polymer microelectrode arrays. *Advanced Materials* **25,** 2135–2139 (2013).

56. Ludwig, K. A., Uram, J. D., Yang, J., Martin, D. C. & Kipke, D. R. Chronic neural recordings using silicon microelectrode arrays electrochemically deposited with a poly(3,4-ethylenedioxythiophene) (PEDOT) film. *Journal of Neural Engineering* **3,** 59–70 (2006).

57. Green, R. A., Lovell, N. H., Wallace, G. G. & Poole-Warren, L. A. Conducting polymers for neural interfaces: Challenges in developing an effective long-term implant. *Biomaterials* **29,** 3393–3399 (2008).

58. Thunemann, M. *et al.* Deep 2-photon imaging and artifact-free optogenetics through transparent graphene microelectrode arrays. *Nature Communications* **9,** 1–12 (2018).

59. Gabay, T., Ben-David, M., Kalifa, I., Sorkin, R., Abrams, Z. R., Ben-Jacob, E. & Hanein, Y. Electrochemical and biological properties of carbon nanotube based multi-electrode arrays. *Nanotechnology* **18,** 35201–35201 (2007).

60. David-Pur, M., Bareket-Keren, L., Beit-Yaakov, G., Raz-Prag, D. & Hanein, Y. All-carbon-nanotube flexible multi-electrode array for neuronal recording and stimulation. *Biomedical Microdevices* **16,** 43–53 (2014).

61. McDonald, M., Monaco, A., Vahidpour, F., Haenen, K., Giugliano, M. & Nesladek, M. Diamond microelectrode arrays for in vitro neuronal recordings. *MRS Communications* **7,** 683–690 (2017).

62. Koerbitzer, B., Krauss, P., Nick, C., Yadav, S., Schneider, J. J. & Thielemann, C. Graphene electrodes for stimulation of neuronal cells. *2D Materials* **3,** 024004 (2016).

63. Lu, Y., Liu, X., Hattori, R., Ren, C., Zhang, X. & Komiyama, T. Ultralow Impedance Graphene Microelectrodes with High Optical Transparency for Simultaneous Deep Two-Photon Imaging in Transgenic Mice. *Advanced Functional Materials* **1800002,** 1–9 (2018).

64. Gaio, N., Silvestri, C., Van Meer, B., Vollebregt, S., Mummery, C. L. & Dekker, R. Fabrication and Characterization of an Upside-Down Carbon Nanotube Microelectrode Array. *IEEE Sensors Journal* **16,** 8685–8691 (2016).

65. Schneider, K., Stamm, B., Gutöhrlein, K., Burkhardt, C., Stett, A. & Kern, D. P. CVD growth of carbon nanotubes with a Ni catalyst in a polyimide trench. *Nanosystems: Physics Chemistry Mathematics* **5,** 86–90 (4 2014).

66. Keefer, E. W., Botterman, B. R., Romero, M. I., Rossi, A. F. & Gross, G. W. Carbon nanotube coating improves neuronal recordings. *Nature Nanotechnology* **3,** 434–439 (2008).

67. Kshirsagar, P., Martina, M., Jones, P. D., Buckenmaier, S., Kraushsaar, U., Chassé, T., Fleischer, M. & Burkhardt, C. J. Semitransparent carbon microelectrodes for opto- and electrophysiology. *Journal of Micromechanics and Microengineering* **28** (2018).

68. Kshirsagar, P., Schroeppel, B., Haehnel, D., Mohr, A., Wirtz, T., Eswara, S. & Burkhardt, C. Catalytic growth of carbon nanotubes on atomic layer deposited nickel layers - a FIB/SEM, EDX and ToF-SIMS study. *Microscopy Conference (Lausanne)* (2017).

69. Kshirsagar, P. Twisted Bilayer Graphene. *Masters Thesis, University of Stuttgart* (2015).

70. Lempka, S. F., Johnson, M. D., Moffitt, M. A., Otto, K. J., Kipke, D. R. & McIntyre, C. C. Theoretical analysis of intracortical microelectrode recordings. *Journal of Neural Engineering* **8** (2011).

71. Raman, C. V. A new radiation. *Proceedings of the Indian Academy of Sciences - Section A* **37,** 333–341 (1953).

72. Reina, A., Jia, X., Ho, J., Nezich, D., Son, H., Bulovic, V., Dresselhaus, M. S. & Jing, K. Large area, few-layer graphene films on arbitrary substrates by chemical vapor deposition. *Nano Letters* **9,** 30–35 (2009).

73. Malard, L. M., Pimenta, M. A., Dresselhaus, G. & Dresselhaus, M. S. Raman spectroscopy in graphene. *Physics Reports* **473,** 51–87 (2009).

74. Dresselhaus, M., Jorio, A. & Saito, R. Characterizing Graphene, Graphite, and Carbon Nanotubes by Raman Spectroscopy. *Annual Review of Condensed Matter Physics* **1,** 89–108 (2010).

75. Ferrari, A. C. Raman spectroscopy of graphene and graphite: Disorder, electron-phonon coupling, doping and nonadiabatic effects. *Solid State Communications* **143,** 47–57 (2007).

76. Wang, Y. Y., Ni, Z. H., Yu, T., Shen, Z. X., Wang, H. M., Wu, Y. H., Chen, W. & Wee, A. T. S. Raman studies of monolayer graphene: The substrate effect. *Journal of Physical Chemistry C* **112,** 10637–10640 (2008).

77. Blake, P., Hill, E. W., Castro Neto, A. H., Novoselov, K. S., Jiang, D., Yang, R., Booth, T. J. & Geim, A. K. Making graphene visible. *Applied Physics Letters* **91** (2007).

78. Mafra, D. L., Moujaes, E. A., Doorn, S. K., Htoon, H., Nunes, R. W. & Pimenta, M. A. A study of inner process double-resonance Raman scattering in bilayer graphene. *Carbon* **49,** 1511–1515 (2011).

79. Stavytska-Barba, M. & Kelley, A. M. Surface Enhanced Raman Study of the Interaction of Organic Solar Cell Components with Plasmonically Active Nanoparticles. *Journal of Physial Chemistry C* **114,** 6822–30 (2010).

80. Raj, P. G., Rani, V. S., Kanwat, A. & Jang, J. Enhanced organic photovoltaic properties via structural modifications in PEDOT : PSS due to graphene oxide doping. *Materials Research Bulletin* **74,** 346–352 (2016).

81. Chen, Y., Xu, J., Yang, Y., Li, S. & Yang, W. PEDOT : PSS / graphene / PEDOT ternary film for high performance electrochemical electrode. *Journal of Materials Science: Materials in Electronics* **26,** 8292–8300 (2015).

82. Suzuki, T., Morikawa, J., Hashimoto, T., Buividas, R., Gervinskas, G., Paipulas, D., Malinauskas, M., Mizeikis, V. & Juodkazis, S. Thermal and optical properties of sol-gel and SU-8 resists. *Advanced Fabrication Technologies for Micro/Nano Optics and Photonics V* **8249,** 82490K (2012).

83. Kraushaar, U., Meyer, T., Hess, D., Gepstein, L., Mummery, C., Braam, S. & Guenther, E. Cardiac safety pharmacology: from human ether-a-gogo related gene channel block towards induced pluripotent stem cell based disease models. *Expert Opinion on Drug Safety* **11,** 285–298 (2012).

84. Kumar, T. R., Larson, M., Wang, H., McDermott, J. & Bronshteyn, I. Transgenic Mouse Technology: Principles and Methods. *Methods Molecular Biology* **590,** 335–362 (2009).

85. Seah, C.-M., Chai, S.-P. & Mohamed, A. R. Mechanisms of graphene growth by chemical vapour deposition on transition metals. *Carbon* **70,** 1–21 (2013).

86. Allen, M. Honeycomb carbon – A study of graphene. *American Chemical Society,* 184 (2009).

87. Zhang, Y., Zhang, L. & Zhou, C. Review of chemical vapor deposition of graphene and related applications. *Accounts of Chemical Research* **46,** 2329–2339 (2013).

88. Bhaviripudi, S., Jia, X., Dresselhaus, M. S. & Kong, J. Role of kinetic factors in chemical vapor deposition synthesis of uniform large area graphene using copper catalyst. *Nano Letters* **10,** 4128–4133 (2010).

89. Li, X., Cai, W., Colombo, L. & Ruoff, R. S. Evolution of graphene growth on Ni and Cu by carbon isotope labeling. *Nano Letters* **9,** 4268–4272 (2009).

90. Zhang, W., Wu, P., Li, Z. & Yang, J. First-principles thermodynamics of graphene growth on Cu surfaces. *Journal of Physical Chemistry C* **115,** 17782–17787 (2011).

91. Lisi, N., Dikonimos, T., Buonocore, F., Pittori, M., Mazzaro, R., Rizzoli, R., Marras, S. & Capasso, A. Contamination-free graphene by chemical vapor deposition in quartz furnaces. *Scientific Reports* **7,** 1–11 (2017).

92. Wang, W. X., Liang, S. H., Yu, T., Li, D. H., Li, Y. B. & Han, X. F. The study of interaction between graphene and metals by Raman spectroscopy. *Journal of Applied Physics* **109,** 07C501 (2011).

93. Brownson, D. A. C. & Banks, C. E. *The handbook of Graphene Electrochemistry* 1–6, 208 (Springer-Verlag London Ltd., 2014).

94. Robinson, R. S., Sternitzke, K., McDermott, M. T. & McCreery, R. L. Morphology and Electrochemical Effects of Defects on Highly Oriented Pyrolytic Graphite. *Journal of the Electrochemical Society* **138,** 2412–2418 (1991).

95. Valota, A. T., Kinloch, I. A., Novoselov, K. S., Casiraghi, C., Eckmann, A., Hill, E. W. & Dryfe, R. A. Electrochemical behavior of monolayer and bilayer graphene. *ACS Nano* **5,** 8809–8815 (2011).

96. Liu, Y., Weng, B., Razal, J. M., Xu, Q., Zhao, C. & Hou, Y. High-Performance Flexible All- Solid-State Supercapacitor from Large Free-Standing Graphene- PEDOT / PSS Films. *Scientific Reports* **5,** 1–11 (2015).

97. Islam, M. M., Chidembo, A. T., Aboutalebi, S. H., Cardillo, D., Liu, H. K., Konstantinov, K. & Dou, S. X. Liquid Crystalline Graphene Oxide/PEDOT:PSS Self-Assembled 3D Architecture for Binder-Free Supercapacitor Electrodes. *Frontiers in Energy Research* **2,** 1–11 (2014).

98. Park, C., Yoo, D., Im, S., Kim, S., Cho, W., Ryu, J. & Kim, J. H. Large-scalable RTCVD Graphene/PEDOT:PSS hybrid conductive film for application in transparent and flexible thermoelectric nanogenerators. *RSC Advances* **7,** 25237–25243 (2017).

99. Yoo, D., Kim, J. & Kim, J. H. Direct synthesis of highly conductive PEDOT:PSS/graphene composites and their applications in energy harvesting systems. *Nano Research* **7,** 717–730 (2014).

100. Kim, J. C., Rahman, M. M., Ju, M. J. & Lee, J. J. Highly conductive and stable graphene/PEDOT:PSS composite as a metal free cathode for organic dye-sensitized solar cells. *RSC Advances* **8,** 19058–19066 (2018).

101. Ahmed, S., Rafat, M., Sigh, M. K. & Hashmi, S. A. A free-standing, flexible PEDOT:PSS film and its nanocomposites with graphene nanoplatelets as electrodes for quasi-solid-state supercapacitors. *Nanotechnology* **29** (2018).

102. Abidian, M. R., Corey, J. M., Kipke, D. R. & Martin, D. C. Conducting-Polymer Nanotubes Improve Electrical Properties, Mechanical Adhesion, Neural Attachment, and Neurite Outgrowth of Neural Electrodes. *Small* **6,** 421–429 (2010).

103. Pranti, A. S., Schander, A., Bödecker, A. & Lang, W. Highly Stable PEDOT:PSS Coating on Gold Microelectrodes with Improved Charge Injection Capacity for Chronic Neural Stimulation. *Proceedings of Eurosensors 2017* **1,** 492 (2017).

104. Cui, X. & Martin, D. C. Electrochemical Deposition and Characterization of Poly (3,4-Ethylenedioxythiophene) on Neural Microelectrode Arrays. *Sensors and Actuators B* **89,** 92–102 (2003).

105. Wang, K., Tian, L., Wang, T., Zhang, Z., Gao, X., Wu, L., Fu, B. & Liu, X. Electrodeposition of alginate with PEDOT / PSS coated MWCNTs to make an interpenetrating conducting hydrogel for neural interface. *Composite Interfaces* **6440,** 27–40 (2018).

106. Qiang, Y. *et al.* Bilayer Nanomesh Structures for Transparent Recording and Stimulating Microelectrodes. *Advanced Functional Materials* **27,** 1704117 (2017).

107. Schander, A., Tesmann, T., Strokov, S., Stemmann, H., Kreiter, A. K. & Lang, W. In-vitro evaluation of the long-term stability of PEDOT:PSS coated microelectrodes for chronic recording and electrical stimulation of neurons. *Proceedings of the Annual International Conference of the IEEE Engineering in Medicine and Biology Society, EMBS* **2016-October,** 6174–6177 (2016).

108. Bobacka, J., Lewenstam, A. & Ivaska, A. Electrochemical impedance spectroscopy of oxidized poly (3, 4-ethylenedioxythiophene) film electrodes in aqueous solutions. *Journal of Electroanalytical Chemistry* **489,** 17–27 (2000).

109. Xiao, Y., Lin, J. Y., Tai, S. Y., Chou, S. W., Yue, G. & Wu, J. Pulse electropolymerization of high performance PEDOT/MWCNT counter electrodes for Pt-free dye-sensitized solar cells. *Journal of Materials Chemistry* **22,** 19919–19925 (2012).

110. Tamburri, E., Orlanducci, S., Toschi, F., Terranova, M. L. & Passeri, D. Growth mechanisms, morphology, and electroactivity of PEDOT layers produced by electrochemical routes in aqueous medium. *Synthetic Metals* **159,** 406–414 (2009).

111. Han, D., Yang, G., Song, J., Niu, L. & Ivaska, A. Morphology of electrodeposited poly(3,4-ethylenedioxythiophene)/poly(4-styrene sulfonate) films. *Journal of Electroanalytical Chemistry* **602,** 24–28 (2007).

112. Castagnola, V., Bayon, C., Descamps, E. & Bergaud, C. Morphology and conductivity of PEDOT layers produced by different electrochemical routes. *Synthetic Metals* **189,** 7–16 (2014).

113. Chen, X., Zhang, L. & Chen, S. Large area CVD growth of graphene. *Synthetic Metals* **210,** 95–108 (2015).

About the author

Education

2015 - 19   PhD work at the NMI Natural and Medical Sciences Institute at the University of Tübingen under the supervision of Prof. Dr. Monika Fleischer and Prof. Dr. Thomas Chassé from the University of Tübingen

2014 - 15   Master Thesis at the Solid State Nanophysics Group at the Max Planck Institute for Solid State Research (Stuttgart, Germany)
Title: Twisted Bilayer Graphene

2012 - 15   Master of Science in Materials Science, University of Stuttgart, Germany

2011- 12   Bachelor Thesis at the Visvesvaraya National Institute of Technology, Nagpur
Title: Wear behaviour of mechanically alloyed $Al/Mg/SiO_2$ metal matrix composites

2008 - 12   Bachelor of Technology in Metallurgical and Materials Engineering, Visvesvaraya National Institute of Technology, Nagpur (India)

Publications

2019   P. Kshirsagar *et. al.*, **Transparent Graphene/PEDOT:PSS Microelectrodes for Electro- and Optophysiology**, *Advanced Materials Technologies*, 4 (1), 1800318
doi.org/10.1002/admt.201800318

2018   P. Kshirsagar *et. al.*, **Semitransparent carbon microelectrodes for opto- and electrophysiology**, *Journal of Micromechanics and Microengineering*, 28 (7), 075007
doi.org/10.1002/admt.201800318

Conference contributions

July 2018	**International Meeting on Substrate-Integrated Microelectrode Arrays** (Reutlingen, Germany) "Graphene-based transparent microelectrode arrays for optical access to the recording site" (poster)
Nov 2017	**Network of Electron Microscopy Tübingen Meeting** (Tübingen, Germany) "Correlative characterization of graphene microelectrodes with AFM, HIM, SEM and Raman spectroscopy" (talk)
Aug 2017	**Microscopy Conference** (Lausanne, Switzerland) "Catalytic growth of carbon nanotubes on atomic layer deposited nickel layers – a FIB / SEM, EDX, ToF-SIMS study" (poster)
Mar 2017	**Fourth Annual Conference on Optical Nanospectroscopy** (ǀ Lisbon, Portugal) " Raman spectroscopy for transparent graphene microelectrode arrays" (talk)
Mar 2017	**Deutsche Physikalische Gesellschaft Spring Meeting of the Condensed Matter Section** (Dresden, Germany) " Transparent graphene electrodes for biomedical applications" (talk)
Dec 2016	**International Conference for Young Researchers in Advanced Materials** (Bangalore, India) "Development of graphene microelectrode arrays" (poster)
Nov 2016	**Deutsche Physikerinnentagung** (Hamburg, Germany) "Towards the development of graphene based microelectrode arrays " (talk)
Sept 2016	**42nd Micro and Nano Engineering** (Vienna, Austria) "Carbon based semi-transparent microelectrode arrays " (poster)
June 2016	**International Meeting on Substrate-Integrated Microelectrode Arrays** (Reutlingen, Germany) "Development Of A Microelectrode Array With Semitransparent Carbon Nanotube Electrodes for In-Vitro Applications And Optogenetics " (poster)

More information about Pranoti Kshirsagar can be found on her website - https://pranotiksagar.wordpress.com/